UNIVERSITÀ DEGLI STUDI DI PADOVA

Sede amministrativa: Università degli Studi di Padova
Dipartimento di Fisica "Galileo Galilei"

SCUOLA DI DOTTORATO DI RICERCA IN: FISICA
XXI CICLO

MAGNESIUM-BASED THIN FILMS FOR HYDROGEN STORAGE

Direttore della Scuola: Ch.mo Prof. Attilio Stella
Supervisore: Ch.mo Prof. Paolo Mazzoldi
Co-Supervisore: Prof. Giovanni Mattei

Dottorando: Giacomo Siviero

Contents

Sommario

L'idrogeno è ritenuto essere il vettore energetico ideale, il cui utilizzo su larga scala, tuttavia, è limitato da due grossi problemi: la produzione e lo stoccaggio. Per quanto riguarda quest'ultimo, negli ultimi anni sono state compiute diverse ricerche sugli idruri metallici, che vengono preferiti allo stoccaggio gassoso ad alta pressione o liquido per le migliori proprietà gravimetriche e volumetriche, nonché per l'intrinseca sicurezza d'utilizzo. L'idruro di magnesio, MgH_2, è uno dei più studiati idruri reversibili, data la sua elevata densità gravimetrica (7.6 wt%) ed energetica (9 MJ/kg); sfortunatamente, l'eccessiva stabilità termodinamica e le cinetiche lente ne impediscono l'uso per applicazioni tecnologiche. Recentemente è stato dimostrato che notevoli miglioramenti possono essere ottenuti grazie all'uso di materiali nanostrutturati e catalizzatori. Attualmente la ricerca scientifica è incentrata sulla relazione intercorrente tra microstruttura, proprietà funzionali e stabilità: a questo proposito i film sottili sono un materiale ideale, grazie al facile controllo della loro microstruttura in fase di sintesi e alla possibilità di applicarvi diverse tecniche di caratterizzazione complementari.

In questa tesi abbiamo dapprima studiamo la relazione tra l'evoluzione del grado di cristallinità, durante i cicli d'idrogenazione, e le proprietà di assorbimento e desorbimento dell'idrogeno da parte di film sottili di magnesio ricoperti da uno strato di palladio; i film sono stati sintetizzati tramite r.f. sputtering su substrati di silicio e vetro. L'uso di diverse tecniche di caratterizzazione complementari fornisce informazioni sulle proprietà strutturali, morfologiche e funzionali. Tramite misure *in-situ* di diffrazione X ad angolo radente vengono seguite le trasformazioni strutturali che si verificano durante il processo di rilascio d'idrogeno, permettendo così di stimare cinetiche migliori e ridotte energie di attivazione, riconducibili alla nanostruttura, rispetto al Mg in fase bulk. La geometria di diffrazione ottimizzata per i film sottili rivela che la tipica tessitura iniziale viene persa dopo il primo ciclo di assorbimento e desorbimento, indicando il manifestarsi di una riorientazione dei cristalliti di magnesio indotta dall'idrogeno. Inoltre quando il magnesio forma l'idruro passa da uno stato metallico ad uno di semiconduttore a grande band gap, mostrando così interessanti proprietà elettriche e ottiche, che vengono studiate tramite spettrofotometria. Il processo reversibile di trasformazione da un metallo con alta riflettanza ad un semiconduttore con alta trasmittanza neutra è promettente nel campo dei ricoprimenti intelligenti e dei sensori d'idrogeno. Particolarmente critici per la stabilità delle proprietà funzionali con i ciclaggi si rivelano l'integrità del layer di palladio e i processi superficiali relativi: il

progressivo degrado della copertura di Pd sul film di Mg comporta il rallentamento delle cinetiche fino ad una totale inibizione del processo.

I successivi sviluppi di questo lavoro prevedono di considerare strategie atte ad incrementare la stabilità e le cinetiche del film (per esempio, con l'aggiunta di catalizzatori): come primo passo viene studiato il drogaggio del Mg con titanio. Il processo di sintesi di non-equilibrio (sputtering) permette di ottenere un elevato grado di mixing tra questi due elementi altrimenti non miscibili, determinando così per il film peculiari proprietà strutturali, stabili con i ciclaggi. Con l'aumento della concentrazione di Ti in Mg è possibile altresì ottenere delle più rapide cinetiche di assorbimento e desorbimento, grazie al fatto che l'idruro assume una struttura favorevole per il trasporto d'idrogeno. Le trasformazioni strutturali che avvengono durante il processo di desorbimento sono monitorate tramite misure di diffrazione X *in-situ* e quindi confrontate con misure parallele di trasmittanza ottica, che forniscono una stima della cinetica di rilascio dell'idrogeno. Il miglioramento indotto dal Ti risulta nella decomposizione dell'idruro persino a temperatura ambiente. Il sistema Mg-Ti si è dimostrato piuttosto affascinante e promettente e pertanto sarà soggetto ad ulteriori indagini.

Abstract

Hydrogen has been identified as the ideal energy carrier, whose widespread exploitation is still limited by two main problems: production and storage. Regarding storage, in last years a great research effort has been spent on metal hydrides, which are preferred over pressurized and liquid hydrogen because of their gravimetric and volumetric storage capabilities and also advantages concerning operational safety. Magnesium hydride, MgH_2, is one of the most studied reversible hydrides, due to its high gravimetric hydrogen density (7.6 wt%) and energy density (9 MJ/kg); unfortunately thermodynamic issues and slow kinetics are limiting its use in technological applications. Recently, it has been shown that great improvements can be attained by using nanostructured powders and catalysts. Currently a lot of research effort is focused on the relation between microstructure, functional properties, and reliability: concerning this point thin films constitute a model material, due to the easy control of microstructure and the possibility of using complementary characterization techniques.

We first study the relation between the evolution, upon successive H_2 cycling, of the crystalline degree and the H_2 sorption properties of Pd capped-textured Mg thin films grown on Si and glass substrate by r.f. sputtering. The use of complementary characterization techniques provides information on structural, morphological and functional properties. By *in-situ* continuous grazing angle x-ray diffraction measurements we follow the structural transformations during the hydrogen desorption process, estimating enhanced kinetics and lower activation energy than bulk magnesium, thanks to nanostructure. The optimized diffraction geometry reveals that the initial preferential growth, typical of thin films, is lost after the first absorption/desorption cycle, showing the hydrogen-induced reorientation of Mg crystallites. Moreover magnesium, upon hydride formation, transforms from a metal to a wide band gap semiconductor, hence showing interesting electrical and optical properties, which are studied by spectrophotometry; the switchability from a metal with high reflectance to a semiconductor with colourless high transmittance is promising for smart coatings and sensors. The Pd cap layer integrity and related surface effects are found to be crucial to the stability of functional properties during absorption/desorption cycling: the progressive degradation of Pd coverage of Mg film leads to a slowing down of kinetics, up to a complete process inhibition. Future developments of this study envisage further strategies to improve cycling stability and to speed up kinetics (e.g. by addition of suitable catalysts); as a starting point Ti-doping of Mg is considered: the non-equilibrium

synthesis (sputtering) allows a high degree of mixing of these two otherwise immiscible elements, leading to peculiar structural properties stable upon cycling. By increasing Ti concentration it is possible to attain an enhanced hydrogen absorption/desorption kinetics, thanks to a hydride structure which favours hydrogen transport. By *in-situ* diffraction measurements structural transformations occuring during desorption are monitored and then compared with concurrent optical transmittance measurements, which provide an indirect estimation of hydrogen release kinetics, whose enhancement results into hydride decomposition even at room temperature. Mg-Ti system demonstrated to be a very fascinating and promising one, and therefore will be the subject of further investigations.

Chapter 1

Introduction

Nowadays, more than ever, human beings have to face with two main correlated issues: environment and energy. After more than 150 years of exploitation of fossil fuels, which have been the basis of our prosperity, things are going to get worse: climate change and depletion of oil fields call for a strong effort to find environment-friendly energy sources.

1.1 Energy

The great progress and wealth achieved in industrialized countries is strictly connected to access to energy sources: the availability of energy, mainly in the form of fossil fuels, set the right basis for the rapid improvement in conditions of human life in the last century, although not homogeneously distributed. Nowadays most of energy is provided by fossil fuels, nuclear energy and, to a smaller extent, by renewable energy (figure 1.1); energy is mainly used for manufacturing (33%), households (29%), mobility (26%).

Despite strong efforts to diversify energy sources in last years, 80% of energy was still provided by fossil fuels in 2005, whose carbon dioxide (CO_2) emissions after burning are suspected to be responsible for the warming of global climate. There are many observations of increasing air and ocean temperatures, widespread melting of snow and ice, and of rising sea levels. More specifically, over the last 100 years (1906-2005), global temperature has increased by 0.74°C. Global sea level has risen by 17 cm during the 20th century, in part because of the melting of snow and ice from many mountains and in the polar regions. More regional changes have also been observed, including changes in Arctic temperatures and ice, ocean salinity, wind patterns, droughts, precipitations, frequency of heat waves and intensity of tropical cyclones. Temperatures of the last half century are unusual in comparison with those of at least the previous 1300 years. The Earth's climate is influenced by many factors, mainly by the amount of energy coming from the sun, but also by factors such as the amount of greenhouse gases and aerosols in the atmosphere, and the properties of the Earth's surface, which determine how much of this solar energy is retained or reflected back to space. Atmospheric concentrations of greenhouse gases such as carbon dioxide, methane (CH_4) and nitrous oxide (N_2O) have significantly increased since the beginning

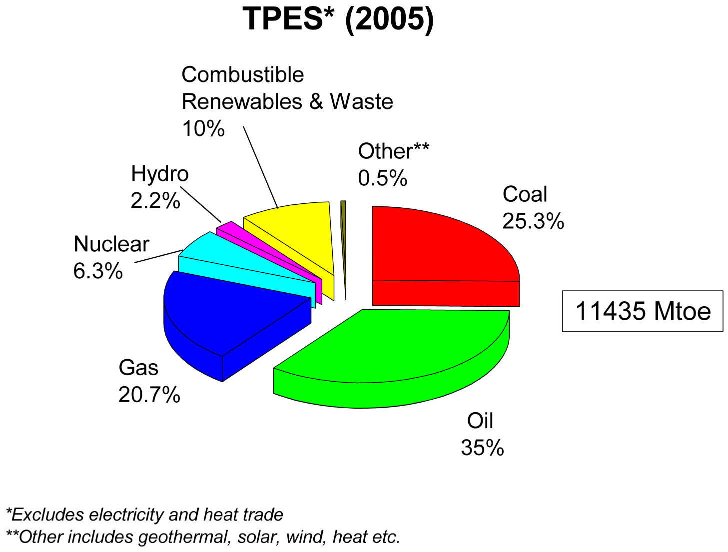

Figure 1.1: Fuel share of total primary energy supply in Million tons of oil equivalent (Mtoe) units (1 Mtoe=11630 GWh).

of the industrial revolution. This is mainly due to human activities, such as the burning of fossil fuels, land use change, and agriculture (figure 1.2). For instance, the atmospheric concentration of carbon dioxide is now far higher than in the last 650000 years and has been growing faster in the last 10 years than it has been since the beginning of continuous measurements around 1960. From IPCC reports [1] it comes out that most of the global warming effect on the Earth is due to human activities since 1750, although it must be pointed out that there's still a strong debate on the main cause of climate change, especially on the reliability of climate models used to predict future warming. Nevertheless, most of industrialized countries decided to slow down emissions, signing the "Kyoto Protocol" in 1997 and pushing the development of renewable energy.

Nowadays the average power consumption per capita is 2 kW, with peak values in North America and negligible consumption of fossil fuels for 2 billion people: this value is going to increase, due to the fast economic growth of developing countries like China and India, whose energy demand has been estimated to increase upto 95% by 2030. In fact The Asia-Pacific region accounted for two thirds of global energy consumption growth (2.4%) in 2007 [2]; worldwide energy demand is projected to grow by 50% over the 2005 to 2030 period with the lion's share still represented by fossil fuels (figure 1.3) both with current energy policy and alternative one[1]. People have a strong awareness of the importance of energy: it's at the first position of the top-ten list of prioritized problems we'll have to

---

[1] Reference scenario takes account of those government policies and measures that were enacted or adopted by mid-2006; on the contrary Alternative scenario analyses how the global energy market could evolve if countries were to adopt all of the policies they are currently considering related to energy security and energy-related CO_2 emissions [3].

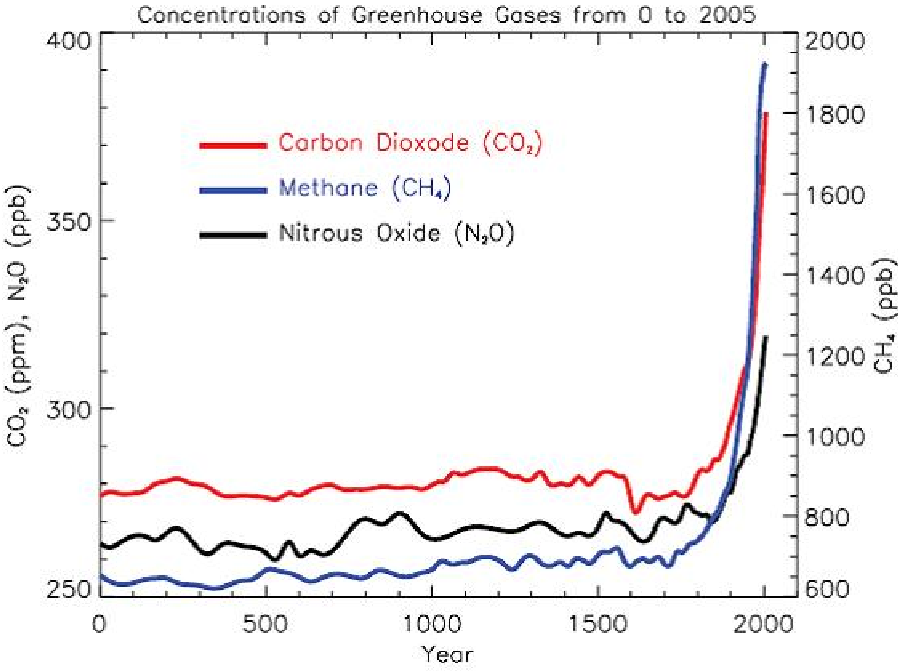

Figure 1.2: Atmospheric concentrations of important long-lived greenhouse gases over the last 2,000 years. Concentration units are parts per million (ppm) or parts per billion (ppb), indicating the number of molecules of the greenhouse gas per million or billion air molecules, respectively, in an atmospheric sample. From [1].

deal with in this century, above water and food [4]. There's the feeling that our society is energy dependent at all, especially on fossil fuels.

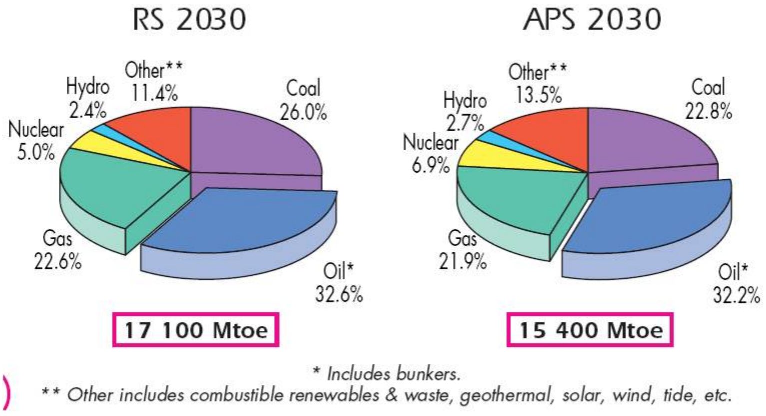

Figure 1.3: Projected fuel share of total primary energy supply in 2030 in reference (RS) and alternative policy scenario (APS) [5].

It is interesting to focus on oil, which is not only a great primary energy source, but also the best form of transporting energy over long distances. Considering the importance of transport sector in our society, the fact that it relies almost completely on cheap petroleum products clearly gives an idea of our dependency on it; moreover oil is used in agriculture, foods, electricity generation and other important sectors. One can rightly define our economy as the ”oil-economy”.

The peak of oil discoveries was passed in the 1960s, and the rate of consumption became greater than new fields' found oil in 1981. The gap between discovery and production has widened since; moreover the oil production is supposed to follow a bell-shaped curve, whose ”peak” either has already occured or is expected in a few years [6]. Proved oil reserves amount to $1.2 \cdot 10^{12}$ barrels while daily consumption (in 2007) is $8.5 \cdot 10^7$ barrels, so if no more oil fields are found, at this consumption rate reserves will deplete in 30-40 years; moreover fossil energy carriers, especially oil and natural gas, are only present in sufficient quantities in a few regions of the world. Unconventional oil, like heavy oil in the Orinoco oil belt or Canadian oil sands, optimistically amounts to $4 \cdot 10^{12}$ barrels and could substitute for crude oil as soon as the price rises high enough to make them profitable; however heavy crudes have a more severe environmental impact than light ones so governments could put a limit on the growing of this kind of production [6]. It is also claimed that an oil-based economy such as ours doesn't need to deplete its entire reserve of oil before beginning to collapse. A shortfall between demand and supply as little as 10 to 15 percent could be enough to wholly shatter an oil-dependent economy and reduce people to poverty [7].

It is apparent that transition from an oil-economy to a ”different energy source”–economy will be a hard issue. The best solution would be an affordable, reliable and renewable energy source: unfortunately current technology can't satisfy these requirements yet; nevertheless a medium-term proposed solution will be: improving efficiency in energy conversion and use, increasing reliance on non-fossil fuels and sustaining the domestic supply of oil and gas within net energy-importing countries (Alternative Policy Scenario, [3]). The long term solution is foreseen to be characterized mainly by solar, wind, geothermal resources with contributions from nuclear fission/fusion processes and biomass exploitation [4].

1.2 Electricity

An important aspect related to energy use is constituted by electricity, which is an energy carrier in the sense that, once created from a primary energy source, it can transport the energy of that source in a usable form. Its extraordinary versatility means it can be put to an almost limitless set of applications which include transportation, heating, lighting, communications, and computation. The backbone of modern industrial society is, and for the foreseeable future can be expected to remain, the use of electrical power [8]. Electricity production was responsible for 32% of total global fossil fuel use in 2005, accounting for $132 \cdot 10^{18}$J. It was also the source of 41%, or 10.9 Gtons, of energy-related CO_2 emissions. As can be seen in figure 1.4, 67% of electricity generation derived from fossil fuels; instead no carbon dioxide is emitted by: hydropower, nuclear fission, biomass, wind, solar.

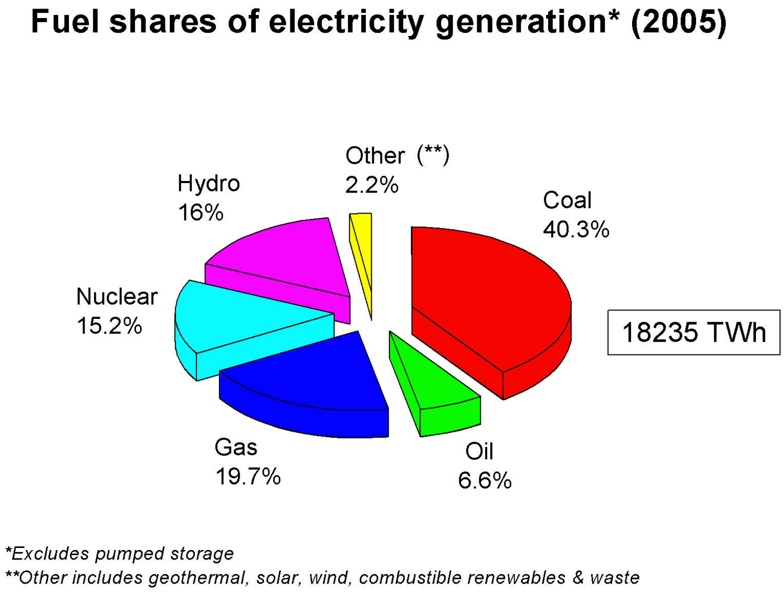

Figure 1.4: Electricity generation by fuel in 2005 [5].

Hydroelectric power plants have a generating capacity of 800 gigawatts, and they currently supply almost one-fifth of the electricity consumed worldwide. As a source of electricity, dams are second only to fossil fuels, and generate 10 times more power than geothermal, solar and wind power combined. One reason for hydropower's success is that it is a widespread resource, in fact 160 countries use hydropower to some extent; electricity costs $0.03 - 0.1$ dollars per kilowatt-hour, which makes dams competitive with coal and gas. Moreover, the fact that hydroelectric systems require no fuel means that they also require no fuel-extracting infrastructure and no fuel transport. This means that a gigawatt of hydropower saves the world not just a gigawatt's worth of coal burned at a fossil-fuel plant, but also the carbon dioxide costs of mining and transporting. As turning on a tap is easy, dams can respond to changing electricity demand independent of the time of day or the weather. This ease of turn-on makes them a useful back-up to less reliable renewable sources. That said, variations in use according to need and season mean that dams produce about half of their rated power capacity.

Hydroelectric systems are unique among generating systems in that they can, if correctly engineered, store the energy generated elsewhere, pumping water uphill when energy is abundant. Drawbacks are, clearly, dependence on territorial morfology and ecological effects on the ecosystems upstream and downstream; biomass that decomposes in reservoirs releases methane and carbon dioxide, and in some cases these emissions can be of a similar order of magnitude to those avoided by not burning fossil fuels. Hydroelectricity is considered a cheap and mature technology to which a TW of capacity can be added.

Concerning nuclear, the 439 current reactors have an overall capacity of 370 gigawatts, while 35 more are under construction; the light-water reactors that make up most of the world's nuclear capacity produce electricity at costs of between 0.025 and 0.07 dollars/kWh. The reserves of nuclear fuel, uranium, which could profitably be extracted at a cost of 130 \$/kg or less are 5.5 Mtons; at the current consumption, these reserves will last for 80 years. However considering the so-called "undiscovered reserves" and lower-grade ores, an availability of 35 million tons of fuel is estimated; in addition to uranium, thorium-fuelled reactors are under study. Furthermore breeder reactors, which make plutonium from uranium isotopes (U-238) that are not themselves useful for power production, can effectively create more fuel than they use, getting up to 60 times more energy out for every kg of natural uranium put in; they are however expensive to build and could only be justified economically if uranium prices were to rise to pre-1980 values, well above the current market price. Nuclear power can run at full blast almost constantly: this makes them well suited to providing always-on baseload[2] power to national grids. Uranium is sufficiently widespread that the world's nuclear-fuel supply is unlikely to be threatened by political factors, in fact Canada and Australia currently account for 44% of global production. The 4^{th} generation of nuclear reactors (GEN-IV) is expected to enter the market after 2030. It includes three fast reactor concepts cooled by liquid lead, sodium or gas (LFR, SFR, GFR), and three thermal reactor concepts cooled by high temperature helium (VHTR), molten-salt (MSR), and supercritical water (SCWR). All concepts are designed to improve passive safety, to minimise long-life radioactive waste production and to reduce costs [9]. In the future, nuclear capacity is expected to grow by, at least, a factor of two. Main, well known drawbacks of nuclear fission power are: waste management,

---

[2] The amount of power required to meet minimum demands based on reasonable expectations of customer requirements

risk of nuclear weapons proliferation, terrorists'threat and , especially, public acceptance. Furthermore, from a different point of view, it is also extremely capital intensive and requires highly trained professionals, whose number could not be sufficient for future needs. Finally, politics is, without doubt, called for dealing responsibly with this issue.

Biomass was the largest energy source until the twentieth century: wood, crop residues and other biological sources are still an important energy source for more than two billion people. Over recent years biomass has become a source of fossil-fuel-free electricity, with a generating capacity of at least 40 GW. The price of biomass electricity varies widely depending on the availability and type of the fuel and the cost of transporting it. Capital costs are similar to those for fossil fuel plants. Power costs can be as little as 0.02 dollars/kWh when biomass is burned with coal in a conventional power plant, but increase from $0.03 - 0.05$/kWh for a dedicated biomass power plant to $0.04 - 0.09$/kWh for a co-generation plant, where recovery and use of the waste heat makes the process much more efficient [10]. The biggest problem for new biomass power plants is finding a reliable and concentrated feedstock that is available locally. Biomass is limited by the available land surface, the efficiency of photosynthesis, and the supply of water: OECD and IPCC estimate a maximum electricity generation capacity of 2 to 5 TW by 2050; however, by storing solar energy in the form of chemical bonds, biomass lends itself better than other renewable energy resources to the production of fuel for transportation, so biofuels might easily beat electricity generation as end-use for biomass. Plants are by nature carbon neutral and renewable and, if burned in power plants fitted with carbon capture-and-storage hardware, they become carbon negative, effectively sucking carbon dioxide out of the atmosphere and storing it in the ground. On the other hand in next years land use for biomass production could conflict with the need to provide food for the growing world's population, so adequate policies by governments should provide a sustainable land use.

Heat from Earth's interior is due both to the planet's original coalescence and to decay of radioactive elements; it can be used for electricity generation, although in a few specific places, or by small geothermal heat pumps that warm buildings directly. The best sites to exploit can generate electricity at about 0.05 $/kWh and with today's technology, 70 GW of the global heat flux is seen as exploitable. Geothermal resources are ideally suited to supplying base-load electricity, because they are driven by a very regular energy supply. At 75%, geothermal sources boast a higher capacity factor than any other renewable. Some drawbacks are constituted by the dishomogeneous distribution of resources, risk of CO_2 leak out and water contamination; it is expected that geothermal capacity will increase by an order of magnitude [10].

Most famous renewable energy source is sun with its nuclear fusion processes sending 100000 TW to the earth's surface: wind and solar energy technologies are different ways to harness it.

Utilization of wind energy has increased spectacularly in recent years, with a 27% increase in installed capacity during 2007 capping similar rises in previous years. This brought total world wind capacity to 94 GW, with tens of thousands of turbines now operating. Wind turbines of up to 5 MW are now functioning in many countries, though most new ones are 1-2 MW. The power output is a function of the cube of the wind speed, so doubling the wind speed gives eight times the energy potential. In operation such turbines require a wind in the range 4 to 25 m/s, with maximum output being at 12-25 m/s (the excess energy being spilled above 25 m/s). Where there is an economic back-up which can be called upon at very short notice (e.g. hydro), a significant proportion of electricity can be provided from wind. The most economical and practical size of commercial wind turbines is now up to 2 MW, grouped into wind farms up to 200 MW. Depending on site, most turbines operate at about 25% load factor over the course of a year (European average), but some reach 33%. Wind is projected to supply 3% of world electricity in 2030 (about 30000 TWh)[3]. With increased scale and numbers of units, generation costs have been diminishing (0.05 to 0.09 dollars/kWh). They are still greater than those for coal or nuclear, however government policies in many countries ensure that power from them is able to be sold.

There are two ways of converting the sun's radiant energy to electricity: photovoltaics (PV) and concentrating solar power (CSP). A standard commercial solar photovoltaic panel can convert 12 to 18% of the energy of sunlight into useable electricity and world's total solar cell capacity is around 9 GW. However, the actual amount of electricity generated, though, is considerably less, as night and clouds decrease the power available. Of all renewables, solar currently has the lowest capacity factor, at about 14% [10]. More efficiency can be gained using concentrator PV, where some kind of parabolic mirror tracks the sun and increases the intensity of the solar radiation up to 1000-times. Moreover wavelenght down–conversion systems are currently under study to increase solar cells efficiency by using Rare Earths complexes as converters [11].
Concentrated solar thermal systems use mirrors to focus the Sun's heat, typically heating up a working fluid that in turn drives a turbine. The mirrors can be set in troughs, in parabolas that track the Sun, or in arrays that focus the heat on a central tower [12]. Current costs are 0.17 (CSP) to 0.25-0.40 dollars/kWh (PV), but a drop is expected in next years. Theoretically, with current technology all world's energy needs could be served by covering with PV less than a tenth of Sahara desert; covering all buildings roofs surface could also give a substantial contribute. Darkness and cloud coverage variability represent the main problems with PV; however, provided that suitable storage options are developed, solar power is foreseen as the most promising carbon-free technology[3].

Although most of expectations rely on wind and solar, they are affected by a big drawback, intermittency, which implies lack of control to provide base-load or peak-load power; their unreliability can be overcome only when coupled with efficient storage.

A possible solution for mobility requirements and energy storage could be hydrogen, which is thought to be the best candidate as an energy carrier.

---

[3] Clearly, in this vision the manufacture and installation of PV cells should not imply any carbon emissions.

1.3 Thesis outline

In the next chapters we will introduce Hydrogen Economy, by treating important issues, such as hydrogen production and storage, especially focussing on metal hydrides and some important breakthroughs achieved in last years; particular emphasis will be given on thin films as suitable materials to study hydrogen storage (Chapter 2). Then we will present the most used experimental technique and models to characterize our thin films (Chapter 3). Results and discussion on Pd capped–Mg thin films will be reported in Chapter 4, while in Chapter 5 we will show how the doping with Ti can substantially improve kinetics. Beside hydrogen storage research, we will also take into account how Mg–based thin films can have technological applications as hydrogen sensor, smart windows and variable reflection coatings.

Chapter 2

Hydrogen

2.1 The Hydrogen economy

Hydrogen is the most abundant element on earth: however only 1% is present as molecular gas and it mostly occurs in the form of water and hydrocarbons; so it must be produced someway spending energy. Chemical energy is based on the energy of unpaired outer electrons (valence electrons) which are to be stabilized by electrons from other atoms. The hydrogen atom is most attractive because its electron is accompanied by only one proton, i.e. hydrogen has the highest ratio number of valence electrons to protons (and neutrons) of all the elements in the periodic table. The energy gain per electron is very high; the chemical energy per mass of hydrogen (39.4 $kWh \cdot kg^{-1}$) is three times larger than that of other chemical fuels, e.g. liquid hydrocarbons (13.1 $kWh \cdot kg^{-1}$). In other words, the energy content (heating value) of 0.33 kg of hydrogen corresponds to the energy content of 1 kg of oil (table 2.1). The difference between the upper (liquid water) and the lower (water vapour) heating value is the enthalpy of vaporization of water according to the state of the water as a result of combustion. For hydrogen the lower heating value is 33.3 $kWh\ kg^{-1}$, and the upper heating value is 39.4 $kWh\ kg^{-1}$. When hydrogen burns reacting with oxygen, its combustion yields only water, from which hydrogen can be extracted again, setting on a clean, hydrogen–water–hydrogen cycle (figure 2.1). Moreover it is transportable over long distances, it can be much more easily stored than electrons in batteries and it's interconvertible with electricity. Two types of challenges must be overcome before the hydrogen economy becomes reality: one is economic, the other technical. The economic challenge is

Properties	H_2	Methane (CH_4)	Petrol (-CH_2-)
Lower heating value($KWh \cdot Kg^{-1}$)	33.3	13.9	12.4
Self-ignition temperature (°C)	585	540	228-501
Ignition limits in air(Vol %)	4-75	5.3-15	1-7.6
Flame propagation in air(m s^{-1})	2.65	0.4	0.4

Table 2.1: Physical and chemical properties of Hydrogen, Methane and Petrol

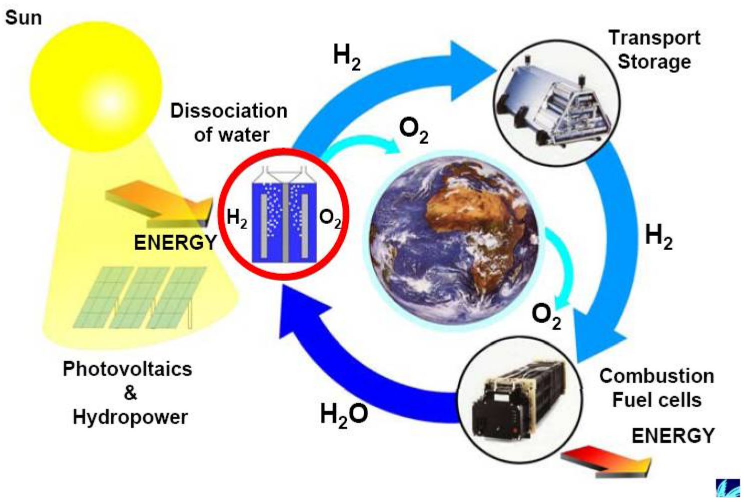

Figure 2.1: Hydrogen cycle.

the cost of hydrogen production; the world economy today is based on free energy naturally stored over millions of years. The price we are used to paying for fossil fuels is the mining cost only. In order to adapt the world to a synthetic fuel such as hydrogen, the world economy needs to be convinced of the benefits in order to see the need to pay for the energy content of the fuel too. The second challenge is the real-time production, ideally from renewable sources, the safe and convenient storage and the efficient combustion of hydrogen [13].

2.1.1 Fuel cells

Hydrogen is thought as a fuel in combination with fuel cells to produce electricity. A fuel cell is a device that uses hydrogen (or hydrogen–rich fuel) and oxygen to create electricity by an electrochemical process; a single fuel cell consists of an electrolyte and two catalyst–coated electrodes (a porous anode and cathode). While there are different fuel cell types (figure 2.2), all work on the same principle:

- Hydrogen, or a hydrogen-rich fuel, is fed to the anode where a catalyst separates hydrogen's electrons from protons;
- at the cathode, oxygen combines with electrons and, in some cases, with species such as protons or water, resulting in water or hydroxide ions, respectively;
- for polymer electrolyte membrane and phosphoric acid fuel cells, protons move through the electrolyte to the cathode to combine with oxygen and electrons, producing water and heat;
- for alkaline, molten carbonate, and solid oxide fuel cells, negative ions travel through the electrolyte to the anode where they combine with hydrogen to generate water and electrons;

- the electrons from the anode side of the cell cannot pass through the electrolyte to the positively charged cathode; they must travel around it via an electrical circuit to reach the other side of the cell, generating an electric current.

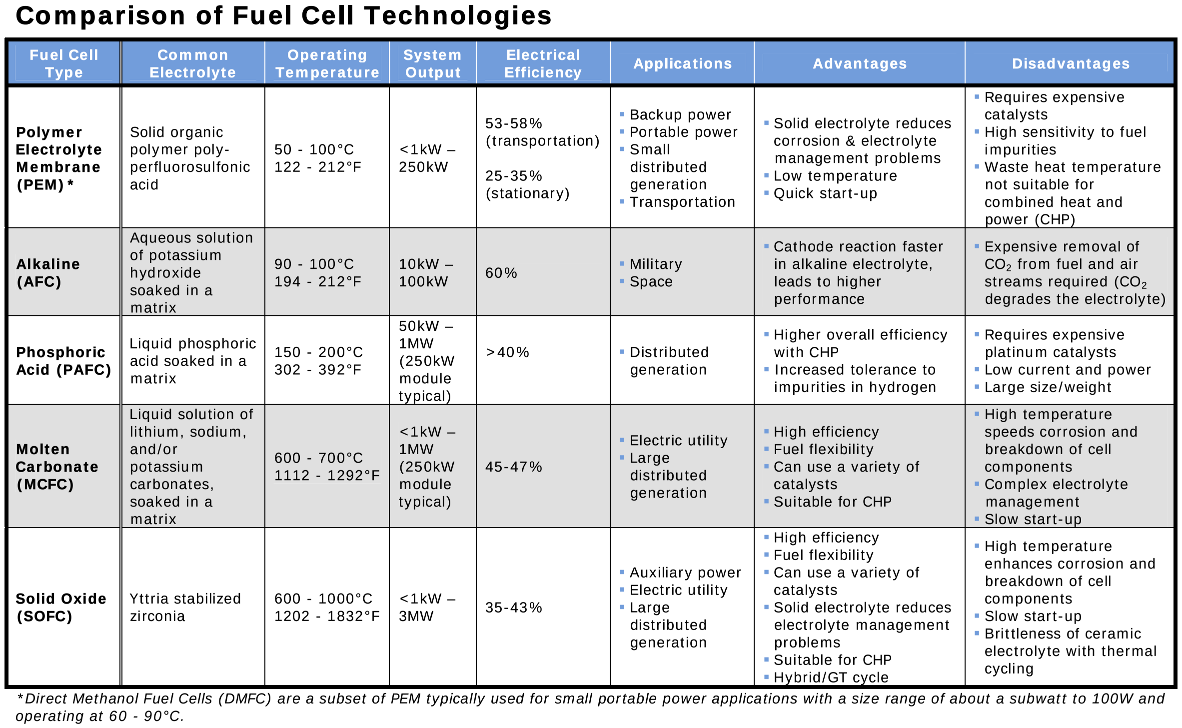

Comparison of Fuel Cell Technologies

Fuel Cell Type	Common Electrolyte	Operating Temperature	System Output	Electrical Efficiency	Applications	Advantages	Disadvantages
Polymer Electrolyte Membrane (PEM)*	Solid organic polymer poly-perfluorosulfonic acid	50 - 100°C 122 - 212°F	<1kW – 250kW	53-58% (transportation) 25-35% (stationary)	▪ Backup power ▪ Portable power ▪ Small distributed generation ▪ Transportation	▪ Solid electrolyte reduces corrosion & electrolyte management problems ▪ Low temperature ▪ Quick start-up	▪ Requires expensive catalysts ▪ High sensitivity to fuel impurities ▪ Waste heat temperature not suitable for combined heat and power (CHP)
Alkaline (AFC)	Aqueous solution of potassium hydroxide soaked in a matrix	90 - 100°C 194 - 212°F	10kW – 100kW	60%	▪ Military ▪ Space	▪ Cathode reaction faster in alkaline electrolyte, leads to higher performance	▪ Expensive removal of CO_2 from fuel and air streams required (CO_2 degrades the electrolyte)
Phosphoric Acid (PAFC)	Liquid phosphoric acid soaked in a matrix	150 - 200°C 302 - 392°F	50kW – 1MW (250kW module typical)	>40%	▪ Distributed generation	▪ Higher overall efficiency with CHP ▪ Increased tolerance to impurities in hydrogen	▪ Requires expensive platinum catalysts ▪ Low current and power ▪ Large size/weight
Molten Carbonate (MCFC)	Liquid solution of lithium, sodium, and/or potassium carbonates, soaked in a matrix	600 - 700°C 1112 - 1292°F	<1kW – 1MW (250kW module typical)	45-47%	▪ Electric utility ▪ Large distributed generation	▪ High efficiency ▪ Fuel flexibility ▪ Can use a variety of catalysts ▪ Suitable for CHP	▪ High temperature speeds corrosion and breakdown of cell components ▪ Complex electrolyte management ▪ Slow start-up
Solid Oxide (SOFC)	Yttria stabilized zirconia	600 - 1000°C 1202 - 1832°F	<1kW – 3MW	35-43%	▪ Auxiliary power ▪ Electric utility ▪ Large distributed generation	▪ High efficiency ▪ Fuel flexibility ▪ Can use a variety of catalysts ▪ Solid electrolyte reduces electrolyte management problems ▪ Suitable for CHP ▪ Hybrid/GT cycle	▪ High temperature enhances corrosion and breakdown of cell components ▪ Slow start-up ▪ Brittleness of ceramic electrolyte with thermal cycling

**Direct Methanol Fuel Cells (DMFC) are a subset of PEM typically used for small portable power applications with a size range of about a subwatt to 100W and operating at 60 - 90°C.*

Figure 2.2: Comparison between different types of fuel cells.

Polymer electrolyte membrane (PEM) fuel cells (Fig 2.3), also called proton exchange membrane fuel cells, deliver high power density and offer the advantages of low weight and volume, compared to other fuel cells. They need only hydrogen, oxygen from the air, and water to operate and do not require corrosive fluids like some fuel cells. They are typically fueled with pure hydrogen supplied from storage tanks or onboard reformers. Polymer electrolyte membrane fuel cells operate at relatively low temperatures, around 80°C. Low temperature operation allows them to start quickly (less warm-up time) and results in less wear on system components, resulting in better durability. PEM fuel cells are used primarily for transportation applications and some stationary applications. Due to their fast startup time, low sensitivity to orientation, and favorable power-to-weight ratio, PEM fuel cells are particularly suitable for use in passenger vehicles, such as cars and buses. The half reactions occuring at the electrodes are:

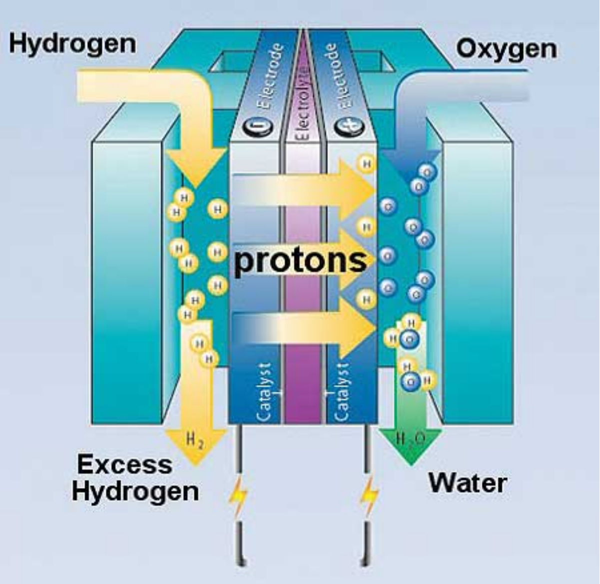

Figure 2.3: PEM fuel cell scheme.

$$\text{oxidation at the anode:} \quad 2H_2 \rightarrow 4H^+ + 4e^- \tag{2.1}$$

$$\text{reduction at the cathode:} \quad O_2 + 4H^+ + 4e^- \rightarrow 2H_2O \tag{2.2}$$

$$\text{total reaction:} \quad 2H_2 + O_2 \rightarrow 2H_2O \tag{2.3}$$

The PEM's heart is the electrolyte membrane: it's a polymer, usually Nafion, which, in the presence of water, allows positive ions (protons) to move freely, carrying charge across the membrane; on the other hand it is an insulator for electrons, which then travel through the external wire to reach the cathode and so completing the circuit. Typical thicknesses are around 50 to 175μm. Reactions occurring at the electrodes are usually slow at 80°C, so they require a noble-metal catalyst (typically platinum) to separate the hydrogen's electrons and protons. The best way to increase reaction kinetics is to use porous carbon with Pt nanoparticles (2 nm) dispersed in it: in this way both electrons can move and gases are allowed to diffuse through the electrode to reach Pt. In addition to the cost, Pt catalyst is also extremely sensitive to CO poisoning, making it necessary to employ an additional reactor to reduce CO in the fuel gas if the hydrogen is derived from an alcohol or hydrocarbon fuel. Developers are currently exploring platinum/ruthenium catalysts that are more resistant to CO.

A key issue is the water management: although water is a product of the reaction and is carried out of the cell by the air flow, it is important that also fuel and air entering the cell are humidified, because the membrane must be hydrated. The humidity of reactants is crucial: too little water decreases proton conductivity, while too much water makes the cathode flood. Thus not enough oxygen can penetrate the liquid water and reach the cathode catalyst sites.

In order to maximize the current from the membrane/electrode assembly, backing layers, flow fields, and current collectors are employed. The backing layers are made of a porous carbon paper or carbon cloth and, while enclosing the membrane/electrodes assembly, allow the right amount of water vapor to reach it and keep the membrane humidified. The backing layers are often coated with Teflon to ensure that at least some, and preferably most, of the pores in the carbon cloth (or carbon paper) do not become clogged with water, which would prevent the rapid gas diffusion necessary for a good rate of reaction at the electrodes. Pressed against the outer surface of each backing layer is a piece of hardware called a bipolar plate that typically serves as both flow field and current collector. In a single fuel cell, these two plates are the last of the components making up the cell. The plates are made of a lightweight, strong, gas–impermeable, electron–conducting material (graphite or metals ,although composite plates are now being developed). Their first task is to provide a gas flow field thanks to channels etched into the side of the plate next to the backing layer; the pattern of the flow field determines how evenly the reactant gases are spread across the active area of the membrane/electrode assembly. The second task is to collect current: electrons produced by the oxidation of hydrogen must (1) be conducted through the anode, through the backing layer, along the length of the stack, and through the plate before they can exit the cell; (2) travel through an external circuit, and (3) re-enter the cell at the cathode plate.

In a fuel cell the chemical energy of fuel is converted in electric energy and heat: a single ideal H_2/air fuel cell should provide a voltage of $V = 1.16V$ at zero current, 80°C and 1 atm gas pressure [14]. The cell voltage depends on current density, as represented by the *characteristic performance curve.* Additional important parameters for a fuel cell are the ratio of the power produced $P = VI$ to the mass of the cell (*specific power*) and the ratio of the power produced to the volume of the cell (*power density*). An estimation of efficiency is given by the ratio of the actual cell voltage to the theoretical maximum one: thus considering that a cell can operate at 0.7 V, about 60% of the total available energy from the fuel is converted as electric power, 40% as heat; if the waste heat is also used, efficiencies of 90% are possible: a great improvement in respect of internal combustion engines, which can reach an efficiency of 41%. The open circuit potential $V = \Delta E$ of the cell is given by

$$\Delta G_f = -nF\Delta E \tag{2.4}$$

where G is the Gibbs free energy, n stands for the number of electrons transferred and F for the Faraday constant ($F = 96484.56Cmol^{-1}$)[15]. Therefore, the theoretical maximum efficiency of the fuel cell at constant temperature is given by

$$\eta = \frac{\Delta G_f}{\Delta H_f} = 1 - T\frac{\Delta S_f}{\Delta H_f} \tag{2.5}$$

In practice fuel cells are connected in series to obtain the required voltage (e.g.: electric motors operate at 200–300 V) so forming a ”stack”.

2.1.2 Hydrogen production

The establishment of the Hydrogen economy will be possible only if clean, efficient and affordable methods of production are developed; in fact nowadays most of the hydrogen consumed ($5 \times 10^{10} kg/year$ [13]) is produced by using fossil fuels, for which carbon dioxide emission is a concern. The world vehicle fleet in 2000 was 700 million and may possibly reach 1500 million by 2050: replacement of fossil fuels by hydrogen would require hydrogen–production of about 260 million tons/year by 2050 [16].

Nowadays there are three classes of processes to produce hydrogen: thermal, electrolytic and photolytic processes.

Among thermal processes, natural gas reforming could be a pathway for near–term hydrogen production during the transition to a hydrogen economy: in this process, gasoline, propane or methane contained in the gas reacts with steam at high temperatures (700–1000°C) under 3 to 25 bar pressure in the presence of a catalyst (Ni, Co, Fe or Pt), producing hydrogen and carbon monoxide, which successively is transformed into CO_2 by reacting with steam in the ”water–gas shift reaction”, producing more hydrogen (2.7) [17]. The final step, called ”pressure–swing adsorption”, consists in the removal of carbon dioxide and other impurities from gas steam, leaving pure hydrogen as required by fuel cells.

$$\text{Steam reforming for } CH_4\text{:} \quad CH_4 + H_2O \rightarrow CO + 3H_2 \quad \Delta\, H = 226\ kJmol^{-1} \tag{2.6}$$

$$\text{Water-gas shift:} \quad CO + H_2O \rightarrow CO_2 + H_2 \quad \Delta\, H = -41\ kJmol^{-1} \tag{2.7}$$

Steam reforming is an endothermic process, so energy is required to make the reaction proceed. Producing hydrogen from natural gas does result in some greenhouse gas emissions. When compared to internal combustion engine vehicles using gasoline, however, fuel cell vehicles using hydrogen produced from natural gas reduce greenhouse gas emissions by 60% [12]; moreover carbon capture and storage methods are under development. Natural gas reforming is thought as a mature technology to produce hydrogen for the transition period only: it must be overtaken by other cleaner and import–independent methods.

Another thermal process is coal gasification: coal is converted into a gaseous mixture of hydrogen, carbon monoxide, carbon dioxide, and other compounds by applying heat under pressure in the presence of steam and a controlled amount of oxygen (in a unit called a gasifier). The coal is chemically broken apart by the gasifier’s heat, steam, and oxygen, setting into motion chemical reactions that produce a synthesis gas (syngas), a mixture of primarily hydrogen, carbon monoxide, and carbon dioxide. The carbon monoxide is reacted (in a separate unit) with water to form carbon dioxide and more hydrogen. Adsorbers or special membranes can separate the hydrogen from this gas stream. The environmental benefits of gasification stem from the capability to achieve extremely low SO_x, NO_x and particulate emissions from burning coal–derived gases. Sulfur in coal, for example, is converted to hydrogen sulfide and can be captured by processes presently used in the chemical industry. In some methods, the sulfur can be extracted in either a liquid or solid form that can be sold commercially. In an Integrated Gasification Combined-Cycle (IGCC) plant, the syngas produced is virtually free of fuel–bound nitrogen. Diluting the syngas allows for NO_x emissions as low as 15 parts per million. Selective Catalytic Reduction (SCR) can be used to reach levels comparable to firing with natural gas if required to meet more stringent emission levels. Other advanced emission control processes are being developed that could reduce NO_x from hydrogen fired turbines to as low as 2 parts per million. Coal gasification may offer a further environmental advantage: if oxygen is used in a coal gasifier instead of air, carbon dioxide is emitted as a concentrated gas stream in syngas at high pressure. In this form, it can be captured and sequestered more easily and at lower costs. By contrast, when coal burns or is reacted in air, 79% of which is nitrogen, the resulting carbon dioxide is diluted and more costly to separate [18].

Water splitting is the process of hydrogen production on which most of efforts are spent in order to arrive at a low–cost commercial production. By applying external energy, pure hydrogen and oxygen can be obtained, without carbon or sulfur impurities; on the other hand it is expensive in comparison with reforming of natural gas.

High–temperature water splitting is a technology under early stages of development: high temperature heat (500–2000°C), provided by either solar concentrators (up to 2000°C) or nuclear reactors (up to 1000°C)[16], drives a series of chemical reactions which consume only water and produce hydrogen and oxygen by using chemicals reused for several cycles. The Zn/ZnO cycle is an example of such a process: Zinc oxide powder is passed through a reactor heated by a solar concentrator operating at about 1900°C. At this temperature, the zinc oxide dissociates to zinc and oxygen gases. The zinc is cooled, separated, and reacted with water to form hydrogen gas and solid zinc oxide. The net result is hydrogen and oxygen, produced from water. The hydrogen can be separated and purified. The Zinc oxide can be recycled and reused to create more hydrogen through this process.

Electrolytic processes achieve water splitting by using electricity, which can result in zero greenhouse gases emissions, depending on the source of the electricity used. Like fuel cells, electrolyzers consist of an anode and a cathode separated by an electrolyte: alkaline electrolyzers (2.8), whose electrolyte is an alkaline solution of NaOH or KOH, have been commercially available for many years.

$$\begin{array}{ll}\text{reaction at the anode:} & 2H_2O + 2e^- \rightarrow 2OH^- + H_2 \\ \text{reaction at the cathode:} & 2OH^- \rightarrow H_2O + \frac{1}{2}O_2 + 2e^- \\ \text{total reaction:} & H_2O \rightarrow H_2 + \frac{1}{2}O_2 \end{array} \tag{2.8}$$

They operate at temperatures between 60°C to 150°C and require a voltage of $1.48V$ (higher heating value, liquid water) or $1.25V$ (lower heating value, water vapour), which

decreases with temperature increase. Efficiencies can reach 80%. In high temperature electrolysis additional heat supports the electrical water splitting, due to its higher efficiency at high temperatures (100–800 °C).
A promising way to produce hydrogen is photoelectrochemical water splitting, in which light incident on a semiconductor electrode creates electron–hole pairs. The holes carry out the oxidation of water to oxygen and H^+ ions, while the electrons reduce the H^+ ions to H_2 in gaseous form. In its simplest form, a photoelectrochemical (PEC) hydrogen production cell consists of a semiconductor electrode and a metal counter electrode immersed in an aqueous electrolyte [19].

2.1.3 Storage

Beside production, hydrogen storage is the other main issue for transition to hydrogen economy. According to hydrogen phase diagram (2.4), at ambient temperature and pressure 1 kg of hydrogen is a molecular gas which takes a volume of 11 m^3: storage basically implies the reduction of this large volume, by increasing pressure or by reducing temperature below the critical one or by interaction with another material. Hydrogen can be stored in six basic ways, which are reported in the following paragraphs. Important parameters to characterize a storage method are *gravimetric* and *volumetric* densities, which give the ratio of the hydrogen weight to total weight and to total volume, respectively and, of course, the reversibility of hydrogen uptake and release. U.S. Department of Energy (DoE) has set several requirements which a storage method should satisfy in order to be suitable for mobility [20]: unfortunately, none of the currently available methods satisfies all of them.

The most common and established storage system are high–pressure gas cylinders with a maximum pressure of 20 MPa; new composite cylinders can withstand pressure up to 80 MPa, so that hydrogen can reach a volumetric density of 36 $Kg\ m^{-3}$ [13]. Hydrogen can be compressed isothermically by normal compressors, if a theoretical work given by (2.9) is provided,

$$\Delta G = RT \cdot ln\frac{p}{p_0} \tag{2.9}$$

where R is the gas constant, T the absolute temperature, p_0 and p the starting and end pressure, respectively. It results that the process consumes 2.21 $kWh\ kg^{-1}$, although in reality more work is needed due to the non isothermal condition of compression. There's, however, a trade-off between gravimetric and volumetric density for cylinders: the higher the pressure, the thicker the cylinder's walls must be; safety of pressurized systems is also an issue of concern. Target set by industry is a 70 MPa cylinder with a mass of 110 Kg resulting in a gravimetric density of 6% and volumetric density of 30 $Kg\ m^{-3}$.

A small zone in the phase diagram, starting at the triple point and ending at the critical point, exhibits the liquid hydrogen with a density of 70.8 $kg \cdot m^{-3}$ at -253 °C. Liquid hydrogen is stored in cryogenic tanks at 21.2 K at ambient pressure. Due to the low critical temperature (33 K), liquid hydrogen can only be stored in open systems, because there is no liquid phase existing above the critical temperature. The pressure in a closed storage

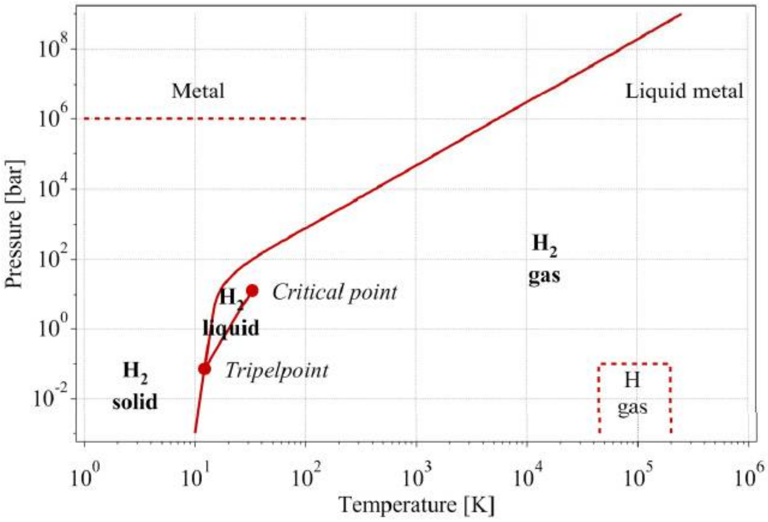

Figure 2.4: Hydrogen phase diagram.

system at room temperature could increase to about 10^4 bar. The challenges of liquid hydrogen storage are the energy–efficient liquefaction process and the thermal insulation of the cryogenic storage vessel in order to reduce the boil–off of hydrogen. Liquid hydrogen can't be obtained simply through the *Joule-Thompson* cycle: in fact upon expansion at room temperature it warms up so it must be cooled below its *inversion temperature* (202 K) in order to be liquefied. Therefore, hydrogen is usually pre-cooled using liquid nitrogen (78 K) before the first expansion step occurs. The free enthalpy change between gaseous hydrogen at 300 K and liquid hydrogen at 20 K is 11640 $kJ \cdot kg^{-1}$ [21]. The necessary theoretical work to liquefy hydrogen from room temperature is $W = 3.23\ kWh \cdot kg^{-1}$, the technical work is about 5 times larger, almost half of the lower heating value of hydrogen combustion. The boil–off rate of hydrogen from a liquid hydrogen storage vessel due to heat leaks is a function of the size, shape and thermal insulation of the vessel. Theoretically the best shape is a sphere, since it has the least surface to volume ratio and because stress and strain are distributed uniformly. However, large-sized spherical containers are expensive because of their manufacturing difficulty. Since boil-off losses due to heat leaks are proportional to the surface to volume ratio, the evaporation rate diminishes drastically as the storage tank size increases. For double–walled vacuum–insulated spherical Dewar vessels, boil-off losses are typically 0.4% per day for tanks which have a storage volume of 50 m^3, 0.2% for 100 m^3 tanks, and 0.06% for 20000 m^3 tanks.

Hydrogen can also be stored by physisorption, which is the adsorption of a gas (adsorbate) on a surface as consequence of the field force at the surface of the solid (adsorbent). The origin of the physisorption are resonant fluctuations of the charge distributions, called Van der Waals interactions; the gas molecule interacts through an attractive–repulsive potential with several atoms at the solid surface, reaching a minimum in potential energy (0.01–0.1 eV) at a distance of about one molecular radius. Due to the weak interac-

tion, a significant physisorption is observed at temperatures below 273 K. Much work on reversible hydrogen adsorption has been related to carbon nanotubes, for which some researchers (over)estimated a storage capacity of 5–10% in 1997. The main interest in carbon nanotubes is the curvature of the graphene sheets and the cavity inside the tube. In microporous solids with capillaries which have a width not exceeding a few molecular diameters, the potential fields from opposite walls will overlap so that the attractive force which acts on adsorbate molecules will be increased compared with that on a flat carbon surface. A realistic hydrogen storage capacity for single–wall carbon nanotubes with a specific surface area of 1315 $m^2 g^{-1}$ is up to 2% in mass at $T = 77\ K$ [22].
Beside the carbon nanostructures, other nanoporous materials have been investigated for hydrogen absorption. The hydrogen absorption of zeolites of different pore architecture and composition was studied: as an example 1.8 mass% of adsorbed hydrogen was found for a zeolite (NaY) with a specific surface area of 725 $m^2 \cdot g^{-1}$ [23]. The big advantages of the physisorption for hydrogen storage are the low operating pressure, the relatively low cost of the materials involved, and the simple design of the storage system. The rather small amount of adsorbed hydrogen on carbon, together with the low temperatures necessary, are significant drawbacks of hydrogen storage based on physisorption.

Many metals and alloys are capable of reversibly absorbing large amounts of hydrogen: charging can be done either using molecular hydrogen gas or hydrogen atoms from an electrolyte. These metal–hydrogen compounds are called hydrides. Metal hydrides are often preferred over storage methods described above because of their gravimetric and volumetric storage capacities and safe operating pressures; besides, they are suitable for hydrogen compression, heat storage, refrigerators, gas separation [24]. It must be pointed out that hydrogen absorption affects electronic an magnetic properties of the hosting metals, which can thus show significant modified properties, such as optical and electrical ones (see following sections).
Hydrogen reacts at elevated temperature with many transition metals (TM) and their alloys to form hydrides. The electropositive elements are the most reactive, i.e. scandium, yttrium, the lanthanides, the actinides, and the members of the titanium and vanadium groups. The binary hydrides of the TM are predominantly metallic in character and are usually referred to as metallic hydrides. They are good conductors of electricity, possess a metallic or graphite–like appearance, and can often be wetted by mercury. Many of these compounds (MH_n) show large deviations from ideal stoichiometry (n=1, 2, 3) and can exist as multi–phase systems. The lattice structure is that of a typical metal with atoms of hydrogen on the interstitial sites; for this reason they are also called interstitial hydrides. This type of structure has the limiting compositions MH, MH_2 and MH_3; the hydrogen atoms fit into octahedral or tetrahedral holes in the metal lattice, or a combination of the two types. The hydrogen carries a partial negative charge, depending on the metal; an exception is, for example, $PdH_{0.7}$ [25]. Only a few TM do not form or have unstable form of hydrides: Pt, Ru, and Ni ($NiH_{<1}$), Cr (CrH, CrH_2) and Cu (CuH), respectively. Among light metals, a very interesting one is magnesium with its theoretical storage ca-

Alloy type	Prototype	Hydrides	Max. capacity [wt.%]	$\Delta H[kJ\ mol^{-1}H_2]$
A	Mg	MgH_2	7.66	-76
A_2B	Mg_2Ni	Mg_2NiH_4	3.59	-64.5
AB	$TiFe$	$TiFeH_2$	1.89	-28.1
AB_5	$LaNi_5$	$LaNi_5H_6$	1.49	-30.8
Comp.	$Na+Al$	$NaAlH_4(Ti)$	5.6	$-47/-37$

Table 2.2: Some Hydride-forming metals and intermetallic compounds with their storage capacity and formation enthalpy. A is an element with a high affinity to hydrogen, and B is an element with a low affinity to hydrogen. (Adapted from [13])

pacity of 7.66%; investigations of metal hydrides have been carried out for several years with hydrogen interacting with metals in the form of micrometer-size powder, which is thought to be suitable for technological appliance.

The reaction of hydrogen gas with a metal, which is driven by difference in Gibbs free energy between gaseous hydrogen and hydrogen in metal, is called the absorption process and consists of several surface and bulk steps. It can be described in terms of a simplified one–dimensional potential energy curve (one dimensional Lennard-Jones potential, see figure 2.5). Far from the metal surface the potentials of a hydrogen molecule and of 2 hydrogen atoms are separated by the dissociation energy ($E_D = 218\ kJ\ mol^{-1}$H). The first attractive interaction of the hydrogen molecule approaching the metal surface is the Van der Waals force leading to the physisorbed state ($E_{Phys} = 10\ kJ\ mol^{-1}\ H$), at approximately one hydrogen molecule radius (0.2 nm) from the metal surface. Closer to the surface the hydrogen has to overcome an activation barrier for dissociation and formation of the

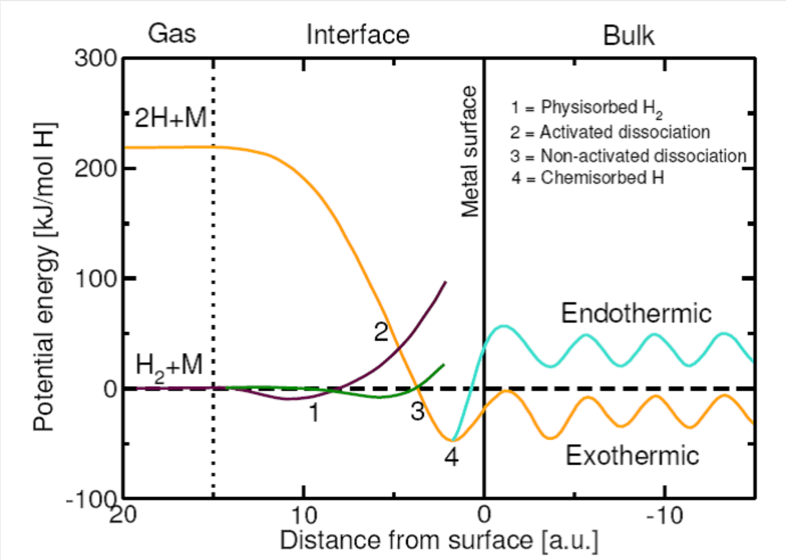

Figure 2.5: Schematic Lennard–Jones potential of a hydrogen atom at the metal surface.

hydrogen-metal bond. The height of the activation barrier depends on the surface elements involved: activation barriers up to 400 meV were found on s–electron metals, while lower values are common for d–electron ones. Hydrogen atoms sharing their electron with the metal atoms at the surface are then in the chemisorbed state ($E_{Chem} = 50kJ\ mol^{-1}\ H$). The chemisorbed hydrogen atoms may have a high surface mobility, interact with each other and form surface phases at sufficiently high coverage. In the next step the chemisorbed hydrogen atom can jump in the subsurface layer and finally diffuse on the interstitial sites through the host metal lattice [26]. The hydrogen atoms contribute with their electron to the band structure of the metal. The hydrogen is present at a small hydrogen to metal ratio ($H/M < 0.1$) exothermically dissolved (solid solution, α–phase) in the metal. The metal lattice expands proportionally to the hydrogen concentration by approximately 2–3 Åper hydrogen atom [27]. At greater hydrogen concentrations in the host metal ($H/M > 0.1$) a strong H–H interaction, due to the lattice expansion, becomes important and the hydride phase (β–phase) nucleates and grows. The hydrogen concentration in the hydride phase is often found to be $H/M = 1$. The volume expansion between the coexisting α– and the β–phase corresponds in many cases to $10 \div 20\%$ of the metal lattice. Therefore, at the phase boundary a large amount of stress is built up and often leads to a decrepitation of brittle host metals such as intermetallic compounds. The final hydride is a powder with a typical particle size of 10 to 100 μm. The thermodynamic aspects of the hydride formation from gaseous hydrogen is described by means of pressure–composition isotherms (see figure 2.6).

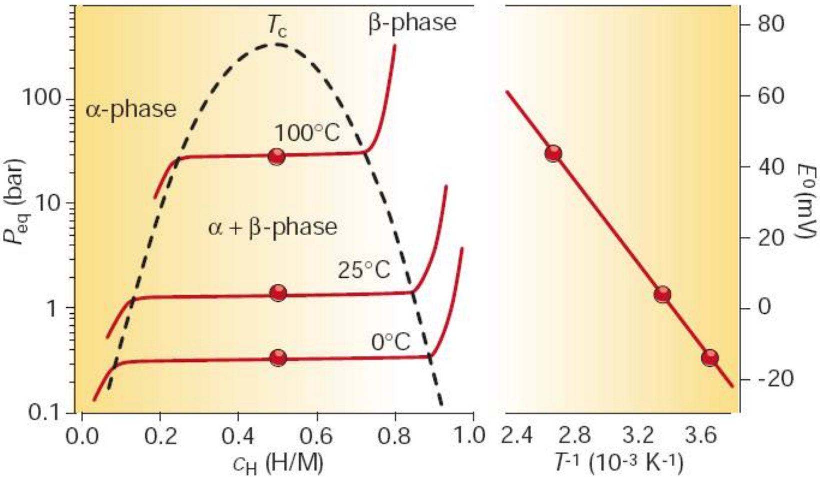

Figure 2.6: Left: pressure–composition isotherms for the hydrogen absorption in a typical intermetallic compound; right: Van't Hoff plot to extract ΔH and ΔS.

While the solid solution and hydride phase coexists, the isotherms show a flat plateau, whose length determines the amount of H_2 that can be stored; in the pure β–phase, the H_2 pressure rises steeply with the concentration. The two–phase region ends in a critical point T_C, above which the transition from α to β–phase is continuous. The equilibrium pressure P_{eq} as a function of temperature is related to the changes ΔH and ΔS of enthalpy and entropy, respectively, by the Van't Hoff equation (2.10), where R is the gas constant and P^0_{eq} the standard equilibrium pressure.

$$ln\left(\frac{P_{eq}}{P^0_{eq}}\right) = \frac{\Delta H}{RT} - \frac{\Delta S}{R} \tag{2.10}$$

As ΔS corresponds mostly to the change from molecular hydrogen gas to dissolved hydrogen in metals, it amounts approximately to the standard entropy of hydrogen ($S_0 = 130\ J \cdot K^{-1}\ mol^{-1}$) and is therefore, $\Delta S_f \approx 130\ J \cdot K^{-1} mol^{-1}\ H_2$ for all metal–hydrogen systems. The enthalpy term characterizes the stability of the metal hydrogen bond: if hydride formation is exothermal, heat has to be provided to the metal hydride to desorb the hydrogen. If the hydrogen desorbs below room temperature, this heat can be delivered by the environment. However, if the desorption is carried out above room temperature, the necessary heat has to be delivered at the necessary temperature from an external source which may be the combustion of hydrogen in a fuel cell (e.g. PEMFC, T≈80°C): for MgH_2 the heat necessary for desorption at 300°C and 1 bar is approximately 25% of the higher heating value of hydrogen. Reffering to DoE requirements for vehicular usage (Table 2.3), to reach an equilibrium pressure of 1 bar at 300 K, ΔH should amount to $-39.2\ kJ\ mol^{-1} H_2$. Beside thermodynamic requirements, an important issue is the rate at which the reaction of absorption/desorption proceeds; a thermodynamically favoured reaction ($\Delta G < 0$)can be seriously slowed down by activation barriers: in fact many metals show very slow absorption/desorption kinetics, which prevents their use for technological applications. In order to improve thermodynamic and kinetic properties, researchers have tried several ways:

Property	Target
System gravimetric capacity	2 kWh kg^{-1} (0.06 kg H_2/kg system)
System volumetric capacity	1.5 kWh L^{-1} (0.045 kg H_2/L system)
Fuel cost	133 \$ $kg^{-1} H_2$
Operating ambient temperature	−30 to 50°C
Cycle life	1000
System fill time (5 kg of H)	3 min.
Equilibrium pressure (MH)	1 bar at room temp.

Table 2.3: Technical DoE targets for on-board hydrogen storage systems by 2010 (Adapted from [28] and [20])

- destabilization of metal–hydrogen bond to tailor ΔH by alloying elements with different hydrogen affinities. Especially interesting are the metallic hydrides of intermetallic compounds (see table 2.2): in the simplest case the ternary system AB_xH_n, because the variation of the elements allows tailoring of the properties of the hydrides. The A element is usually a rare earth or an alkaline earth metal and tends to form a stable hydride. The B element is often a transition metal and forms only unstable hydrides. Some well defined ratios of B to A in the intermetallic compound x=(0.5, 1, 2, 5) have been found to form hydrides with a hydrogen to metal ratio of up to 2;

- reduction to nanostructure;
- insertion of catalysts to speed up one or more hydrogenation steps– e.g. Pd, Pt and Ru are known to be excellent hydrogenation catalysts;

Metal hydrides are very effective for storing large amounts of hydrogen in a safe and compact way. All the reversible hydrides working around ambient temperature and atmospheric pressure consist of transition metals; therefore the gravimetric hydrogen density is limited to <3 mass%. It is still a challenge to explore the properties of the lightweight metal hydrides [13].

Particular interest is put on the group one, two and three light elements (e.g. Li, Mg, B, Al) which build a large variety of metal–hydrogen complexes (*complex hydride*). They are attractive because of their light weight and the number of hydrogen atoms per metal atom, which is in many cases 2. The main difference of the complex hydrides to the metallic hydrides is the transition to an ionic or covalent compound of the metals upon hydrogen absorption. The hydrogen in the complex hydrides of light elements previously cited is often located in the corners of a tetrahedron with boron or aluminium in the centre. The negative charge of the anion, $[BH_4]^-$ and $[AlH_4]^-$, is compensated by a cation, e.g. Li or Na. The hydride complexes of borane, the tetrahydroborates $M(BH_4)$, and of alane, the tetrahydroaluminate $M(AlH_4)$, are interesting storage materials; however, they are known to be stable and decompose only at elevated temperatures and often above the melting point of the complex.

Absorption and desorption pressure–concentration isotherms of catalysed $NaAlH_4$ at temperatures of 180°C and 210°C were presented for the first time in 1996 [29]. The catalysed system reversibly absorbed and desorbed hydrogen up to 4.2 mass% and the mechanism of a two–step reaction was described. A desorption hydrogen pressure of 2 bar at 60°C was found and the enthalpy for the dissociation reaction was determined to be 37 $kJ\ mol^{-1}$ and 47 $kJ\ mol^{-1}$ for the first an second dissociation step of Ti–doped $NaAlH_4$, respectively (2.11).

$$\begin{aligned} 3NaAlH_4 &\rightarrow NaAlH_6 + 2Al + 3H_2\ (3.7wt\%) \\ Na_3AlH_6 &\rightarrow 3NaH + Al + \tfrac{3}{2}H_2\ (3.0wt\%) \end{aligned} \tag{2.11}$$

The compound with the highest gravimetric hydrogen density at room temperature known today is $LiBH_4$ (18 mass%). Therefore, this complex hydride could be the ideal hydrogen storage material for mobile applications. $LiBH_4$ desorbs three of the four hydrogen atoms

in the compound upon melting at 280°C and decomposes into LiH and boron. The desorption process can be catalysed by adding SiO_2 and significant thermal desorption was observed starting at 100°C [30]. Recently it has been shown that the hydrogen desorption reaction is reversible and the end–products lithimhydride and boron absorb hydrogen at 690°C and 200 bar to form $LiBH_4$ [31].
Complex hydrides represent new hydrogen storage materials, whose stability, kinetics and reversibility are almost unknown and difficult to study, since most of them don't exist as intermetallic compounds when hydrogen is removed.

The last hydrogen storage method regards reaction with water. Direct hydrogen generation from metals is possible e.g. by making two sodium atoms react with two water molecules resulting into sodium hydroxide and one hydrogen molecule. The reaction is not directly reversible but the sodium hydroxide could later be removed and reduced in a solar furnace back to metallic sodium. The hydrogen molecule produces again a water molecule in the combustion, which can be recycled to generate more hydrogen gas. However, the second water molecule necessary for the oxidation of the two sodium atoms has to be added. Therefore, sodium has a gravimetric hydrogen density of 3 mass%. The same process carried out with lithium leads to a gravimetric hydrogen density of 6.3 mass%. The major challenge with this storage method is the reversibility and the control of the thermal reduction process in order to produce the metal in a solar furnace [13].
Similarly, hydrolitic generation of hydrogen is obtained by reaction of metal hydrides with water [28]. For example lithium boron hydride has 8.6% storage capacity ($LiBH_4 + 4H_2O \rightarrow LiOH + H_3BO_3 + 4H_2$) while magnesium hydride 6.3% ($MgH_2 + 2H_2O \rightarrow Mg(OH)_2 + 2H_2$). Clearly, regeneration of spent storage materials can't be done onboard but has to be performed in dedicated plants. Although the material costs seem to relegate hydrolitic processes to "niche" applications, some systems are considered for commercial use. $NaBH_4$ is reasonably stable in alkaline aqueous media, but can be catalytically decomposed by Ruthenium or other catalysts; storage would be in the form of 25% solution of $NaBH_4$ in 2% of NaOH aqueous solution: by introducing the catalyst hydrolisis reaction gives H_2 and aqueous $NaBO_2$ solution, which will be then regenerated externally. The total capacity is 5.3% in mass. The advantage of this system is the easy-to-handle liquid state of the fuel, but on the other hand part of products has to be stored onboard.

2.2 Magnesium hydride

There has been a considerable research for a lot of years on magnesium and its alloys for on–board hydrogen storage, due to their high hydrogen–storage capacity and low cost. Mg has also good–quality functional properties such as heat resistance, vibration absorbing, reversibility and reciclability [32].
Magnesium hydride MgH_2 has a high energy density (9 MJ Kg^{-1}) and a high storage capacity (7.6 wt % , 132 g l^{-1}): moreover it is the eighth most frequent element on the earth and thus it is relatively inexpensive. Magnesium has a hcp structure which transforms

to a tetragonal (rutile type) one when hydrogen is absorbed and magnesium hydride is formed, inducing a 30% increase in volume of the cell (α phase)(figure 2.7); at least 3 other phases, which form at higher pressure, are known: β , γ , δ [33]. Beside structural modifications, hydrogen intercalation involves also changes in electronic properties: in fact magnesium is a metal, while its hydride is a wide band–gap semiconductor. Major drawbacks of magnesium, which prevent its use for storage applications, are slow absorption and desorption kinetics even at high temperatures: in practice temperatures of 350–400°C are required to have reaction over a time scale of hours. Being the equilibrium pressure of hydrogen gas in equilibrium with MgH_2 1 bar at 280°C, thermodynamics would allow readily hydride formation at room temperature: this however never occurs because of kinetic limitations.

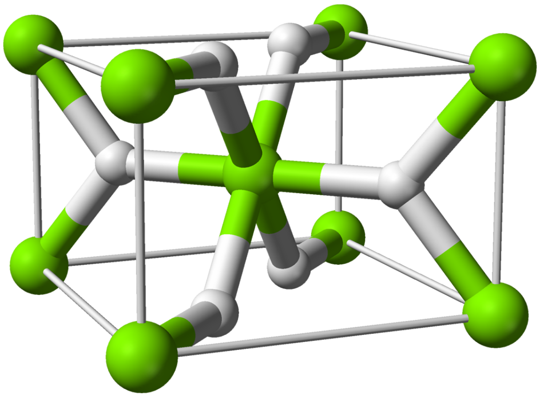

Figure 2.7: Magnesium hydride alpha phase Small atoms: H, big: Mg.

Several factors reduce the rate of hydrogenation [34]:

- Magnesium surface oxidation and/or formation of magnesium hydroxide. When Mg is exposed to air a MgO layer, which is not transparent to hydrogen molecules , forms readily, so impeding hydrogen penetration into the metal; MgO has to be cracked to start absorption, so high temperature (400°C) annealing cycles (*activation*) are usually required to allow hydrogenation. Magnesium hydroxide also requires such high temperatures to decompose. However, even if activation is performed, hydrogenation still requires several hours at a pressure of 30 bar and a temperature of 400°C;

- Surface dissociation. It is well known that clean magnesium surface is not active for dissociation of molecular hydrogen, which is the first step to start the absorption process [35];

- Nucleation and growth process. The rate of absorption can be increased by increasing pressure, which basically tunes the thermodynamic driving force for the process. However this trend stops at a certain point, when the initial fast hydrogenation has formed a near–surface hydride shell, whose growth is now the limiting step for the

> hydrogenation process: growth is controlled by hydrogen diffusion, which is very slow in MgH_2 [36], although further experiments suggest that growth might be controlled by hydrogen diffusion along Mg–MgH_2 interface. In any case Mg complete hydrogenation can't be achieved, because it was found that a 50 μm MgH_2 layer is enough to kinetically block hydrogen diffusion.

On the other hand, in addition to kinetic issues, hydrogen desorption process is limited by the high enthalphy of formation ($-76\ kJ\ mol^{-1} H_2$) of the hydride, which requires a lot of energy to break Mg–H bonds ($\approx 30\%$ of the H energy content). Moreover thermal management upon hydride formation is an additional important issue, that is frequently forgotten.

Different measures have been explored to accelerate sorption and desorption kinetics and destabilize Mg–H bond, with the constraint of affecting as little as possible hydrogen storage capacity.

2.2.1 Role of microstructure

As previously said, diffusion of hydrogen has a great importance for the rate of hydride formation: in general small crystallite size and the lower packing density of the atoms offered by grain boundaries allow faster diffusion than in the lattice; furthermore grain boundaries are nucleation sites for MgH_2 formation and decomposition. Then particle dimension for powder materials determines the active surface area for reaction with hydrogen and also the lenght of the diffusion path. Ball milling is an effective way to reduce structure to the nanometer scale [34]: material powders, milled in a controlled atmosphere for several hours, can achieve hydrogen absorption already at 300°C for crystallite size of less than 1 μm and a remarkable enhancement in kinetics with decreasing size. This improved hydrogenation induced by reduction to nano–structure is a consequence of several combined effects: the microstructure of ball–milled samples can contain defects such as grain boundaries, dislocations, and impurity atoms in a high number density (see figure 2.8) [37]. Near–surface grain boundaries and vacancy favour easy hydrogen penetration into the material and hydride nucleation, without the limit of the closest surface; grain boundary density is related to multi–crystal structure, which may be the most important factor for the improved properties of these nanostructured systems. Remarkably, Zaluski et al. found no changes in the initial nanostructure upon cycling at temperatures up to 450°C [34].

The influence of grain boundaries on hydrogen solubility and hydrogenation kinetics in nanostructured Pd was studied by Muetschele and Kirchheim and summarized by the latter [39]. They found that the maximum hydrogen solubility in the α phase increases while that in β phase decreases, then narrowing the α–β miscibility gap. This behaviour was explained by dividing the sample in two regions with different local solubility: grain boundaries and an interior region. Whereas the interior region dissolves hydrogen similarly to bulk Pd–H, the grain–boundary region offers sites of different energies; at low hydrogen concentrations (c_H) additional low–energy sites provided by grain boundaries are filled,

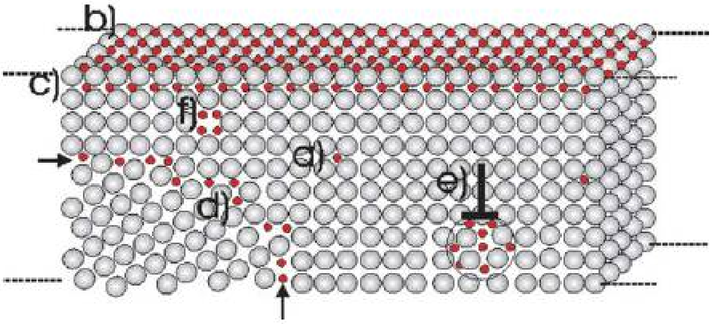

Figure 2.8: Schematic presentation of defects in a nanoscaled film and accumulation of hydrogen atoms in the low–concentration range.(a) Hydrogen solubility in the lattice matrix; trap sites for hydrogen atoms on the surface (b) and in subsurface (c) sites; (d) grain boundaries; (e) edge dislocations; (f) vacancies [38].

leading to a c_H greater than in bulk Pd–H. On the other hand, at high concentrations only those regions that behave bulk–like can transform into the hydride phase: because the hydride total volume is less than that of a single–crystal bulk sample, the mean concentration of the hydride phase in nanostructured Pd–H is lower than in bulk Pd–H. Moreover, the segregation of hydrogen at grain boundaries generates large stress for the nano–grain interiors, which could lower T_C values.

Regarding diffusion, it was found that grain boundaries have an opposite behaviour depending on c_H: at low H concentration, low–energy sites act as traps, so lowering diffusion coefficient in respect of bulk Pd; instead, when low energy sites are saturated at concentrations near the solubility limit, hydrogen interstitial–diffusion is increased by one order of magnitude.

Similar considerations are valid for dislocations, which are always present in materials because they are introduced during processing or as the result of thermal stresses that appear during the solidification of the melt. Hydrogen loading creates dislocations that accommodate the lattice mismatch between matrix and precipitate; it was found that solubility is enhanced by edge dislocations which act as traps for H in Pd: this interaction is modelled as an elastic one between the stress field around dislocations and the strain caused by the solute H atom, which results into an extra term in hydrogen chemical potential expression. Moreover H–H interaction gives rise to a rather large segregation of hydrogen at dislocations [39].

Vacancies are entropically stabilized equilibrium defects and are always present in materials. Most metals exhibit negligible equilibrium concentration of vacancies at room temperature. For example, in Nb, the concentration of thermal–equilibrium vacancies is approximately 10^{-34}. The equilibrium concentration increases at higher temperatures, and close to the melting point it becomes approximately 10^{-4}. Vacancies can be regarded as open volume defects, like an internal surface. Thus, when the surface chemisorption state of hydrogen is more energetically favored than the interstitial solution, hydrogen is driven to enter the vacancy, where it is trapped. The presence of hydrogen in the metal lattice can dramatically modify the equilibrium vacancy concentration, which can lead to superabundant vacancies (SAV) formation. This behaviour was found for many metals, in which SAV showed remarkable stability also when the metal is returned to ambient pressure and temperature. The high vacancy concentrations are correlated with a large number of hydrogen atoms trapped near one or more vacancies; for example six hydrogen atoms per vacancy complex in Fe, known as the $VacH_6$ complex, were found by Iwamoto& Fukai [40]. The vacancy–hydrogen (Vac–H) binding seems to cause the formation of SAVs, as calculated by Nordlander et al. by means of effective medium approximation [41].

2.2.2 Use of catalysts

Several attempts have been made to enhance surface kinetics using different additives. Most studied are platinum group metals like Ni [42], hydride–forming elements such as Ce, Nb and Ti [43], low–temperature metal hydrides such as $LaNi_5$ and FeTi [44], non–hydride–forming elements such as Fe, Co and Cr [45], and transition–metal compounds, for example, metal oxides [46]. In particular, 3d transition metals and metal oxides have been proven to enhance sorption kinetics significantly. Effective catalysis does not require covering the whole metal surface by an overlayer of a catalyst. Instead, very small (of the size of tens of nanometers) particles of the catalyst are sufficient, when uniformly distributed on the metal surface. This process can be explained by a spill–over phenomenon, which involves surface diffusion of reactive hydrogen formed on a dissociatively absorbing metal which then migrates over a phase where dissociative adsorption does not easily occur [47]. The key point of this process is that it does not require the surface of magnesium to be very active and free of oxides/hydroxides. It is the catalyst that dissociates or recombines the hydrogen molecules. Being able to retain the oxide layer on magnesium surface is of great practical importance: amongst other things it prevents pyrophoricity. For example Zaluski et al.[34], by using Pd, could greatly enhance sorption and desorption kinetics of nanostructured MgH_2 powders. The advantageous properties for dissociation shown by transition metals are related to the unfilled d–band; in order to separate hydrogen atoms, a change of the orbital structure with sharing of electrons between H and metal is needed: for simple and noble metals, H_2 antibonding orbital mixes with metal levels of the same simmetry forming H–M bondind and antibonding levels, which move downwards as H_2 approaches metal surface. Dissociative chemisorption occurs if H–M bonding wins the competition [26]. For transition metal d–orbitals are strongly localized and thus overlap with the H_2 orbitals; when hydrogen molecule approaches the surface, metal s–electrons can be transferred to the d–bands avoiding the penetration of the H_2 bonding orbital and thus weakening the Pauli repulsion, which could lead up to disappearance of the activation barrier [48].

Liang et al. [49] investigated the catalytic effects of the five 3d elements–Ti, V, Mn, Fe and Ni–on the reaction kinetics of ball–milled MgH_2. They found that desorption at low temperatures was most rapid for MgH_2-V, followed by MgH_2-Ti, MgH_2-Fe, MgH_2-Ni and MgH_2-Mn. On the other hand the materials containing Ti exhibited the most rapid absorption kinetics, followed in order by $Mg-V$, $Mg-Fe$, $Mg--Mn$ and $Mg-Ni$. In contrast, measurements performed by Oelerich et al.[50] using high–purity V showed only a negligible enhancement of sorption kinetics of MgH_2; however a significant enhancement (3 times) was achieved by adding 5 mol % of V_2O_5. This pushed the research on metal and transition metal oxides, which exhibit the best catalytic behaviour: basing on sistematic measurements [51, 52] Barkhordarian et al. [53] have identified several factors influencing the effectiveness of transition–metal oxide catalysts for Mg–based hydrides: (i) defect density of the oxide catalyst; (ii) thermodynamic stability of the transition–metal oxide with respect to MgO; (iii) affinity of the transition–metal to hydrogen, i.e. stability of the respective hydride; and (iv) valence state of the transition–metal ions in catalyst, i.e. the number of electrons available for bonding. In conclusion, by use of proper catalyst, it is possible to obtain reaction kinetics suitable for applications even for MgH_2.

2.2.3 Tailoring of thermodynamic properties

As already said, the high enthalpy of formation for magnesium hydride requires high desorption temperatures and efficient heat management systems. In order to decrease the thermodynamic constraints, various strategies for the development of new Mg-based alloys and intermetallics for hydrogen storage have been considered and tested.

One possible way to reduce heat of formation is by introducing a new chemical species that either has a negative heat of mixing and forms compounds with Mg or react with both Mg and hydrogen to form a ternary hydride [54]. In the first case a classical example is 5% Si doped Mg: upon desorption Mg will form an intermediate compound with a reduction in enthalpy of 40 kJ mol^{-1} (see figure 2.9), which won't be released in the successive hydriding reaction. However, the MgH_2/Si system was not readily reversible; hydrogenation of Mg_2Si appears to be kinetically limited because of the relatively low temperature, <150 °C, required for hydrogenation at 100 bar. In fact thermodynamic calculations indicate equilibrium pressures of 1 bar at approximately 20 °C and 100 bar at approximately 150 °C. The clear drawback is the reduction of storage capacity from 7.6 to 5% of hydrogen.

In the second case the addition of the new element results into a destabilized hydrogenated state. Mg is often immiscible with late transition metals. However, if a ternary hydride is formed, where hydrogen acts as a binding component, and the hydrogen per magnesium atom ratio is enhanced by the addition, this could result in a favourable influence of the reaction enthalpy per hydrogen molecule. The complex hydride Mg_2FeH_6 is such an example. This material is interesting because it has the highest known volumetric hydrogen density of 150 kg m^{-3}, which is more than double that of liquid hydrogen, and a gravimetric hydrogen density of 5.6 wt%. It is however difficult to synthesize and it doesn't show an appreciable reduction in enthalpy of formation [55]. Recently, by using high pressures in the GPa range or thin film processing, a significantly lowered hydrogen bonding enthalpy has been reported for $Mg-Sc-H$ and $Mg-Ti-H$ [56]. While $Mg-Sc-H$ would be

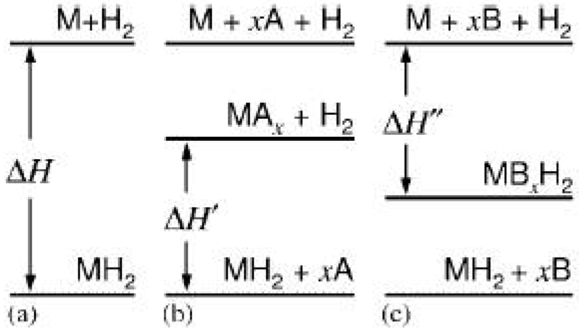

Figure 2.9: Scheme which shows two ways to reduce formation enthalpy by introducing a new species: (a) normal case; (b) added species A forms a compound with Mg resulting into a metastable state with reduced enthalpy difference with the hydride phase; (c) added element B creates a destabilized hydrogenated state.

too expensive for commercial applications, $Mg_{1-y}Ti_yH_x$ would be an interesting hydride if it could be produced at moderate pressures for bulk materials: it has to be substantially less stable than the respective competing $MgH_2 - TiH_2$ composite and thus has to be reversibly formed in the hydrided state. Till now, however, successful hydride formation at low temperatures and stability upon cycling has been reported only for thin film systems [57], which have very peculiar characteristics, as it will be shown in the next section.

Another method to destabilize Mg–H bonds is mixing with other light metal hydrides, whose metal reacts exothermically with Mg upon desorption (Reactive Hydride Composites). Examples are $MgH_2 + NaBH_4$ and $MgH_2 + LiBH_4$, which form MgB_2 during desorption and can be reversibly hydrogenated: with the combination of low reaction enthalpies and theoretic reversible hydrogen storage capacities of 7.8 and 11.4% wt, respectively, these RHC are very promising candidates for hydrogen storage materials [58].

Strictly connected to thermodynamic properties is the thermal management issue. Developing strategies to reduce the heat generation and to provide efficient heat removal during the hydriding reaction is essential to provide optimal energy utilization efficiency and fast kinetics for metal hydrides. DoE requirements demand a reaction rate for the hydride formation on the order of 1.5 kg H_2 min^{-1}. For Mg, with an enthalpy of hydride formation of 75 kJ mol^{-1} H_2, approximately 1MW of heat over more than 3 min is generated for 5 kg of H_2: assuming no heat removal (this is a reasonable assumption considering that a very low thermal conductivity of $\approx$ 0.1 W $m^{-1}K^{-1}$ in milled hydride powders has been reported [59]) in the hydride during the hydriding reaction, the temperature rise can be estimated from $\Delta T = \frac{Q}{nC}$ where Q is the heat supplied to the system, C the conductivity and n the number of moles. For metallic Mg, which has a specific heat of 24.9 J $mol^{-1}K^{-1}$, this gives a temperature increase on the order of 1000°C: without proper thermal management, this temperature increase would stop the hydriding reaction. Such large temperature excursions might even lead to local consolidation of the hydride which would destroy the nanostructure and prevent cyclability. A good thermal conductivity will also help during the dehydriding process by promoting the fast and uniform heating of the fuel tank required for a good rate of hydrogen release. In nanostructures, the thermal conductivity becomes a function of size and structure, and a low thermal conductivity value is usually derived for nanostructured materials due to size effects, such as porosity and nano-size [54]. Porosity will decrease the thermal conductivity due to the presence of poorly conducting gas gaps between particles. The thermal conductivity of H_2 is roughly three orders of magnitude smaller than that of Mg, leading to a significant barrier to thermal transport through the pore spaces, diverting the heat flow through the host material surrounding the pores.

For nanoparticles with a length scale smaller than the mean free path of the heat carriers, the thermal conductivity is reduced because the distance between successive boundaries becomes the effective mean free path. At room temperature, the phonon and the electron mean free paths lie between 10 and 100 nm for most materials. Since the thermal conductivity is proportional to the mean free path in the kinetic theory approximation, a 5 nm nanoparticle will have a thermal conductivity roughly 2–20 times smaller than its bulk counterpart.

The poor thermal transport properties of nanostructured materials can be improved by using conductive matrices to increase the heat transfer. The use of fins, foams, meshes and matrices formed by high conductivity materials like Cu, Al, Fe and Ni have been reported [60] and the use of expanded graphite/metal-hydride compacts were shown to increase the conductivity from 0.1 to 3 W m^{-1} K^{-1} [61] with only a 2.1 wt% graphite additive. This opens up the possibility of designing functional nanocomposites, where an external matrix could play the double role of increasing the heat transfer while being chemically active in promoting desirable thermodynamic and kinetic properties of the hydride.

2.3 Hydrogen in thin films

Thin films are quasi-two dimensional materials, where the third dimension (thickness) is greatly reduced in respect of the other two and usually ranges from a few atomic layers to hundreds of nm. They have unique properties significantly different from the corresponding bulk materials as a result of their physical dimensions, geometry, non–equilibrium microstructure and metallurgy: they are strongly influenced by surface, interface effects and under intrinsic stress caused by lattice misfit with the substrate on which they' re grown; they are not fully dense and present several defect structures. Thin films are often used as a model material, due to the easy control of microstructure and possibility of applying several complementary techniques.

The basic steps involved in the film deposition by condensation are: i) emission of particles from source, ii) transport of particles to substrate and iii) condensation of particles on substrate. Each step is very important for the final properties of the films but the most important is the growth of the film on the substrate. The growth step to form continuous film is divided into four stages: nucleation and island structure, coalescence of islands,

channel formation and formation of the continuous film [62].
It has been recognized that many important characteristics of thin film layers are related to the properties of grain boundaries and interfaces in these layers as well as the intrinsic properties of the materials involved. This is the consequence of the relatively small grain size and high density of boundaries in deposited films, which facilitate certain kinetics reactions by short–circuiting diffusion under conditions which could not possibly promote such reaction in bulk materials. This important property makes thin films an advantageous form of material for hydrogen storage because reaction kinetics for the uptake and release of hydrogen on nano–crystalline structures is much higher than on microcrystalline structures.
Research on hydrogen interaction with Mg in the form of thin films has been carried out since the work of Krozer and Kasemo [63]: they showed that by evaporating a thin Palladium layer on top of Mg the kinetic barrier for H_2 dissociation can be removed and hydrogen uptake can start even at 296 K and at low pressure (0.03–30 Torr); Pd layer also provides protection against magnesium oxidation. Atomic hydrogen then diffuses rapidly through the Pd film and also through the Mg layer, as long as the hydrogen concentration in the latter is low, i.e. in the dilute α phase. As the hydrogen concentration increases, the hydrogen mobility becomes lower up to null in magnesium, due to the nucleation and growth of a continuous MgH_2 layer at Pd/Mg interface, which prevents attainment of thermodynamic equilibrium between H_2 gas and hydrogen in magnesium. However by exploring the temperature dependence of the interface hydride formation, a region in the pressure–temperature (p–T) plane was found in which it is possible to attain thermodynamic equilibrium [36]: the higher the pressure is, the higher the temperature to prevent interface hydride formation.
Another issue is Mg–Pd intermixing. These two elements present a negative enthalpy of mixing of approximately -40 $kJ\ mol^{-1}H_2$ and form compounds of various stoichiometry [64]: raising the temperature results to be detrimental, because the Pd top layer mixes with Mg and finally is encapsulated by it, so that H_2 dissociation becomes difficult, being no more Pd on surface. It is however possible to avoid mixing by not raising temperature above 370–380 K, although a certain degree of mixing or alloying could be already present during the deposition process. The remarkable result of their measurements is the good agreement over 6 decades in gas pressure and over a temperature range of 500 K between low and high pressure data.

Higuchi et al.[65] synthesized by RF magnetron sputtering Pd capped–Mg thin films with different degree of crystallization: they found that, after hydrogenation at 0.1 MPa and 373 K for 24 hours, MgH_2 and non–crystalline Mg hydrides were formed in all the Pd/Mg films, where the hydrogen content reached 2.9 to 6.6 wt%. Desorption temperature was found to decrease with decreasing the degree of Mg crystallization, while the storage capacity resulted independent of it: temperatures as low as 473 K were recorded for desorption in vacuum. They suggested that amorphous hydride was less stable than the crystalline one, taking into account the higher hydrogen solubility in the former. Similarly, Checchetto et al.[66] by decreasing the thickness of MgH_2 film attained a desorption temperature up to 80°C, which is the basically required desorption temperature for the on–board usage of hydrogen. They showed that the production of such a thin film hydride leads to the formation of different lattice defects and crystalline stress level in the film which in turn allows the control of the desorption kinetics.

It must be pointed out that the remarkable achievements in hydrogen absorption–desorption attained for thin films can be hardly transferred to powders, which are thought to constitute the "hydrogen tank" in cars; nevertheless, thin films represent an easy method of synthesis for both theoretical and application–oriented fields. They're particularly suited for combinatorial techniques: in fact great efforts in hydrogen storage research are currently spent on multiple–elements composites in order to overcome limitations of simple binary hydrides; however the number of possible combinations and parameters is quite huge and so very time–consuming. Thin films allow fast and efficient exploration and analysis which are not possible for bulk chemical methods: for example, by synthesizing films with a compositional gradient it is possible to rapidly characterize alloys/solid solutions with different concentrations of elements in parallel [67].

Moreover several technological applications for thin films, such as in batteries and coatings, have been proposed since 1995, when Huiberts et al. [68] discovered spectacular changes in the optical properties of metal–hydride films of yttrium and lanthanum near their metal–insulator transition. It was found that the dihydrides are excellent metals and shiny while the trihydrides are semiconductors and transparent in the visible part of the optical spectrum. The transition is reversible and can be simply induced by changing the surrounding hydrogen gas pressure or electrolytic cell potential; because of this reversible behaviour, they were called "switchable mirrors" (SM). Since that discovery, three classes of switchable mirrors have been found: Rare Earth SM, Mg–Rare Earth SM and Mg–Transition Metal SM. The presence of Mg has a particular importance: in fact Rare Earth SM have a characteristic colour in the fully hydrogenated state because their band gap is in the visible ($Eg < 3$ eV). Alloying with Mg results in color neutrality and higher transparency, an essential property for devices such as smart windows [69]. Some of foreseen applications of switchable mirrors are: smart coatings [70], hydrogen indicators for catalytic and diffusion investigations, active layer in fiber optic hydrogen sensors [71] and hydrogen absorption detectors in a combinatorial search for new light–weight hydrogen storage materials [67].

Chapter 3

An experimental technique

3.1 Grazing incidence X-ray diffraction

X-ray diffraction (XRD) is a versatile non-destructive characterization technique which relies on elastic scattering by electrons in atoms of x-ray photons, whose wavelength is of the same order of the atomic spacing in crystals (about 0.3 nm). Diffracted waves from each atom can thus interfere with each other, thus modulating the resultant intensity distribution, which results into sharp interference maxima if atoms are arranged in a periodic fashion as in crystals. From the resulting diffraction pattern it is possible then to extract information on distribution of atoms in materials. Bragg found that, for a given set of lattice planes with interplanar distance d, the condition for constructive interference is given by (3.1), where 2θ is the angle between the incident and diffracted beams, λ the x-ray photons wavelength used and n an integer.

$$2d\sin\theta = n\lambda \tag{3.1}$$

From Bragg's law it results that only certain combinations of θ and d allow constructive interference to occur, which thus gives information on the interplanar distances d characteristic of every material. The ”powder method” is one of the most used to characterize a crystalline material: the x-ray source and the detector rotate around the sample in a manner so that the relationship θ-2θ is mantained during the angular scan. Any time (3.1) is fulfilled a peak appears, whose position, intensity, shape and width provide structural information. In particular the Full Width at Half Maximum of the peak is related to the average size (in Å) of the crystallites producing it through the Scherrer formula (3.2), where β stands for either FWHM or integral breadth and the subscripts h k l refer to the miller indices of the planes.

$$D_{hkl} = \frac{0.9\lambda}{\beta\cos\theta} \tag{3.2}$$

If the θ-2θ method described above is very good for polycrystalline powders, it can lose effectiveness for thin films deposited on a substrate, whose contribution to the diffracted signal can overshadow that of the film of interest. Hence Grazing Incidence (angle) XRD technique is used to minimize the signal from the substrate. Diffraction measurements are performed with a small constant incidence angle, usually fixed in the angular range between the critical angle and 2°, while the detector is moved across the 2θ range of interest (figure 3.1). The advantage of this asymmetric geometry is the reduced penetration of the beam into the substrate, thus reducing its contribution to the diffracted signal. Moreover planes with different orientation can be analyzed within one scan, in contrast to the symmetric geometry, in which only those parallel to the substrate can diffract. Clearly, if the substrate is amorphous or single crystal, the advantage of using GIXRD configuration in part vanishes.

GI-XRD measurements are performed with a X'Pert Pro Extended MRD apparatus, in which the divergent x-ray beam generated by a Cu anode ($K_{\alpha 1} = 1.5406$Å) is converted by an x-ray mirror with a parabolic shape (figure 3.2) in a more intense quasi-parallel beam (10 times), which is then directed to the sample; the diffracted beam passes through a parallel plate collimator with an equatorial acceptance angle of 0.27° before reaching the detector. Soller slits can also be used to control the axial divergence. In this configuration K_β radiation is suppressed to a level below 0.5% of its original value.

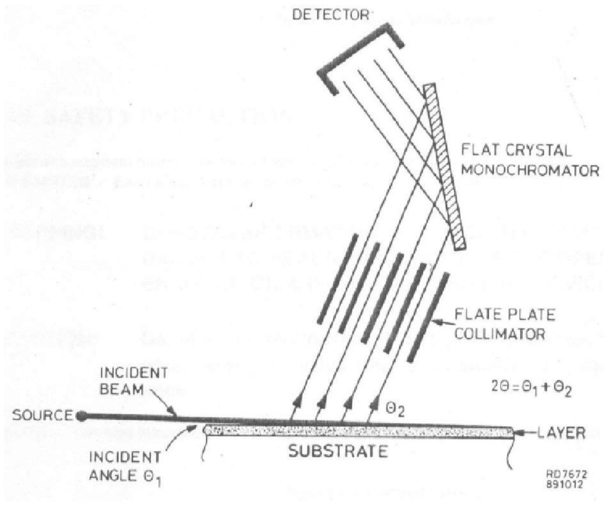

Figure 3.1: Asymmetric geometry of GI-XRD measurements: the angle of incidence is usually fixed in the angular range between the critical angle and 2°.

In-situ desorption measurements are allowed in the diffractometer by using a domed hot stage tool (figure 3.4), which is designed for diffraction measurements at controlled temperature under inert gas or vacuum. The dome is made of PEEK, a synthetic material based on polyetheretherketone, which allows temperature homogeneity in an inert atmosphere, N_2 in our case. The heating plate (figure 3.5) can reach temperatures up to 900°C: the reported difference between the read temperature and that of the sample is less than a degree °C for the temperatures considered in this work. A typical result of continuous

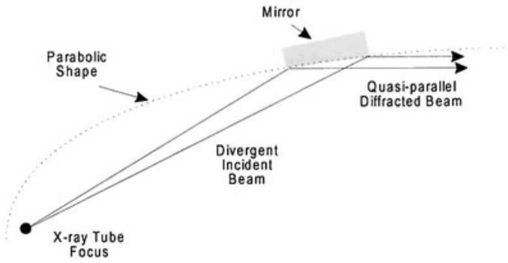

Figure 3.2: X-ray mirror to convert divergent beam from a line focus into a quasi-parallel beam.

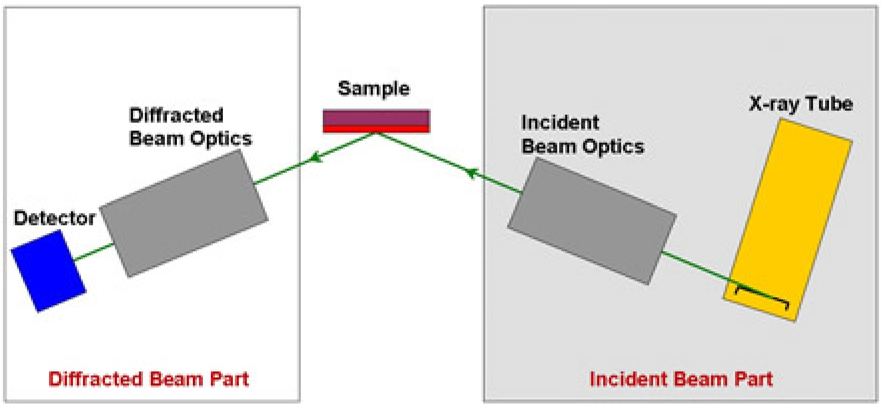

Figure 3.3: Schematic of X'Pert Pro MRD diffractometer.

diffraction scans is reported in figure 3.6a: each peak is fitted with a Voigt-type function and the resulting integrated intensity, position and FWHM are displayed and collected by a coded procedure. A time tag is assigned to each peak and then a normalized-intensity vs time graph is generated (figure 3.6b); the resulting kinetics is fitted with the Johnson-Mehl-Avrami nucleation and growth rate equation $\alpha(t) = 1 - exp(-(kt)^n)$ [72, 73, 74]. The reaction order n and the rate constant k are finally given by a Levenberg–Marquardt fitting algorithm [75, 76].

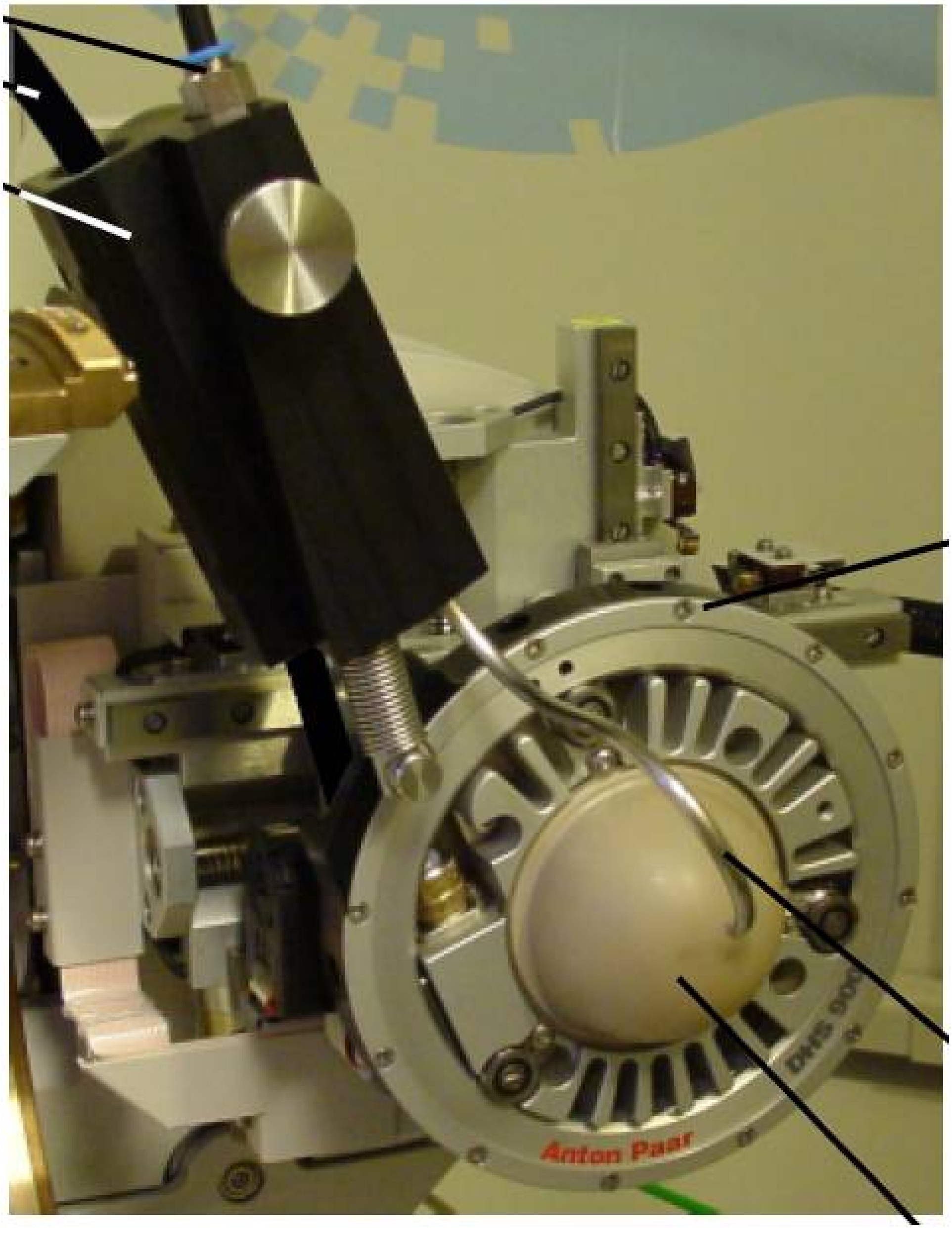

Figure 3.4: Domed hot stage for diffraction measurements at controlled temperature and under inert gas or vacuum.

Figure 3.5: Particular of the sample holder.

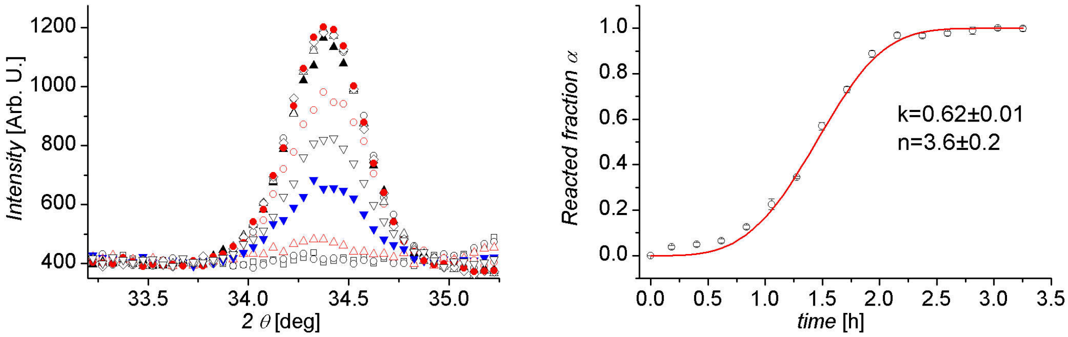

Figure 3.6: Example of continuous diffraction measurements (left) and the resulting kinetics (right) with the extracted n and k value.

Chapter 4

Pd capped–Mg thin films

4.1 Introduction

Magnesium hydride, MgH_2, is one of the most studied reversible hydrides, due to its high gravimetric hydrogen density (7.6 wt%) and energy density (9 MJ/kg); moreover upon hydrogen absorption and hydride formation, magnesium as other hydrides shows interesting electrical and optical properties, which are reflected in a metal–to–insulator transition: this pushed the development of new Mg-based devices as gasochromic switchable mirrors, which could have technological applications as sensors, smart windows and variable reflection coatings [70, 77]. Currently a lot of research effort is focused on the relation between microstructure, functional properties and reliability: concerning this point thin films constitute a model material, due to the easy control of microstructure and the possibility of using complementary characterization techniques [67, 78, 79]. Many observations are reported in literature concerning the dynamics of the metal-to-hydride phase transition in Pd capped Mg thin films. Experiments suggest that: i) the hydride phase starts nucleating at the Pd/Mg interface, ii) the diffusion of hydrogen through the hydride phase is the rate limiting step in the hydride formation, while, during hydride decomposition, the H diffusion is controlled by Mg [80]. Given the role of defects in the H diffusion process, it is thus not surprising that the hydrogen desorption kinetics results improved in Mg thin films with smaller grain size and/or decreased crystallinity [81, 66]. Recent studies revealed that in epitaxial Mg thin films the MgH_2 phase forms epitaxially relative to Mg film and that the MgH_2/Mg interface (when the metal–to–hydride phase transition is not complete) is a nucleation site for Mg during the process of hydride decomposition as well as the MgH_2/Pd one [82]. Consequence of the presence of two different nucleation sites for Mg in the hydride decomposition is a reduced degree of epitaxial re–growth in the Mg film: this finding has a more general character because a reduced crystalline degree of the regrown Mg layers was also observed in textured Mg film.

We present a study on the relation between the evolution, upon successive H_2 cycling, of the crystalline degree and the H_2 sorption properties of textured Mg thin films grown on Si and glass substrates. A Pd thin cap layer of 5-10 nm was added to promote hydrogen dissociation and to prevent magnesium oxidation [63].

4.2 Experimental

Pd capped–magnesium thin films, with a Cr buffer layer, were deposited on Si and glass substrates by r.f. magnetron sputtering. Depositions were done in a custom built r.f. magnetron sputtering system (13.56 MHz) equipped with 3 independent 2" sources and a r.f.–biased sample holder. The magnetron sputtering sources were positioned at a $\approx 30°$ inclination to the substrate normal and a target-to-substrate (center to center) distance of 12 cm. The sample holder, on the ceiling of the vacuum chamber, was rotated at 5 r.p.m. in order to assure a deposition uniformity better than 5%. Chromium, magnesium and palladium layers were deposited, in sequence, onto silicon wafers and fused silica slabs. The natural oxide on the Si wafers was removed by dipping in concentrate HF. These samples were then rinsed in deionized water and stored in isopropanol. Silica slabs were washed with a detergent, rinsed with deionized water and ultrasonically cleaned in trichloroethylene, acetone and isopropanol. Once in the sputtering chamber, the substrates were sputter-cleaned at a power of 20 W for 20 min in order to remove any residual surface contamination (in these conditions we measured a 10nm-thick sputtered layer for silica). The Cr layer was sputtered at first onto the cleaned substrates in order to assure a good adhesion of the Mg layer. Targets materials were 2" diameter Cr (99.9%), Mg (99.95%) and Pd (99.99%) disks. Sputtering was performed in pure Ar (99.9995%) at a pressure of $4 \cdot 10^{-3}$ mbar. The base pressure was better than 10^{-6} mbar. Before starting the depositions, sources were conditioned for 15 min. at the operating conditions. Depositions were performed at room temperature. Powers delivered to the sputtering sources were 50 W, 20W and 10 W for Cr, Mg and Pd, respectively. Sputtering times were 50 s, 3300 s and 700 s for Cr, Mg and Pd, respectively. The elemental composition of the films was measured by Rutherford Backscattering Spectroscopy (RBS) using a 2 MeV $^4He^+$ beam at Laboratori Nazionali INFN of Legnaro (Padova). The structural characterization of the films was carried out by Grazing Incidence X–Ray Diffraction (GIXRD) (with typical incidence angle θ=0.8°) in parallel beam geometry with a Panalytical X'Pert Pro MRD diffractometer equipped with a parabolic mirror in front of a CuK_α X–ray source. Hydrogen absorption was attained in a pre-evacuated (P=$4.5 \cdot 10^{-5}$ mbar) stainless steel chamber filled with hydrogen (purity: 99.999%) at 1 bar and then heated at 100°C. For in-situ desorption measurements a heatable specimen holder (Anton Paar DHS 900 hot stage) has been used in the GIXRD apparatus. Diffraction patterns were acquired with integration time set to 5 s, the step size to 0.05° and the incidence angle to 0.8°. Desorption measurements have been also performed in UHV by means of Thermal Desorption Spectroscopy (TDS), where the heating rate was set to 9 K min^{-1}. Structural and compositional characterization was performed with a field-emission gun FEI TECNAI F20 (S)TEM Transmission Electron Microscope equipped with an EDAX Energy-Dispersive X–ray spectrometer. Surface morphology was then studied by a field-emission gun JEOL JSM 7001F SEM Scanning

Electron Microscope, also equipped with an Oxford INCA PentaFetX3 energy-dispersive X–ray spectrometer. Optical transmission spectra were recorded with a JASCO V-600 spectrophotometer in the 900-200 nm wavelength range.

4.3 Results

4.3.1 As deposited sample

From GIXRD measurements the as deposited sample results textured with an intense hcp-Mg(002) peak at 34.40° (ref. ICDD card D470770) (see Figure 4.1a); the other strong reflection corresponds to hcp-Mg (103) peak: similar results were obtained by Léon et al. [83] who found that substrate temperature and the evaporation rate control the structure of their film synthesized by vacuum and UHV evaporation using a resistive heating and electron beam, respectively. The average crystallite size is 75 nm, as estimated from Scherrer formula applied to hcp-Mg (002) reflection. The most intense reflection from the Pd cap-layer is the fcc-Pd (111) (ref. ICDD card P870643) one at 40.00°, from which we estimate an average domain size of 6 nm. Apart from smaller Mg and Pd peaks, a weak reflection is visible at $2\theta = 38.13°$: it may be a hint of Mg_xPd_y compound, which is already formed at Mg-Pd interface during deposition.

To better investigate the structure of the layers and of their interfaces, TEM analysis has

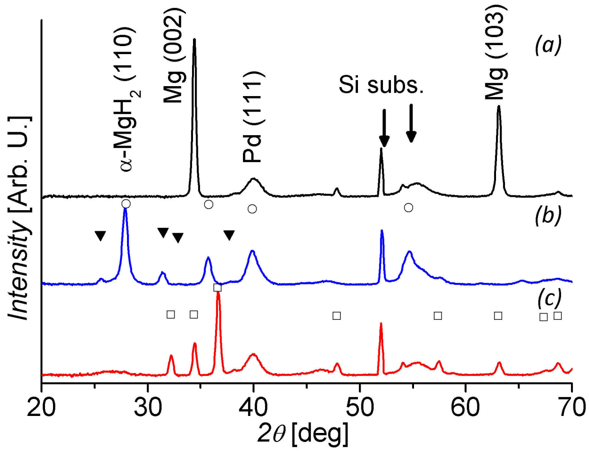

Figure 4.1: XRD patterns of the as deposited (a), hydrogen loaded (b) and desorbed films (c) deposited on silicon; □: hcp-Mg; ∘: α-MgH_2; ▼: γ-MgH_2.The loss of texture upon hydrogen absorption and desorption is clear.

been performed. Figure 4.2a shows the resulting cross-sectional bright-field TEM image: the different layers can be clearly distinguished. The total film thickness is about 200 nm with a high degree of roughness at the surface. The stack is composed of 6 nm of Cr, 170 nm Mg, 30-40 nm of a mixed Mg-Pd layer and 8-10 nm (partially discontinuous) Pd on top; a consistent result (table 4.1) is obtained by simulations [84] of the experimental RBS spectrum (see figure 4.3), where Mg-Pd mixing layer is assumed to have a Pd atomic fraction of about 10%. Elemental amounts of $20 \cdot 10^{15}$ Cr/cm^2, $800 \cdot 10^{15}$ Mg/cm^2, and $55 \cdot 10^{15}$ Pd/cm^2 are also estimated. The Cr layer results amorphous, while Mg is polycrystalline with texturing in the direction parallel to the growth direction and amorphous in some regions. The mixed intermetallic Mg-Pd layer has a varying composition along its thickness as can be seen by EDS: it is mainly amorphous with small domains, about 5÷15 nm, compatible with hcp-Mg_5Pd_2 (ref. ICDD card P220713) ordered alloy found through HR-TEM mode (figure 4.4a). The occurrence of Mg-Pd mixing and alloying is not surprising if one considers their binary alloy phase diagram and the enthalpy of mixing $\Delta H_{mix} = -40 kJmol^{-1}$ [85]. Finally, the Pd cap layer results irregular and polycrystalline, with the presence of MgO and PdO domains on the surface.

Layer	As dep RBS [nm]	As dep TEM [nm]	H-loaded TEM [nm]	Desorbed TEM [nm]
Pd	7	0÷10		
Pd–Mg	23	30÷40	60÷80	70÷100
Mg	160	155÷170	230	70÷120
Cr	6	6÷7	6÷7	6÷7
Entire film	196	≈215	≈300	≈200

Table 4.1: Layer thicknesses as extracted from RBS and TEM Bright-field images. For H-loaded and Desorbed samples a Pd layer cannot be distinguished.

SEM measurements of the surface reveal that, beside zones covered by Pd (figure 4.5a), which resemble the underlying columnar morphology of magnesium, an interconnected structure is present, where elemental analysis evidenced an increase in oxygen content: this is related to MgO formation following Mg exposition to air due to presence of regions with low Pd coverage.

4.3.2 Hydrogen loaded sample

The as deposited sample was loaded in a pre–evacuated ($P = 4.5 \cdot 10^{-5}$ mbar) stainless steel chamber with hydrogen at 1 bar and then heated at 100°C for 5.5 hours. In the hydrogen-loaded film two different phases of magnesium hydride are present: the dominant tetragonal (α)(ref. ICDD card P120697) and orthorhombic (γ)(ref. ICDD card P351184), the latter of which is metastable and usually formed from the previous one under high compressive stress [33]. Peaks at 27.87° and 35.70° (figure 4.1b) can be indexed as α-MgH_2 (110) and α-MgH_2 (101) respectively, while the $\alpha - MgH_2$ (200) one is masked by the fcc-Pd (111). The strongest peaks belonging to the orthorhombic phase are those at 25.62°,γ-MgH_2 (110), and 31.42°, γ-MgH_2 (111). Hydride peaks are broader than the metal ones, resulting in a crystallite size of 15 nm. No residual magnesium reflections are visible in the pattern. Moreover the strong α-MgH_2 (110) reflection recalls the orientation relation between hexagonal Mg (001) plane and α-MgH_2 (hk0) plane [86]: in fact also the tetragonal

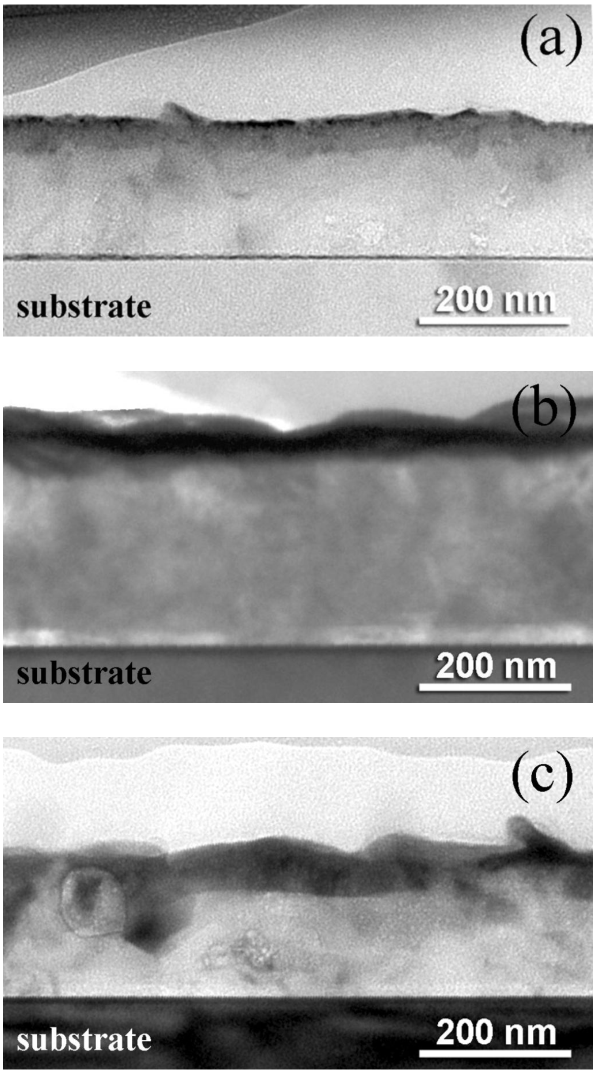

Figure 4.2: TEM Bright-field images of the as deposited (a), hydrogen loaded (b) and desorbed sample (c). The progressive disruption of Pd cap layer and Mg-Pd mixing is apparent.

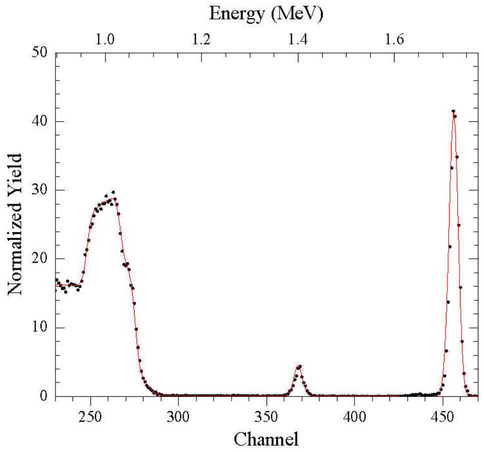

Figure 4.3: RBS experimental spectrum (dots) with the simulated one superimposed on it (continuous line). Peaks from higher to lower channels correspond to Pd, Cr, Si and Mg respectively.

hydride phase presents a certain degree of texturing. From TEM observations (figure 4.2b) we find that Pd is almost mixed with Mg and from HR-TEM Mg_5Pd_2 and MgO lattice planes are visible at the surface: this is probably consequence of Mg migration towards the surface upon annealing, which could be detrimental for both Pd cap layer integrity and its catalytic properties, as will be discussed in section *Discussion*. Also EDS confirms the increase in oxygen content in near surface regions, due to the failure of cap layer, with an atomic percent content doubled with respect to the as deposited sample. Oxygen comes from the air, during TEM sample preparation. The film thickness is 40% greater than the unloaded sample, mainly due to the out of plane expansion following hydride formation: in fact magnesium hydride formation was identified by HR-TEM through all the Mg layer. Moreover, large compressive stresses are generated in the in-plane direction, because of clamping to the substrate. A smaller contribution to film expansion could come from the oxidation of magnesium near the surface, as the cell volume increases. Concerning this point, similar test samples with a better Pd coverage showed upon hydrogen absorption a smaller film expansion in this region, due to improved cap layer strength, which prevented magnesium oxidation.

4.3.3 Desorbed sample

Preliminary measurements performed on test samples have shown that desorption is hindered at temperatures below 130°C in N_2 flux or in vacuum: the only way to induce desorption at these temperatures is through exposure to air or oxygen mixed with a inert carrier gas. This agrees well with studies performed on similar systems [70, 87] . After 2 hours at 100°C in air the sample results almost desorbed: the hcp-Mg (002) peak reappears but is reduced in comparison to the initial one; moreover other Mg reflections are visible, among which the ones at 32.22°, hcp-Mg (100) and 36.66°, hcp-Mg (101) (figure 4.1c).

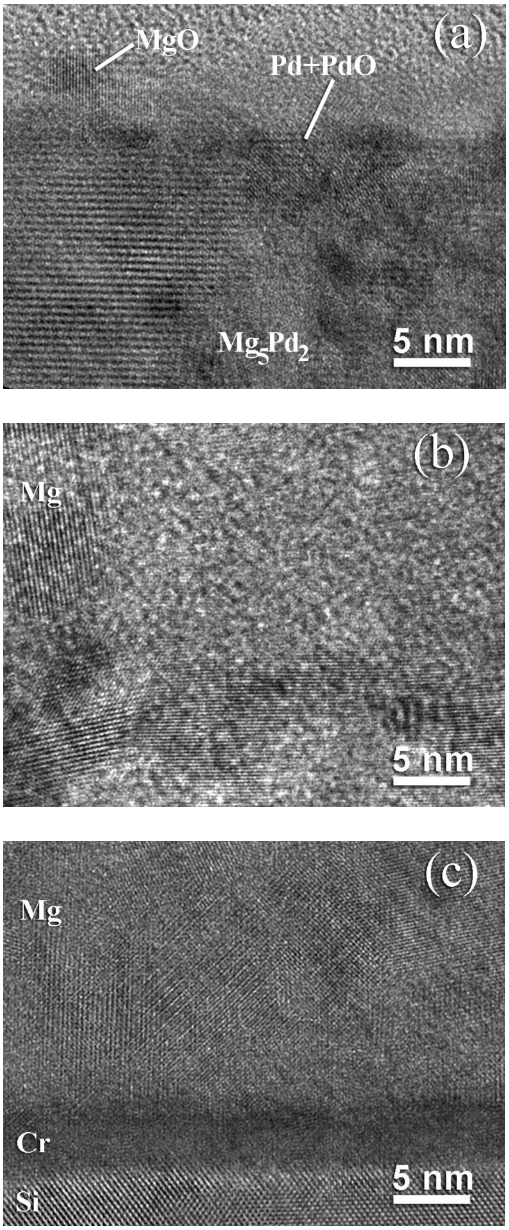

Figure 4.4: HR-TEM images of the as deposited sample on silicon: (a) surface zone, (b) middle zone, (c) film-substrate interface zone.

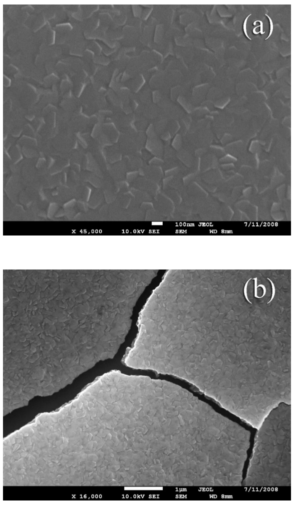

Figure 4.5: SEM micrographs of the surface: (a) as deposited and (b) desorbed sample.

From Scherrer analysis of the (002) peak, we estimate an average crystallite size of about 70 nm. Therefore, within one sorption/desorption cycle, texture is completely lost and the intensity distribution among hcp reflections resembles well a polycrystalline sample with randomly oriented nanograins. On the other hand, a previously partially hydrogenated sample (figure 4.6), under the same desorption conditions, shows a textured Mg re-growth (figure 4.7): this is a hint that Mg/MgH_2 interface is a nucleation site for Mg [82]. By comparing the cell parameters, calculated through fitting all Mg reflections available, it comes out that the desorbed sample, which has been fully loaded previously, has a Mg cell slightly greater than the previously-partially-loaded desorbed one; both, however, have a hcp c–axis smaller than the as deposited one (table 4.2), which could be due to an increased Mg–Pd mixing, according to the smaller metallic radius of Pd (1.40 Å) compared with Mg (1.60 Å). Moreover from peak intensity integration we found that the lower value for the desorbed sample suggests crystallinity loss. TEM images support this finding: the film has a sponge–like structure and amorphous zones are more frequent. The mixed intermetallic layer now extends to 70-100 nm (table 4.1) and MgO is widely present on surface with traces of magnesium hydroxide, as identified by HR-TEM mode. SEM measurements showed both oxide structures, like those present on the as deposited sample, and zones of film cracks and detachment from the substrate (figure 4.5b).

4.3.4 Desorption kinetics measurements

The hydrogen desorption process was studied by continuously acquiring XRD scans of the lowest order hcp–Mg (002) and α-MgH_2 (110) reflections using a heatable sample holder. Assuming a Voigt–type profile for the peaks, their integrated intensities are considered as directly proportional to the volume of the phase producing the reflection [88]. We consider only these two peaks due to the trade–off existing between time resolution and counting statistics. It must be pointed out that in this way only the crystalline phases

	hcp-Mg cell parameters		
sample	a [Å]	b [Å]	c [Å]
Reference value	3.2095	3.2095	5.2104
As deposited	–	–	5.210(1)
Vacuum annealed	–	–	5.190(1)
Partially loaded and desorbed	3.203(1)	3.203(1)	5.204(1)
Fully loaded and desorbed	3.206(1)	3.206(1)	5.205(1)
Vacuum annealed, loaded and desorbed	3.204(1)	3.204(1)	5.201(1)

Table 4.2: Mg cell parameters calculated by fitting available polycrystalline Mg reflections (TREOR). Values in parentheses are uncertainties from the fit.

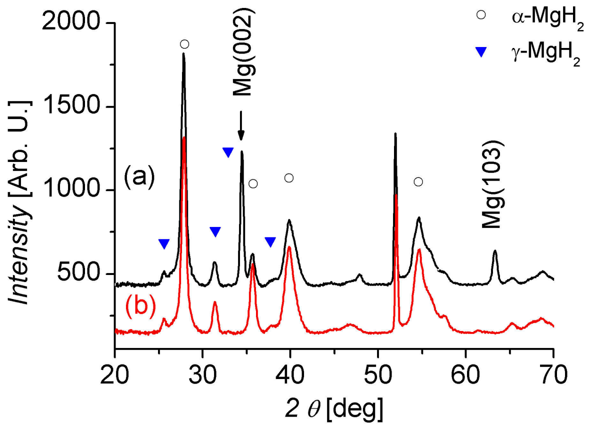

Figure 4.6: Diffraction patterns of partially (a) and fully loaded (b) samples. Mg reflections are still present in the former.

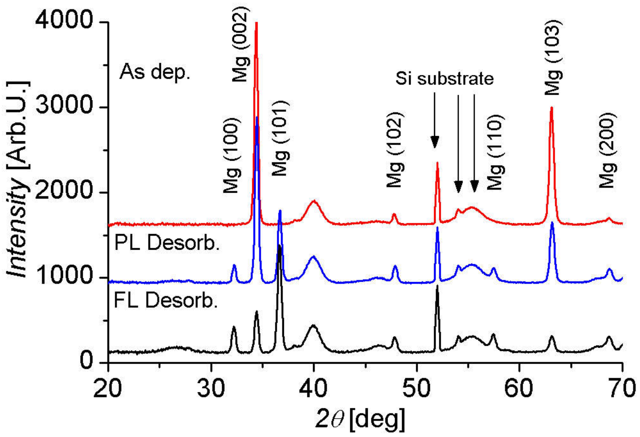

Figure 4.7: Diffraction patterns of the as deposited, partially loaded (PL) and fully loaded (FL) samples after desorption. It is apparent that Mg re-grows along (002) direction in the PL sample.

can be monitored and nothing can be said about the amorphous fraction of the sample. The Johnson-Mehl-Avrami nucleation and growth rate equation (chapter 3) was used to fit the experimental data (4.1) for MgH_2 and Mg with the *reacted fraction* α being related to the reacted volume at time t.

$$\begin{aligned} MgH_2\text{:} \quad & \alpha_1(t) = exp(-(kt)^n) \\ \text{Mg:} \quad & \alpha_2(t) = 1 - exp(-(kt)^n) \end{aligned} \tag{4.1}$$

The reaction order n and the rate constant k were taken as free parameters in a Levenberg–Marquardt fitting algorithm [75, 76]; extracted values are reported in table 4.3. The spread in fitted n values is probably due to the difficulty in estimating first points in Mg and MgH_2 kinetics and not to a variation of reaction order. However, fitted rate constant k is quite insensitive to n variations, provided that the rate equation is the same, so an Arrhenius analysis can be performed. The complete desorption time is estimated as about 5 times the reciprocal of rate constant k. It is interesting to note that the dependence on time of α-MgH_2 (110) reflection's decrease and that of hcp-Mg (002) growth are consistent, indicating once more the orientation relation between them. Assuming an Arrhenius type expression (4.2) for the desorption rate constant, where k_B is the Boltzmann constant, T the temperature, A the apparent pre-exponential factor and E_a the apparent activation energy for the process, *in-situ* desorption measurements were performed in air at different temperatures to extract E_a and A. The loading conditions were the same as those described above.

$$k(T) = A\, exp\left(-\frac{E_a}{k_B T}\right) \tag{4.2}$$

We measured the desorption kinetics after one and two absorption cycles, in order to study the influence of cycles on the functional properties of the film. In all cases desorption was

	Rate constant k[h^{-1}]			
T[°C]	MgH_2 1^{st}	MgH_2 2^{nd}	Mg 1^{st}	Mg 2^{nd}
60	0.384 ± 0.003	0.40 ± 0.03	0.378 ± 0.003	0.39 ± 0.01
	$(n = 1.91 \pm 0.06)$	$(n = 1.99 \pm 0.09)$	$(n = 1.75 \pm 0.03)$	$(n = 2.0 \pm 0.1)$
70	0.64 ± 0.01	0.89 ± 0.03	0.62 ± 0.01	0.82 ± 0.01
	$(n = 3.7 \pm 0.1)$	$(n = 1.9 \pm 0.1)$	$(n = 3.6 \pm 0.2)$	$(n = 3.1 \pm 0.1)$
80	1.48 ± 0.03	1.70 ± 0.06	1.47 ± 0.06	1.72 ± 0.09
	$(n = 3.5 \pm 0.2)$	$(n = 2.7 \pm 0.3)$	$(n = 3.8 \pm 0.6)$	$(n = 2.5 \pm 0.6)$
90	2.49 ± 0.06	5.7 ± 0.4	2.35 ± 0.06	5.31 ± 0.4
	$(n = 2.1 \pm 0.1)$	$(n = 2.2 \pm 0.3)$	$(n = 2.1 \pm 0.3)$	$(n = 1.88 \pm 0.8)$
100	4.2 ± 0.2	–	4.1 ± 0.4	–
	$(n = 0.9 \pm 0.2)$		$(n = 2.9 \pm 0.9)$	

Table 4.3: Extracted values of n and the rate constant k for α-MgH_2(110) and hcp-Mg(002). Note that the rate constant at T=100°C for the 2^{nd} cycle is missing because the reaction was too fast in order to be measured with our experimental set-up.

almost complete, with small or no detectable residual (crystalline) hydride. In figure 4.8 the Arrhenius plot of the rate constant is reported for the 1^{st} and 2^{nd} cycle: a weighted linear fit provides the values for A and E_a. It is clear that the second desorption cycle is faster than the first; however, the corresponding apparent activation energy and pre-exponential factor are larger. The faster dehydrogenation kinetics for the 2^{nd} cycle could be related to decrease of Mg crystallization degree, as TEM images showed [81]. However, already at the third cycle the desorption kinetics slows down and complete desorption cannot be achieved even in 24 hours at 80°C at the fourth cycle (see figure 4.9): this is related to the Pd layer degradation, which results in an opposite stronger effect than the beneficial reduction of crystallization degree. The increase in oxygen content in the film, as shown by EDS and by the appearance of $MgCr_2O_4$ near the substrate, is a hint of decreased Pd catalytic and protective properties against Mg oxidation.

Huot et al.[89] found that magnesium hydride powders have an activation energy for desorption of 156 kJ mol^{-1} ($\approx$ 1.62 eV), with desorption lasting more than 50 minutes at 350°C in 0.015 MPa of hydrogen; concerning thin films, Checchetto et al.[78] found an activation energy of 1.13 eV for deuterium desorption in UHV from Pd capped Mg thin film. However, a direct comparison with the present measurements is not too meaningful, because desorption conditions are different (UHV vs air as in the present case).

It is interesting to compare the different evolution upon hydrogen cycling of an as deposited sample annealed in vacuum ($4.5 \cdot 10^{-5}$mbar) at 140°C for 6 hours. As shown in figure 4.10 d–spacing results lower (2θ higher) in respect of the as deposited state. That also seems to have a larger crystallite size. Probably Pd penetration in Mg, as suggested by fcc-Pd (111) reflection decrease and appearance of a Mg-Pd reflection (of crystallite size$\approx$ 30 nm), induces compressive stress on hcp-Mg. Moreover the reflection at $2\theta = 38.22°$ and

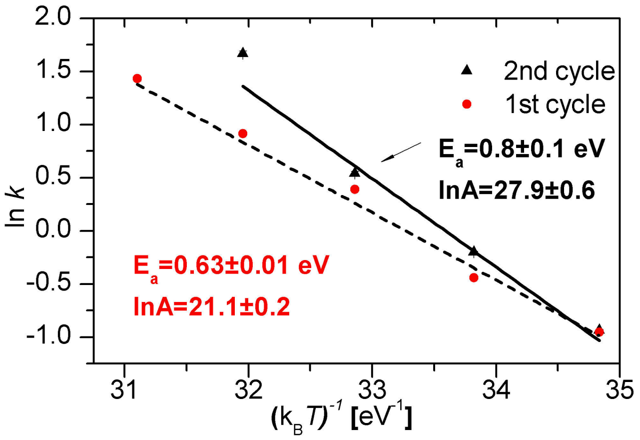

Figure 4.8: Arrhenius plot. Logarithm of the rate constant for MgH_2 decomposition versus $(K_BT)^{-1}$ for 1^{st} and 2^{nd} desorption cycle in air; error bars are masked by symbols. Extracted values for apparent activation energy and pre-factor are also reported.

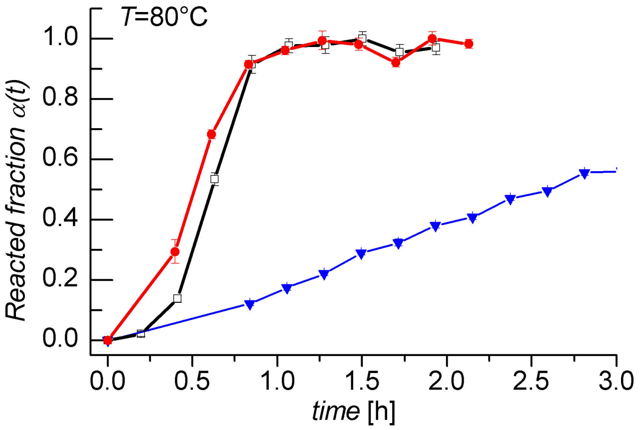

Figure 4.9: Desorption kinetics at T=80°C in air after one (□), two (○) and three (▼) hydrogenation processes. Lines are guides to the eye.

the weak broader one at about $2\theta = 26.1°$ are hints of Mg-Pd compound. Hydrogen loading can be achieved within 4.5h at P=1 bar and T=100°C; MgH_2 reflections are not shifted in comparison with those of the as deposited sample, while the Mg-Pd reflection decreases, probably as a consequence of partial hydrogenation of Mg-Pd mixed region (figure 4.11b). On the contrary, desorption results slower and incomplete even after 4h at 100°C in air figure 4.11c): magnesium is polycrystalline with smaller lattice parameters than the not annealed sample (table 4.2). This could be due to a higher Mg-Pd mixing, according to the smaller metallic radius of Pd (1.40 Å) compared with Mg (1.60 Å); annealing in vacuum with the consequent increase in Pd-Mg mixing speeds up film degradation in respect of the not annealed one: in fact fcc-Pd (111) reflection is almost unchanged after one cycle for the latter. This once more suggests the importance of the Pd on surface.

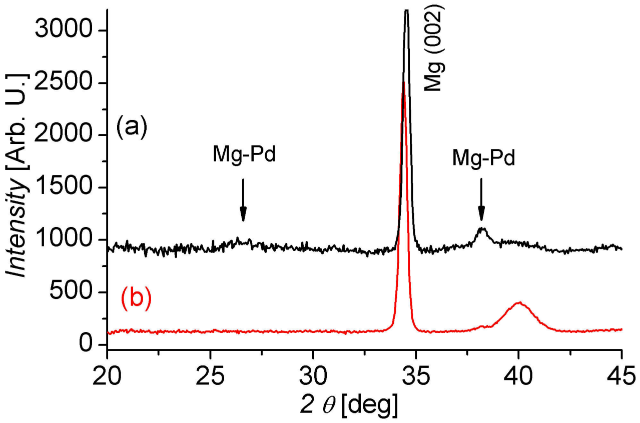

Figure 4.10: Comparison between diffraction patterns of the vacuum-annealed (a) and as deposited (b) sample. Annealing induces Pd (111) disappearance with formation of a new Mg-Pd reflection.

4.3.5 Optical transmission measurements

For the sample deposited on glass optical transmittance was monitored after hydrogen loading and desorption at 90°C for 2 hours in air, in order to check the metal–insulator transition related to hydride formation. In figure 4.12 spectra of the loaded and desorbed samples are reported: there's a lower transmittance after desorption, which suggests that some hydride is still present. In fact GIXRD patterns confirm the presence of residual MgH_2 peaks. Fringe pattern is compatible with the layered structure found by TEM analysis; however the lack of defined interfaces and roughness make a quantitative simulation difficult. What can be seen is an increase of the extinction coefficient compatible with a random nucleation and growth of the magnesium phase within the whole volume [90]; then, applying the "Tauc procedure" to the fringe–free part of the spectrum near the absorption

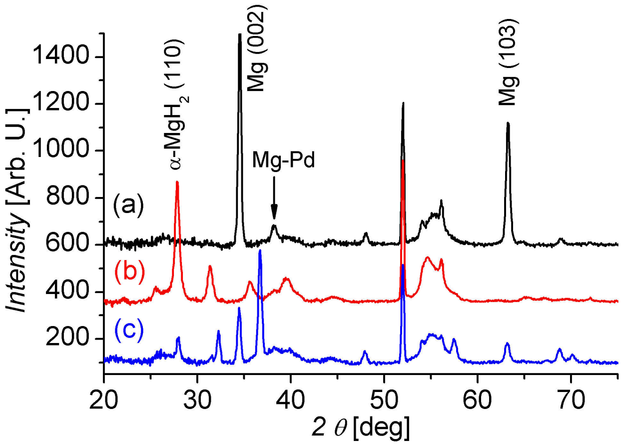

Figure 4.11: Diffraction patterns of the vacuum-annealed sample: (a) as annealed, (b) hydrogen loaded, (c) (partially) desorbed.

edge, the transmission follows (4.3).

$$\ln T(\omega) = \ln T_0 - C\frac{(\hbar\omega - E_g)^{\nu}}{\hbar\omega} \tag{4.3}$$

where T is the transmittance, $\hbar\omega$ the energy of the incoming light, E_g the band gap, C

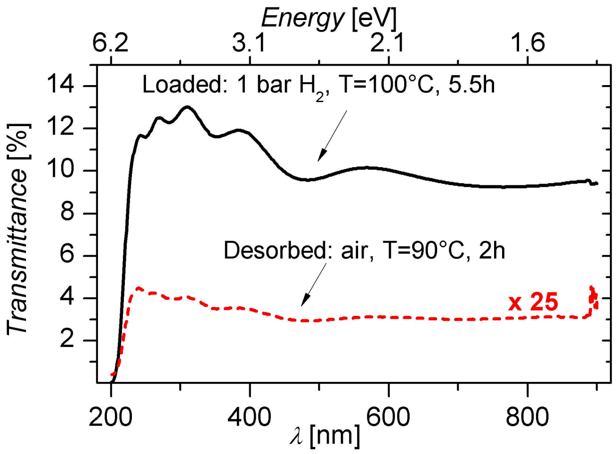

Figure 4.12: Optical transmission spectra for the loaded and desorbed samples: the desorbed one is magnified 25 times.

a constant, T_0 contains substrate contribution and the exponent ν depends on the type of transition [91]. Assuming $\nu = 2$, as it is reported to give the best results for nanocrystalline materials [92], we estimate that the band–gap for the entire film is $E_g = (5.4 \pm 0.1)$ eV, which is comparable to the literature value for MgH_2 , $E_g = (5.48 \pm 0.05)$ eV, found by Isidorsson et al.[91] . The same authors, however, pointed out that a more reliable estimation for the band gap is $E_g = (5.6 \pm 0.1)$ eV, which was obtained considering diffuse transmission instead of total transmission. Moreover, it could be that the value we found is affected by Cr buffer layer and Pd mixed with Mg: in fact Pd and Cr contribution are not comprised in T_0 term in (4.3).

4.3.6 Thermal Desorption Spectroscopy

In this case samples have been loaded with deuterium (D_2), in order to have a better signal-to-noise ratio [66]. TDS measurements, performed in Ultra High Vacuum (UHV), are reported in figure 4.13: the desorption spectrum consists of two peaks, a first one at T=154°C and a more intense one at 262°C. This is consistent with preliminary GIXRD kinetic measurements performed in vacuum and N_2 flux, for which no hydride dissociation was detected below 130°C. GIXRD patterns were recorded after the first and second TDS peak in order to correlate the structural evolution of the film sample and the hydrogen desorption process. To this purpose two similar samples were analyzed: one after annealing up to 170°C so that only the first TDS peak appears, the other after complete D_2 desorption. The XRD pattern of the first sample evidences only the presence of the α-MgH_2 reflections while no peaks due to the γ-phase are seen, indicating that the low temperature peak can be due to the dissociation of the γ-phase which is in fact metastable. We also observe that Mg dissociated from this phase has reacted with Pd, (see figure 4.14) producing polycrystalline Mg_5Pd_2 with a mean crystallite size of 50 nm. The α-MgH_2 (110) reflection is shifted to a higher angle (2θ =28.02°) and it is more intense than that of the loaded sample, indicating a compressive stress for hydride crystallites, which doubled in size after the thermal treatment in high vacuum. After the second desorption peak, only reflections due to fcc-Mg_2Si (ref. ICDD card P350773) and MgO (diamond structure, ref. ICDD card P300794) can be identified indicating that at temperatures higher than 262°C both the Mg fraction in the Mg_5Pd_2 phase and that in the α-MgH_2 hydride has reacted with the Si substrate (figure 4.15). In a previous study [66] Pd capped MgD_2 thin films were produced by thermal annealing in D_2 atmosphere of Mg films deposited on glass (Mg deposition occurred in UHV conditions by e-gun). The TDS spectrum of that sample showed a single desorption peak at T=100°C connected with the decomposition of the hydride phase. No solid state reaction of Mg with the Pd capping layer or the glass substrate was observed and the XRD pattern evidenced only Mg reflections. This difference in the structural evolution can be reasonably attributed to the much lower temperatures where D_2 desorption occurs, probably allowed by a better covering Pd cap layer.

4.4 Discussion

The studied Pd capped-magnesium thin film showed a lower activation energy for desorption than bulk magnesium and faster dehydrogenation kinetics in air, thanks to its nanostructure. Desorption in air is attained at low temperatures and seems to be the only viable way to dehydrogenate our samples: in fact, as shown in the previous section, desorption in UHV requires temperatures higher than 130°C, which leads to the loss of the original structure of the film. Dehydrogenation at low temperatures in air is related

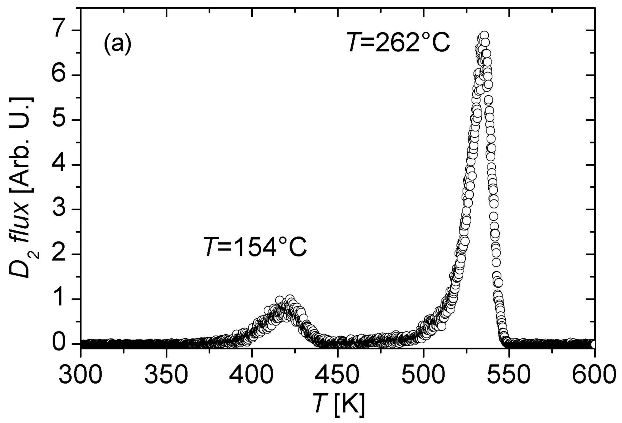

Figure 4.13: TDS spectrum for the sample loaded with D_2. The two peaks are related to processes with a different activation energy.

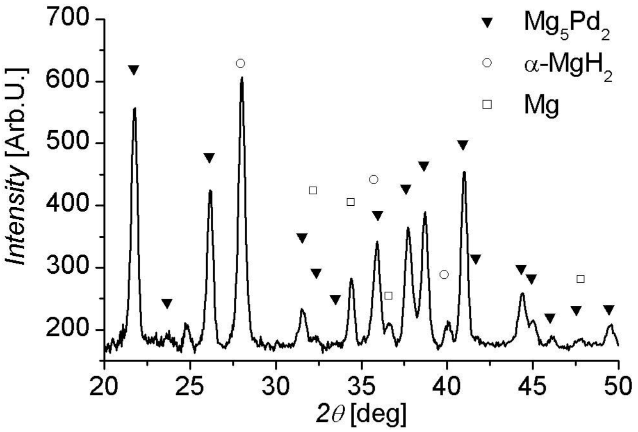

Figure 4.14: Diffraction pattern after the first desorption peak: the γ-MgH_2 phase has been decomposed and Mg_5Pd_2 has grown.

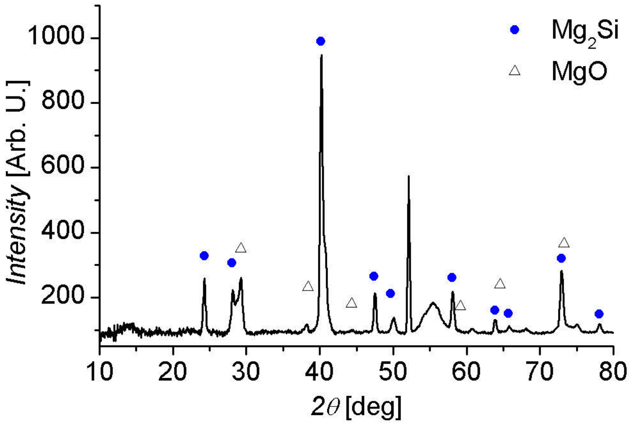

Figure 4.15: Diffraction pattern after the second desorption peak: hydrogen has desorbed, MgO has grown and some of Mg has reacted with Si substrate.

to the surface of the film, where Pd promotes recombinative desorption: the presence of oxygen on the surface can clearly offer a second path of desorption through water formation process [93]. It is frequently found in literature that hydrogen absorption is faster than desorption in vacuum for Pd capped-thin films: oxygen is then used to speed up hydrogen release [70, 87]; Pasturel et al.[94] showed that the different behaviour in sorption and desorption can be due to a much smaller gradient in the chemical potential induced during the desorption process. In fact the diffusion of hydrogen through a bi–layer system as in the present study depends strongly on the relative enthalpies of solution and hydride formation: because magnesium film has a stronger affinity for hydrogen than Pd, being the enthalpy of MgH_2 formation $\Delta H_f = -74.5\ kJ\ mol^{-1}\ H_2$, the enthalpy of H solution in Pd $\Delta H_s = -10\ kJ\ mol^{-1}\ H_2$ and PdH formation enthalpy $\Delta H_f = -41\ kJ\ mol^{-1}\ H_2$, the desorption is much slower than the absorption of hydrogen. Regarding activation energies, Borgschulte et al.[95] recently have found with their model that values extracted from kinetics measurements must refer to a process with several rate-limiting steps, in which surface dissociation of hydrogen and diffusion are interdependent mechanisms. Moreover Andreasen et al.[96] report about a dependence of activation energy on MgO content and explain the simultaneous increase of activation energy and prefactor with a compensation effect, originating from the Arrhenius analysis. Beside these effects, other processes at surface must be taken into account. As TEM analysis showed, Pd doesn't cover completely the Mg layer, which then oxidizes at the surface when exposed to air; moreover, during hydrogen absorption at 100°C Mg-Pd mixing increases, affecting Pd cap integrity [97]. The cell volume increase following magnesium hydride formation, which is about 30%, must be taken into account: it generates strain between Mg and Pd, whose expansion is up to 10% when hydrogen–loaded, and then it can lead to Pd fracture. All these processes could be responsible for the different behaviour of our samples between air and vacuum, as shown by Borgschulte et al. for YO_x and Mg_yNi_{1-y} [98, 99], who suggested that Pd is affected by a strong metal support interaction (SMSI), for which smaller Pd clusters are encapsulated in magnesium oxide or hydroxide, resulting catalytically inactive; then subsequent exposure to oxygen seems to restore the Pd on surface. This process results dependent on the number of sorption/desorption cycles, Pd layer thickness and presence of impurities. Moreover SMSI can explain the different behavior between absorption and desorption for the vacuum-annealed sample: it is likely that after annealing some Pd in the form of clusters is still on surface, thus allowing hydrogen molecule dissociation and migration towards Mg; desorption, instead, is kinetically limited by oxygen-induced restoration process of previously encapsulated Pd clusters.

Combined effects, relative to surface processes described above, strongly affect the cyclic stability of the samples: the incomplete coverage of the magnesium surface and its subsequent oxidation in air should be the most important. To overcome this problem either a thicker Pd layer is required or oxygen and other contaminants must be avoided through high vacuum–UHV conditions. However, even with thicker and well-covering Pd cap layers, cycling is detrimental, due to Mg migration towards surface, Mg-Pd mixing, Pd layer failure; therefore Slack et al.[100] suggested the insertion of a NbO_x buffer layer between Mg-Ni and Pd to prevent Pd-Mg mixing, so achieving an appreciable slowing down of absorption/desorption speed deterioration. Bao et al.[101] focused on Ti, Nb and V as buffer layers, due to their well known high hydrogen diffusivity: however also in that case degradation of properties could only be retarded by a factor 3, reaching 400-500 cycles. Slaman et al.[71, 102] had similar problems with their fiber optic hydrogen detectors, which seemed to be solved by the use of a protective coating against air humidity. Clearly, a better Pd wetting and control of Mg-Pd interface would improve the cyclability and properties of our thin films: such an improvement will be reported in the next section.

4.5 Improved Pd cap layer

In order to improve the Pd cap layer coverage and reduce mixing with Mg, new similar thin films were synthesized by adjusting the distance between the source and substrate in the sputtering chamber. Diffraction patterns are similar to the previously studied sample; on the other hand a different behaviour has been found in hydrogen absorption and desorption. In fact, for this new sample absorption is almost full in 7.5 h at P=1 bar and T=60°C, while for the old one it's only partial (figure 4.16); moreover desorption in air at 80°C is faster (figure 4.17) and TDS measurements show that there is a single desorption peak at about 115°C (figure 4.18). The reason of improved properties for this film can be understood by considering TEM micrograph of the as deposited sample reported in figure 4.19a and by comparing EDX depth profiles with those of the old one (Figure 4.20): it's apparent that Pd cap layer is almost continuous with a thickness of 9–12 nm and Mg doesn't reach the surface. However, as in the previous sample, a mixed Pd-Mg region extends for 30–40 nm between Pd and Mg layers and Mg_5Pd_2 grains are found in the sub-surface region. The estimated thicknesses for the layers are reported in table 4.4.

The film evolution with sorption/desorption cycles is the same as the previous sample, with a progressive fracturing of the Pd layer and mixing between Mg and Pd. After three cycles Pd is completely encapsulated in Mg as is shown in figure 4.19b: a Mg layer can't be distinguished and the the structure is sponge–like with the presence of voids up to Cr buffer layer.

From these findings it is clear that either a thicker Pd layer is required, with the drawback of reducing gravimetric density, or another way to improve cycling stability must be considered. In the next chapter we will explore Ti doping of Mg, for which peculiar structural properties have been recently found when synthesized in the form of thin films [57].

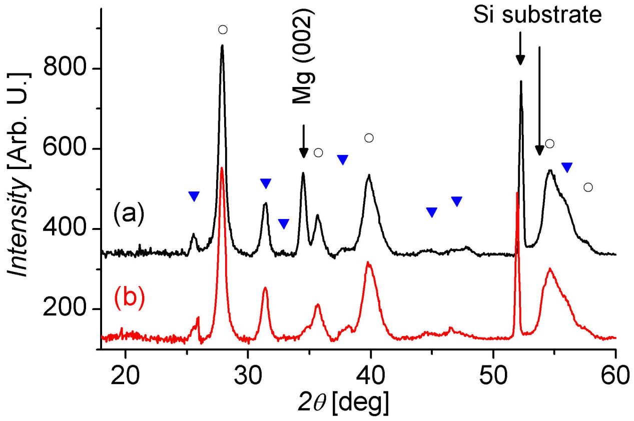

Figure 4.16: Comparison between old (a) and new (b) sample after Hydrogen loading at 1 bar, 60°C for 7.5 h; ○: α-MgH_2; ▼: γ-MgH_2.

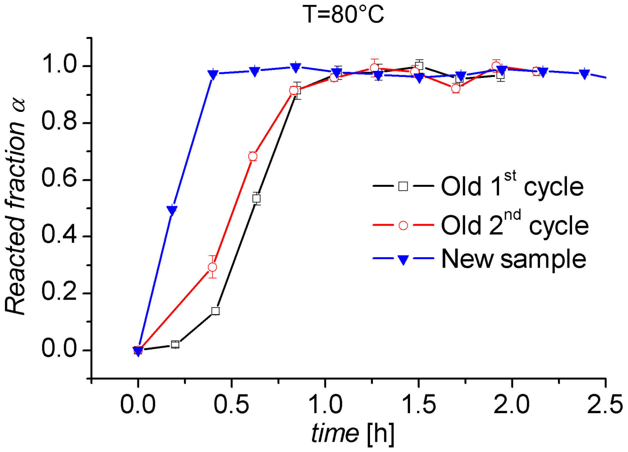

Figure 4.17: Comparison between desorption kinetics in air at T=80°C between the old and new deposition.

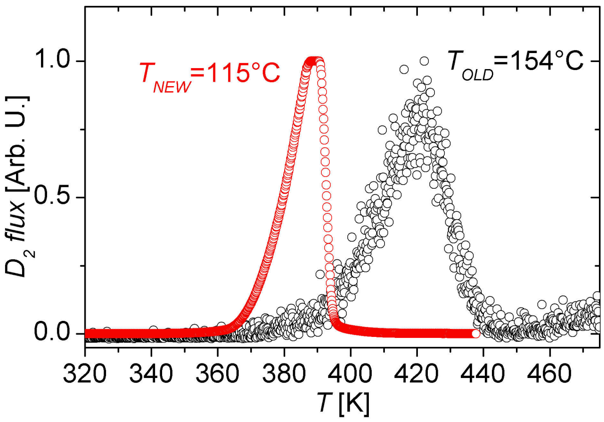

Figure 4.18: Comparison between TDS spectra between new and old sample. Note that the old one has another stronger peak at 262°C, which is not reported here.

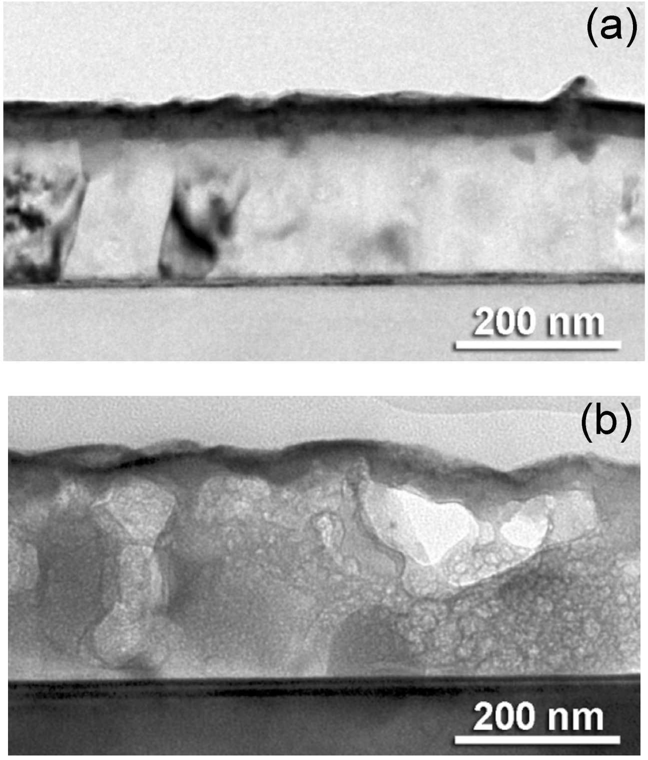

Figure 4.19: TEM micrographs of the new sample: as deposited (a) and after 3 cycles (b).

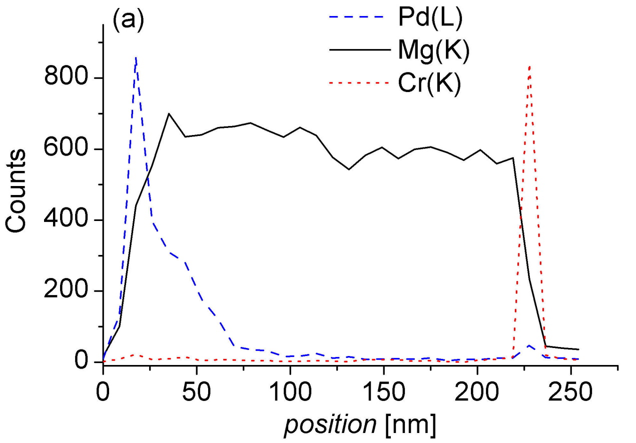

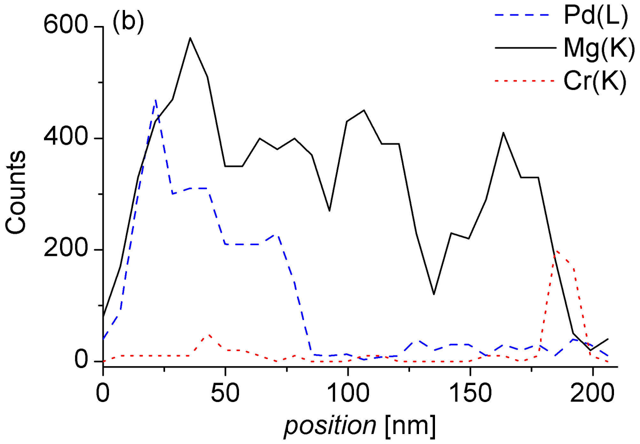

Figure 4.20: EDX depth profiles of the new (a) and old (b) samples. The Mg signal fluctuations in (b) are due to the presence of voids in the Mg layer.

Layer	As dep [nm]	Desorbed (3 cycles) [nm]
Pd	9÷12	–
Pd–Mg	30÷40	275÷295
Mg	170÷190	–
Cr	5÷8	5÷6
Entire film	≈230	≈290

Table 4.4: Layer thicknesses as extracted from TEM Bright-field images. For the Desorbed (3 cycles) samples Pd and Mg layers cannot be distinguished.

Chapter 5

Mg-Ti thin films

5.1 Introduction

Ti is a transition metal which upon hydrogen absorption forms hydride (TiH_2, $TiH_{1.9}$): its cell undergoes a transformation from a hcp to a fcc one. The enthalpy of formation is $\Delta H = -130\ kJ\ mol^{-1}H_2$, which is almost twice as negative as that of magnesium. Research on Mg-Ti system was pushed by the work by Notten et al.[103] in the search for high energy density and space–efficient batteries. In fact, beside hydrogen storage for transportation, hydride–forming materials can also be used in many other applications, for instance, as negative electrode material in rechargeable batteries. Commercially used Metal Hydride electrodes show hydrogen storage capacities of about 300 mAh/g, corresponding to 1.1 wt% ($LaNi_5$) hydrogen stored. It was shown that MgSc compounds exhibit very high storage capacities of up to six times that of the mischmetal-based materials. It was argued that, depending on the Sc content, the MgSc hydride is either rutile–structured or face–centered cubic structured of which the latter structure shows superior hydrogen transport properties [103, 104, 105]. In fact the slow desorption rate of α-MgH_2 is closely related to its rutile-type crystal structure. The favorable fcc structure of the MgSc hydride most likely originates from the fact that the fcc structure of ScH_2 is retained, even when Sc is partially substituted by Mg: it was experimentally determined that the $Mg_{80}Sc_{20}$ composition yielded an optimum in hydrogen storage capacity, while exhibiting excellent rate capability (i.e., fcc-structured hydride). Unfortunately the high cost of Sc prevents its widespread use. A promising low cost substitute, with properties that can resemble those of Sc, is Ti. However it doesn't form intermetallics with Mg under standard alloying conditions because these 2 elements are considered as immiscible, being their enthalpy of mixing positive ($\Delta H_{mix} >$ 30kJ/g atom) and being no stable bulk compounds present in the binary phase diagram (figure 5.1). Alloying is however possible by means of mechanical alloying of bulk samples, physical vapour deposition, e-beam deposition and sputtering. For example Kyoi et al.[56] were successfull in synthesizing metastable Mg_7TiH_x powders by using quite high pressures (8 GPa) at 873 K in an anvil cell; however after hydrogen release this ternary hydride decomposed in Mg and Titanium hydride and no Mg-Ti binary compound was left. Remarkably, Vermeulen et al.[57] achieved hydride formation at low temperatures and stability upon cycling for Mg-Ti thin film systems, in which Mg and Ti resulted highly mixed.

Mg-Ti-H system shows also interesting optical properties: while the film is metallic in the as-deposited state (high reflectance and low transmittance) it becomes highly absorbing upon hydrogen uptake; Van Setten el al.[106] claim that the optical absorption is due to the high degree of mixing between Mg and Ti, via a lowering of plasma frequency. It is reported that $Mg_{0.80}Ti_{0.20}H_{1.7}$ thin films combine a high optical absorption (87% of the solar spectrum) with a low thermal emissivity (10%), while after desorption they absorb no more than 1/3 of the solar spectrum; moreover their great advantage is switchability [107, 108].

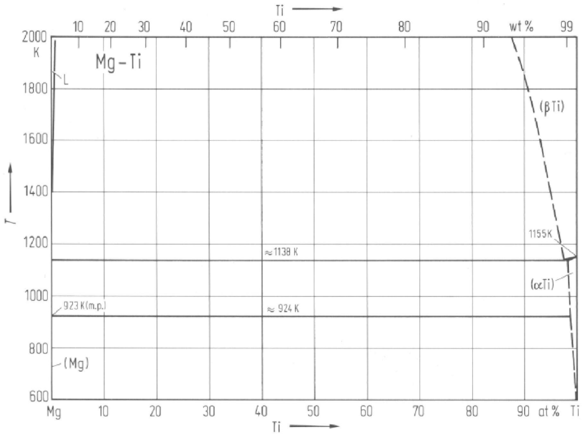

Figure 5.1: Bulk Mg-Ti phase diagram [109].

5.2 Experimental

Ti doped-Mg thin films, with a Ti buffer layer, were deposited on Si and glass substrates by r.f. magnetron sputtering. Depositions were done in a custom built r.f. magnetron sputtering system (13.56 MHz) equipped with 3 independent 2" sources and a r.f.–biased sample holder. The magnetron sputtering sources were positioned at a $\approx 30°$ inclination to the substrate normal and a target-to-substrate (center to center) distance of 12 cm. The sample holder, on the ceiling of the vacuum chamber, was rotated at 5 r.p.m. in order to assure a deposition uniformity better than 5%. Titanium, magnesium and palladium layers were deposited, in sequence, onto silicon wafers and fused silica slabs. The natural oxide on the Si wafers was removed by dipping in concentrate HF. These samples were then rinsed in deionized water and stored in isopropanol. Silica slabs were washed with a detergent, rinsed with deionized water and ultrasonically cleaned in trichloroethylene, acetone and isopropanol. Once in the sputtering chamber, the substrates were sputter-cleaned at a power of 20 W for 20 min in order to remove any residual surface contamination (in these conditions we measured a 10nm-thick sputtered layer for silica). The Ti layer was sputtered at first onto the cleaned substrates in order to assure a good adhesion of the Mg layer. Targets materials were 2” diameter Ti (99.9%), Mg (99.95%) and Pd (99.99%) disks. Sputtering was performed in pure Ar (99.9995%) at a pressure of $4 \cdot 10^{-3}$ mbar. The base pressure was better than 10^{-6} mbar. Before starting the depositions, sources were conditioned for 15 min. at the operating conditions. Depositions were performed at room temperature. Powers delivered to the sputtering sources were 30 W, 20 W and 10 W for Ti (buffer layer), Mg and Pd, respectively. Sputtering times were 160 s, 3300 s and 1050 s for Ti, Mg and Pd, respectively. For Ti co-sputtering with Mg the delivered power was 15 W, 22 W and 30 W for the low, medium and high concentration samples, respectively. The elemental composition of the films was measured by Rutherford Backscattering Spectroscopy (RBS) using a 2 MeV $^4He^+$ beam at Laboratori Nazionali INFN of Legnaro (Padova). The structural characterization of the films was carried out by Grazing Incidence X–Ray Diffraction (GIXRD) (with typical incidence angle θ=0.8°) in parallel beam geometry with a Panalytical X’Pert Pro MRD diffractometer equipped with a parabolic mirror in front of a CuK_α X–ray source. Hydrogen absorption was attained in a pre-evacuated (P=$4.5 \cdot 10^{-5}$ mbar) stainless steel chamber filled with hydrogen (purity: 99.999%). For in-situ desorption measurements a heatable specimen holder (Anton Paar DHS 900 hot stage) has been used in the GIXRD apparatus. Diffraction patterns were acquired with integration time set to 15 s, the step size to 0.05° and the incidence angle to 0.8°. Optical transmission spectra were recorded with a JASCO V-600 spectrophotometer in the 900-200 nm wavelength range.

5.3 Structural properties

RBS measurements on the different samples are reported in figure 5.2 and elemental amounts, estimated by simulating experimental spectra, in table 5.1: the only striking difference is the Ti concentration in the Mg layer. The GIXRD pattern of the Mg-Ti thin films with lower Ti concentration is reported in figure 5.3; the fcc-Pd is polycrystalline with the (111) reflection at $2\theta = 40.206(3)$ as the most intense one and lattice parameter a=3.877(1) Å. By using Scherrer formula a crystallite size of 8 nm is estimated. The Mg is

Elemental amounts [10^{15} at/cm^2]				
Sample	Pd	Mg	Ti	Ti-buffer
Mg	98	820	–	10
low	100	880	57.2	10
medium	100	880	114.4	10
high	98	900	189	10

Table 5.1: Results from simulation of RBS experimental spectra. Reference data of a sample with only Mg is also reported.

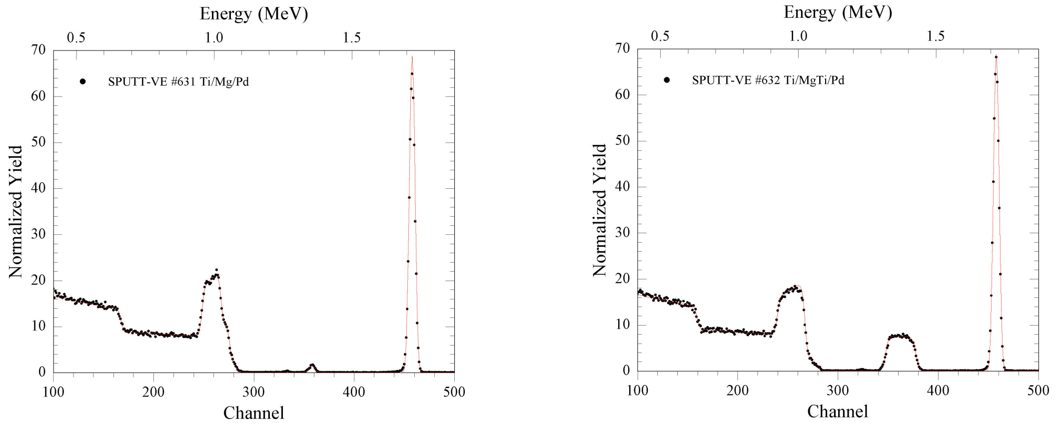

Figure 5.2: RBS spectra of the sample with only Mg (left) and of that with the highest Ti concentration (right). The other two are similar to the latter. From higher to lower channels: Pd, Ti, Si and Mg peaks.

textured, with the strongest reflection at 63.809(1) lying between hcp-Mg (103) and hcp-Ti (103), so that it is indexed as Mg-Ti (103). Crystallite size is about 27 nm. No reflections belonging to Mg or Ti are present. The diffractograms of the other two concentrations resemble the first one, except for the hcp Mg-Ti (103) reflection's position, which shifts to higher angles with Ti increase: this is a clear evidence of partial substitution of Mg by Ti, which in fact has a smaller molar volume than Mg, causing the lattice to contract. Mg-Ti (103) reflections are reported in figure 5.4. On the other hand, $\theta - 2\theta$ scans for the three types of films evidenced that the only Mg-Ti reflections are the (002) and the smaller (004) whose position is function of Ti concentration; regarding Pd, it is found to have only the Pd (111) reflection oriented perpendicular to the substrate for the medium and high concentration samples, while no reflections were found for the low one. The lack of preferential orientation along the substrate normal seems to be peculiar to Mg-rich surfaces: in fact previously synthesized Pd capped Mg thin films don't show Pd reflections parallel to the substrate normal. These findings are in accordance with literature [110]. According to Vegard's law, a linear relationship exists between the crystal lattice constant and the composition [111]. Figure 5.5 shows the evolution of the d-spacing of $Mg_{1-y}Ti_y$ (103) reflection with respect to the composition determined through RBS measurements; Ti concentration values calculated by applying Vegard's law are also reported. Table 5.2 summarizes structural data of the as deposited samples.

It is apparent that extracted values over-estimate Ti concentration: this behaviour can be explained with the argument that Vegard's law holds only in binary compounds where both elements have a comparable molar volume, which is not the case of Mg and Ti, being their molar volume 14 and 10.64 cm^3/mol, respectively.

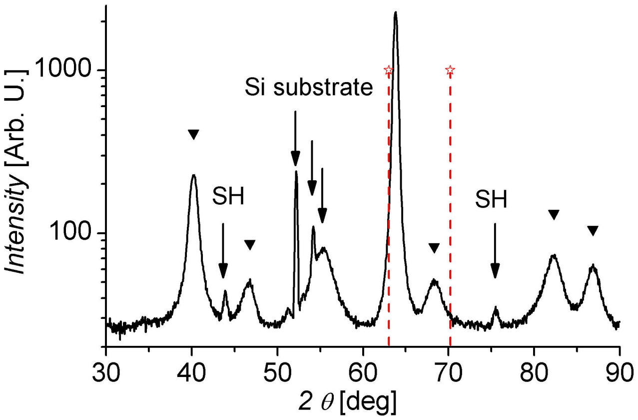

Figure 5.3: XRD pattern of the as deposited $Mg_{0.935}Ti_{0.065}$ film on silicon. ▼: Pd; SH: reflection from the sample holder. The two dotted vertical lines evidence the position of Mg (103) and Ti (103) reflections, respectively.

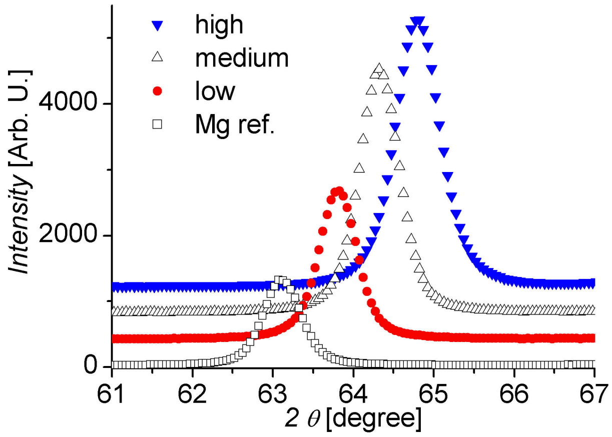

Figure 5.4: Position of reflection indexed as Mg-Ti (103) as a function of Ti concentration (c_{Ti}) in Mg. □: $c_{Ti} = 0$; •: $c_{Ti} = 6.5\%$; △: $c_{Ti} = 13\%$; ▼: $c_{Ti} = 21\%$. Patterns are shifted in intensity for clarity.

Sample	2θ[°]	d-spacing [Å]	size [nm] (Scherrer)	y of $Mg_{1-y}Ti_y$ (RBS)	y of $Mg_{1-y}Ti_y$ (Vegard's)
Mg	63.120	1.472(1)	28	–	–
low	63.809	1.457(1)	27	0.065	0.11
medium	64.326	1.447(1)	24	0.13	0.19
high	64.803	1.437(1)	19	0.21	0.26

Table 5.2: Structural data for samples at 3 different Ti concentration. Reference data of a sample with only Mg is also reported.

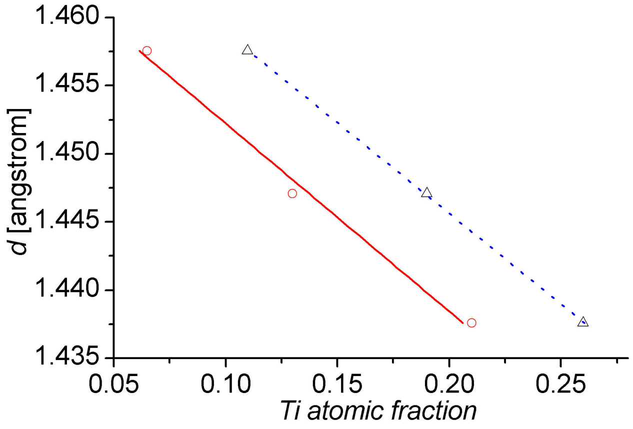

Figure 5.5: Comparison of d interplanar distance dependence on c_{Ti} between RBS values and estimations given by Vegard's law. △: Vegard's Law; ∘: RBS measurements.

5.4 Hydrogen loading and desorption

Hydrogen loading was attained by inserting as deposited samples in a pre-evacuated ($P = 4.5 \cdot 10^{-5}$ mbar) stainless steel chamber filled with hydrogen at 0.5 bar and then heated at 60°C for 3.5 hours; loading parameters were chosen at purpose lower than those for the Pd-capped Mg thin films previously studied, in order to have a first indication of expected better absorption properties of these films.

5.4.1 Low-Ti concentration sample

The X-ray diffractogram for the $Mg_{0.935}Ti_{0.065}$ after hydrogen absorption is reported in figure 5.6; the intensity of the (103) reflection decreases and moves to lower angles, while two weak reflections belonging to a hydride phase appear around 26.4° and 28°, the latter being the MgH_2 (110), at a higher angle with respect to the pure phase, due to the presence of Ti. The Pd (111), convoluted with MgH_2 (200) shifts to 40.368(2)°. The hydrogenation results thus partial: by peak intensity integration we estimate that a 70% of Mg-Ti has transformed to hydride, maybe partly amorphous, considering the small MgH_2 reflections present. Successively, *in-situ* hydrogen desorption measurements were performed at 90°C under N_2 flux (60 cm^3/min) with a heatable sample holder by continuously acquiring several XRD scans of the Mg-Ti (103) reflection, as already done before. The choice of N_2 was dictated by the need of having slower kinetics than in air and the chance of a first comparison with the preceeding samples: in fact, it must be recalled that the Pd capped-Mg (old) thin films considered in the previous chapter didn't show any appreciable hydrogen release with these desorption settings even in 24 h.

During desorption the Mg-Ti (103) grows and moves back towards the initial value, following the path shown in figure 5.7, where a plateau-like region can be distinguished.

Interestingly, after exposure to air at RT an additional shift in 2θ to a final value of 63.842(1) occured. The final FWHM is higher than the initial one: this could be a hint of non-uniform strain. The particular behaviour of (103) reflection recalls that found by Vermeulen et al.[112] for $Mg_{90}Ti_{10}$ thin films, where the constant interplanar distance of the plateau region is ascribed to a coexistence with a varying relative fractions of a hydrogen-rich and a hydrogen-poor phases with constant composition. No other Mg-Ti reflections are visible after complete desorption, which shows the structural reversibility and absence of phase segregation, according to literature for these systems [110, 112].
On the other hand the partial hydrogenation could be responsible for this type of behaviour too, so a full loading was then attempted by raising hydrogen pressure to 1 bar and time to 4 hours. With these settings the Mg-Ti (103) disappeared and several reflections of α-MgH_2 grew as shown in figure 5.8a. The most intense hydride reflection is the (110) at 27.92(1) with a crystallite size of about 10 nm; it also presents a shoulder at lower 2θ values, which is not identifiable. Desorption was then performed in air at 50°C: it must be pointed out that these samples seem to release hydrogen already at room temperature, so introducing uncertainties in kinetic results, especially due to: i) trade-off between time resolution and counting statistics and ii) reduced crystallinity, which requires longer acquisition time, in comparison with the previously synnthesized sample. Anyway, it was possible to follow desorption kinetics (figure 5.9) and (103) peak's position with time (figure 5.10). After desorption in air the degree of initial texture along (103) is greatly reduced and other reflections are present, which, by fitting, result compatible with an hcp Mg-Ti structure with lattice parameters: $a = b = 3.193(2)$; $c = 5.162(2)$. Applying Vegard's law, it comes out that the Ti concentration is $c_{Ti} = 7.2\%$, which is less than the previous estimation and nearer the value found by RBS. Mg-Ti crystallite sizes ranges between 20 to 30 nm; Mg-Ti (103) is now 21% in intensity with respect to the as deposited one, while its interplanar distance d is higher, suggesting an expanded structure due to an irreversible amount of hydrogen still present in the host lattice. Finally Pd lattice parameter is $a = 3.858(1)$, which is slightly less then the initial value, suggesting that a relaxation of the deposition-native strain has occured. After 6 absorption/desorption cycles, diffraction patterns result similar to the initial one, indicating that Mg or Ti phase has not segregated; crystallinity, however, seems to have been reduced and the fraction of hydrogen irreversibly bound in the lattice has increased.

5.4.2 Medium-Ti concentration sample

The sample with $c_{Ti} = 13\%$ was subjected to the same hydrogen-loading procedure as the low concentration one. In this case absorption has been more effective, as shown in figure 5.11: in fact, although Mg-Ti (103) is still present, its intensity has decreased to 10% of the initial one. At the same time broad relections related to a hydrogenated phase have appeared: those at $2\theta = 26.28(1)°$ and $32.61(2)°$ are close to the (220) and (222) reflections, respectively, found by Kyoi et al.[56] for the fcc (Ca_7Ge type, a=9.532 Å)-Mg_7TiH_x; this structure was argued to be similar with that of fcc $TiH_{1.9}$, but with

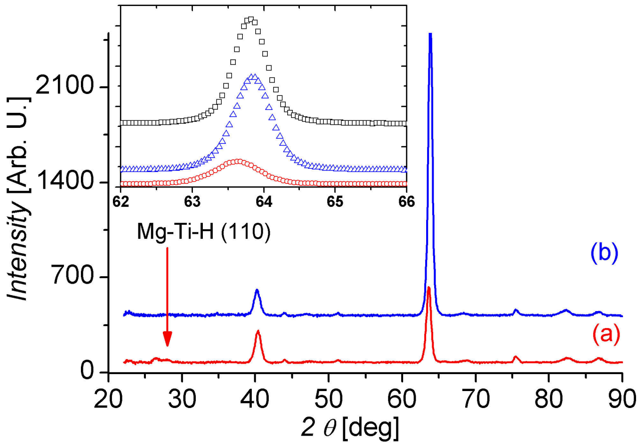

Figure 5.6: XRD patterns of low Ti concentration sample after partial hydrogen absorption at T=60°C, P=0.5 bar for 3.5 h (a) and desorption in N_2 flux at 90°C for 24 h (b). Inset: Mg-Ti (103) for the as deposited (□), partially loaded (○) and desorbed (△) sample. Patterns are shifted in intensity for clarity.

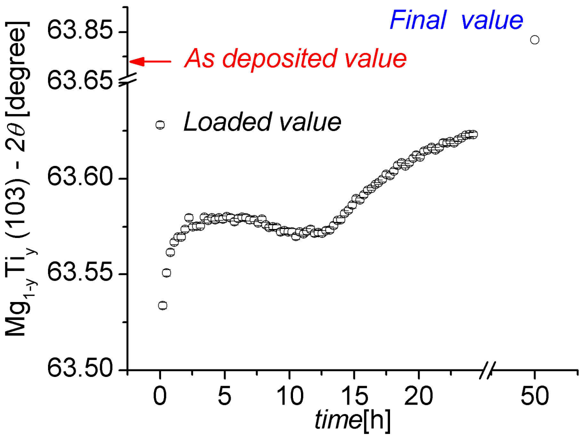

Figure 5.7: Low Ti concentration sample. Mg-Ti (103) position's evolution during desorption in N_2 at 90°C.

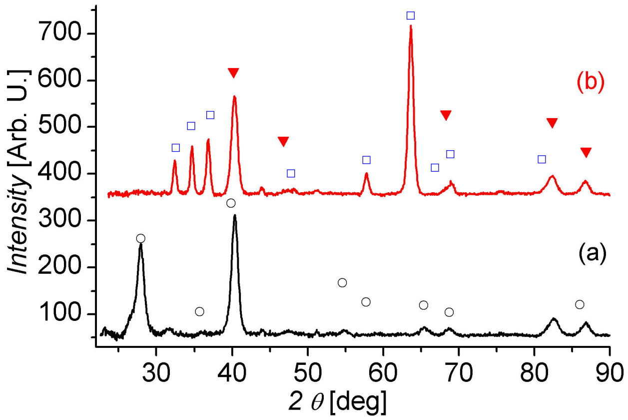

Figure 5.8: XRD patterns of low Ti-concentration sample after full hydrogen absorption at T=60°C, P=1 bar for 4 h (a) and desorption in N_2 flux at 90°C for 24 h (b). After desorption the degree of initial texture is greatly reduced. □: Mg-Ti; ○: Ti-doped α-MgH_2; △: Pd. Patterns are shifted in intensity for clarity.

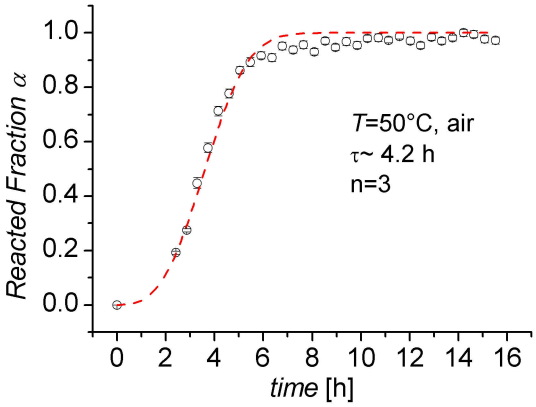

Figure 5.9: Desorption kinetics in air at 50°C after full loading; n and k values given by fitting are also reported.

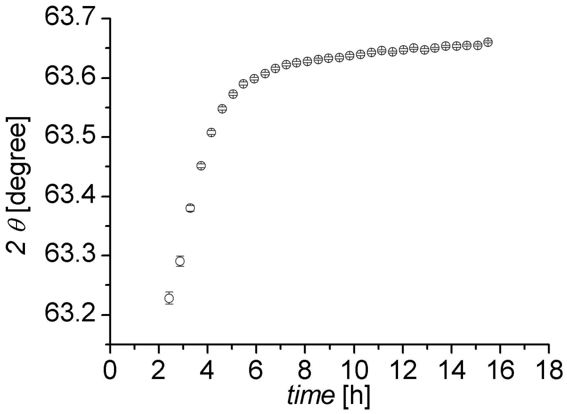

Figure 5.10: Mg-Ti (103) position's evolution during desorption in air at 50°C.

most of Ti atoms substituted by Mg in an ordered way, resulting in a superstructure with a doubled unit cell. Moreover no hydride peaks belonging to the MgH_2 tetragonal phase seem to be present, except for the slightly increase in intensity the Pd (200) reflection, which could be caused by convolution with α-MgH_2 (200). In figure 5.12 Mg-Ti(103) position evolution during desorption in N_2 flux at 90°C is reported: it is similar to the low concentration sample, but the kinetics results slower. After 24 h the hydride phase is still present and the Mg-Ti (103) intensity is 22% of the as deposited one.

5.4.3 High-Ti concentration sample

Upon hydrogen loading at 60°C, 0.5 bar for 3.5 h, the Mg-Ti (103) reflection of the high-Ti sample completely disappeared, as shown in figure 5.13. It is apparent that a broad hydride reflection has grown at $2\theta = 32.185(6)$, with a smaller one on its right side. This reflection is close to the (222) reflection of fcc-Mg_7TiH_x: assuming a fcc simmetry, the cell parameter a would be about 9.634(2) Å. Reflection at $2\theta = 34.55(2)$ is near a Mg-Ti(002) reflection, but, applying Vegard's law with the known Ti concentration, it doesn't match with it. We will call it as the "unknown" reflection. More about it can be suggested by continuous diffraction scans during desorption (N_2, 90°C) in the angular range comprising $Mg_{1-y}Ti_yH_x$ (222). Figure 5.14 shows the evolution of hydride fcc (222) and unknown reflections: the former decreases, while the latter grows. Both then move to higher angular values, but the latter is slower than the former (figure 5.15). This behaviour can be due to the phase transition from a fcc to a hcp structure, where the former is represented by the fcc (222) and the latter by the unknown reflection: first the lattice of the fcc phase contracts, then the two phases coexist and finally only the expanded hcp evolves, moving towards the initial position. It is interesting to note that the unknown reflection reaches its maximum in intensity in the region around $2\theta = 34.70$ and then slowly decreases. While the coexistence is in accordance with literature [110, 112], the following decrease of hcp reflection is not reported. On the other hand, no Mg-Ti (103) growth was detected during this process. The annealing in N_2 was not enough to desorb all the hydrogen, so exposure to air was performed to speed up the process. Interestingly, after the additional desorption, the unknown reflection results almost disappeared and the Mg-Ti (103) starts growing, which suggests that the final step of dehydrogenation is connected to re-orientation of Mg-Ti domains along the starting preferential direction.

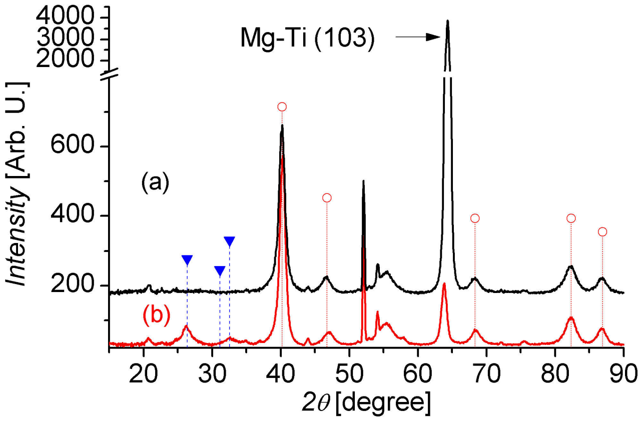

Figure 5.11: XRD patterns of medium Ti concentration sample (a) and after hydrogen absorption at T=60°C, P=0.5 bar for 3.5 h (b). The Mg-Ti (103) reflection has been reduced to 10 %. ○: Pd; ▼: $Mg_{1-y}Ti_yH_x$. Patterns are shifted in intensity for clarity.

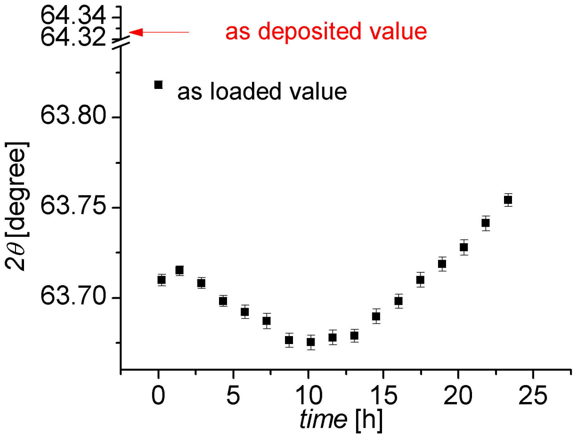

Figure 5.12: Medium Ti concentration sample. Mg-Ti (103) position's evolution during desorption in N_2 at 90°C.

The pattern after full desorption is reported in figure 5.16. The most interesting features are: i) the reduced intensity –about 11% of the starting value– of Mg-Ti (103), wich is shifted to $2\theta = 64.836(3)°$; ii) the appearance of a reflection at $2\theta = 58.723(3)°$, which, according to Vegard's law, can be indexed as Mg-Ti(110); iii) the broad zone just before the Pd (111), which could be a set of at least three reflections, maybe Mg-Ti (100), (002)

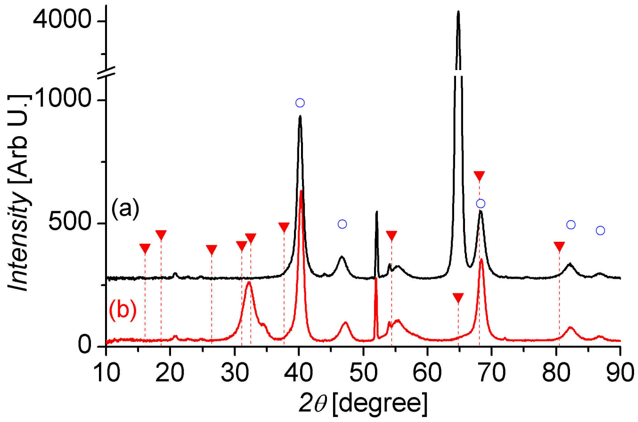

Figure 5.13: XRD patterns of high Ti-concentration sample in the as deposited state (a) and after full hydrogen absorption at T=60°C, P=0.5 bar for 3.5 h (b). The Mg-Ti (103) reflection has almost disappeared. ○: Pd; ▼: $Mg_{1-y}Ti_yH_x$. Patterns are shifted in intensity for clarity.

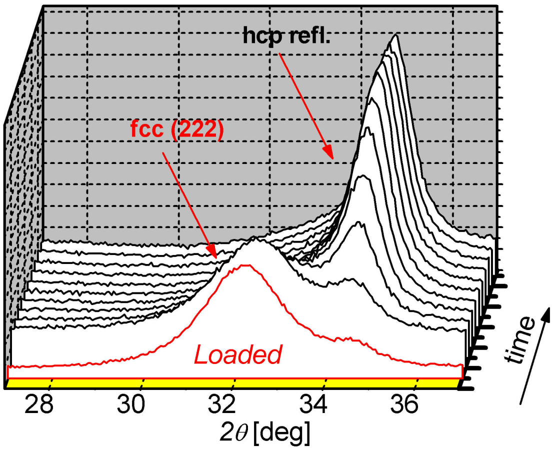

Figure 5.14: Evolution during desorption of fcc (222) and hcp reflections for the high-Ti concentration sample.

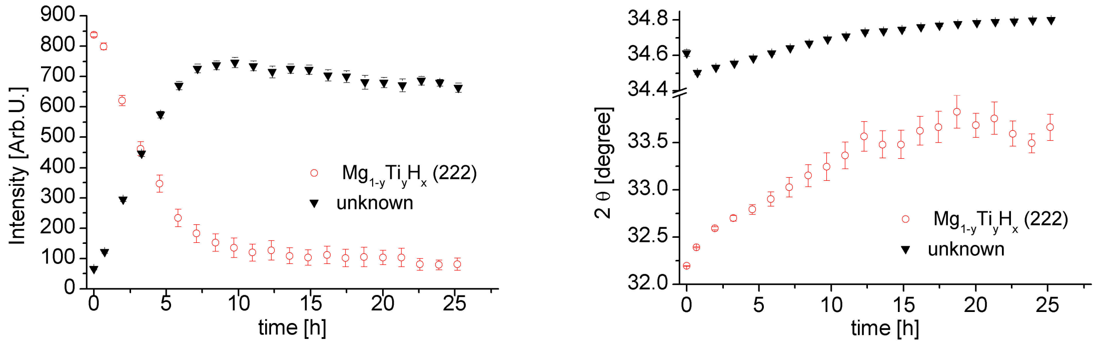

Figure 5.15: Evolution of peak intensity (left) and position (right) during desorption for the high-Ti concentration sample. ○: fcc (222); ▼: hcp reflection.

and (101). In order to see if cycling could induce growth of other reflections belonging to the fcc hydride phase or the hcp metal one, another loading at 1 bar was performed. As shown by figure 5.17, the reflection at $2\theta = 34.55(2)°$, present in the previuos loading, is not visible, indicating that transition from fcc to hcp phase has not started yet. No additional reflections belonging to the hydride phases seem to be present.

For comparison a sample with only Mg was hydrogen-loaded at 1 bar, 60°C for 4 h; in this case the loading results partial, as depicted in figure 5.18b. Mg (103) is reduced to 65% of the initial intensity value and it is shifted to a slightly higher 2θ value: from 63.119(1)° to 63.132(1)°, indicating the presence of a compressive stress. Reflections belonging to α-MgH_2 are recognized at 27.967(2)°, (110), 35.82(1), (101) and 40.427(2)°, (200) in convolution with Pd (111); instead, the one at $2\theta = 31.49(1)$ could be ascribed to γ-MgH_2. After desorption, attained in air at 90°C in 10 min., the Mg re-grows mostly textured along (103) direction, whose corresponding diffraction peak has moved to 63.233(1)° and grown in intensity to 113% of the as deposited value; this increase can be ascribed to a hydrogen-induced crystallite re-orientation, which is supported also by the appearance of weak hcp-Mg (100), (002) and (101) diffraction peaks (figure 5.18).

5.5 Discussion

The formation of a Mg-Ti random alloy, suggested by the presence of only one diffraction peak in the as deposited sample, is unlikely, considering the large positive enthalpy of mixing of the metal constituents [113]. Instead it is argued that a coherently coupled mixture of Mg and Ti is formed [114], which, after hydrogen absorption and desorption, retains its structure and crystallinity without phase segregation: this is considered a surprising result, since hydrogen cycling in other Mg-based systems is generally affected by large scale phase segregation. As shown above, the hydride phase has a different structure depending on Ti concentration: rutile for low concentration and fluorite for the higher ones. It is reported that rutile structure is found only for Mg-rich composition ($y < 0.13$ in $Mg_{1-y}Ti_y$) [110], while for $y > 0.13$ data point to a structure with cubic symmetry and a lattice

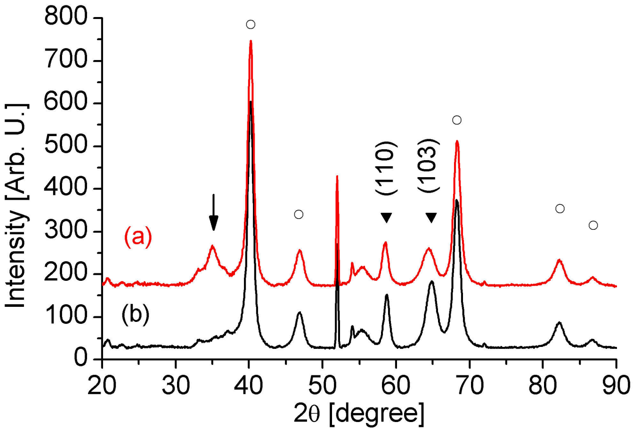

Figure 5.16: Sample with high Ti concentration. Xrd diffraction pattern after partial desorption in N_2 at 90°C (a) and after full desorption in air (b). ○: Pd. Patterns are shifted in intensity for clarity.

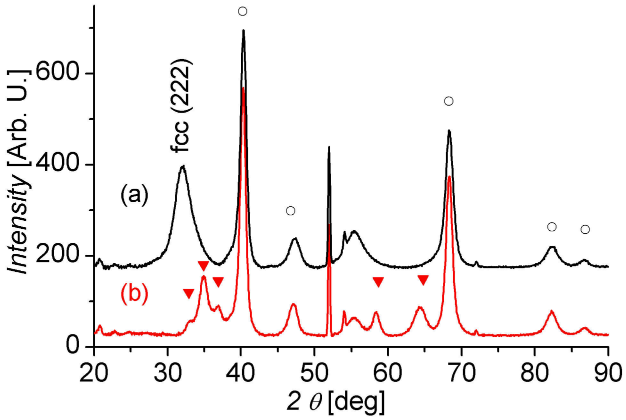

Figure 5.17: Diffractograms after full hydrogen absorption at 1 bar, 60°C, 4h (a) and after partial desorption in air (b). ○: Pd; ▼: hcp Mg-Ti. Patterns are shifted in intensity for clarity.

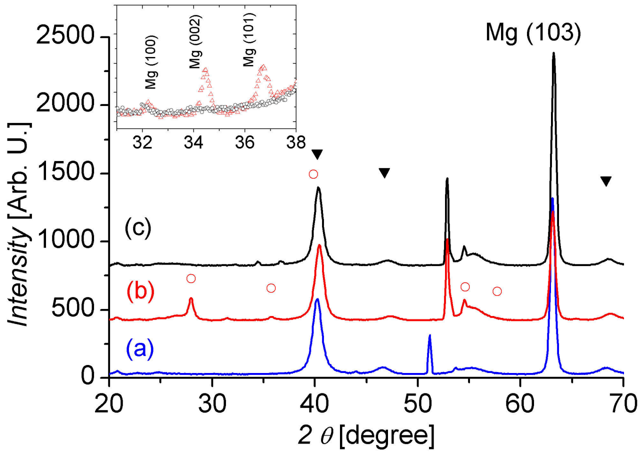

Figure 5.18: Diffractograms of $c_{Ti} = 0$ sample in the as deposited (a), partially hydrogen-loaded at 1 bar, 60°C, 4h (b) and desorbed (c) state. ○:α-MgH_2; ▼: Pd. Inset: weak Mg reflections grown after desorption. Patterns are shifted in intensity for clarity.

parameter which varies continuously with metal composition in the parent alloy. Baldi et al. [114], by combining XRD and EXAFS measurements, concluded that the material is a composite of Mg and Ti (in the metallic state) and MgH_2 and TiH_2 (in the hydrogenated state) regions that form a coherent crystalline structure, in which Hydrogen first occupies Ti-related sites, due to the more negative enthalpy of the corresponding hydride formation. Our results are consistent with this picture, considering the time evolution of Mg-Ti (103) during desorption. It is also claimed that the coherent mixture model in the fcc structure for the high Ti concentration samples can be understood by assuming that both TiH_2 and MgH_2 have a cubic structure. If this is expected for the former, it sounds strange for the latter, being its crystalline structure, at normal pressure and temperature, rutile. However Vajeeston et al.[33] found by synchrotron radiation measurements, supported by theoretical calculations, that a transition to a cubic phase (β) occurs at high pressure (around 4 GPa); moreover Density Functional Theory calculations by Pauw et al.[115] showed that the rutile MgH_2 structure in $Mg_{0.75}Ti_{0.25}H_2$ is destabilized by 16 $kJ\ mol^{-1}$ and that the fluorite structure becomes the most stable around $y = 0.20$. The formation of such a cubic structure at normal pressure and temperature could be caused by the local stress induced by Ti and TiH_2; the presence of stress is not surprising in thin films and the coexistence of α and γ magnesium hydride in Pd capped magnesium films is a clue for it.

The first conclusion that can be drawn about Ti-doping is its beneficial role for hydrogen absorption: in fact the more the Ti concentration is, the faster the hydride formation. Regarding desorption, an improvement in respect of previously studied Pd-capped Mg thin films has occured; however, this achievement can be also due in part to the improved Pd cap layer. Moreover the indicator we use for estimation of hydrogen absorption/desorption, the Mg-Ti(103), could not be suitable for kinetics measurements in these samples, taking into account that desorption already occurs in air at RT and that diffraction measurements are intrinsically affected by poor time resolution. All this calls for a faster and reliable method to monitor hydride formation/dissociation with time: on this purpose, the feasibility of optical transmittance measurements was studied.

5.6 Optical transmission measurements

Optical transmission measurements were performed for the three Ti concentrations samples and for that with nominal $c_{Ti} = 0$ deposited on glass. Again, the transition of Mg from a metal to a wide band gap semiconductor upon hydride formation is exploited. As shown by Borgschulte et al.[116] Lambert-Beer's law can be used to relate the optical transmission of a hydrogenated film to its hydrogen concentration; moreover Borsa et al.[110] confirmed, by joint electrochemical and optical measurements, that the logarithm of transmission increases linearly with hydrogen concentration. Surprisingly, it was found that this relation is valid also for metallic hydrides as PdH [117]. Energy gaps for the hydrogen loaded samples were estimated with the Tauc procedure, already illustrated in the previous chapter. Before optical measurements, $2\theta - \theta$ diffraction measurements were performed to have an estimation of the degree of hydrogen loading. This type of measurement was preferred to GIXRD because of its more intense diffracted signal, although only reflections coming from planes parallel to the substrate are detectable in this way.

The $c_{Ti} = 0$ sample was hydrogen-loaded at 1 bar, 80°C for 7h in order to reach a full loading: figure 5.19 shows the corresponding $2\theta - \theta$ diffraction scans, where hcp Mg (002) at $2\theta = 34.415(2)$ and α-MgH_2 (110) $2\theta = 27.922(2)$ are visible. Spectra after one and two successive loading are reported in figure 5.20; it is apparent that the second Hydrogen-loading has resulted into a higher transmission in respect of the first one. Given the fact that diffractograms are similar in both cases, either the difference is due to a higher fraction of PdH_x for the second or an amorphous fraction with insulating properties, which has not been hydrogenated previously, is present. Clearly, from $2\theta - \theta$ xrd measurements it's difficult to find an answer, being the Pd (111) absent in the patterns. On the other hand GIXRD evidenced the presence of PdH_x (111) peak after the 2^{nd} loading: by comparing literature value for Pd and PdH_x, the latter formed under a hydrogen pressure of 1 bar, and simulating optical transmittance spectra with IMD software [118], it comes out that is reasonable to ascribe transmittance increase to a higher palladium hydride content. However, it can't be excluded that the a small contribution arises from the hydrogenation of Ti buffer layer. Continuous scans in time of transmittance show that the sample releases hydrogen at room temperature in air, as it was suspected (figure 5.21). Energy gap, estimated after first and second loading is (5.62 ± 0.03) eV and (5.54 ± 0.09) eV, respectively, in accordance with literature.

Optical transmittance spectra of the sample with the lowest Ti concentration is reported in figure 5.22, where it is shown that transmittance increases after the second loading, probably for the same reason proposed above. Calculated energy gap is (5.41 ± 0.05) eV and (5.37 ± 0.03) eV after the first and second loading, respectively.

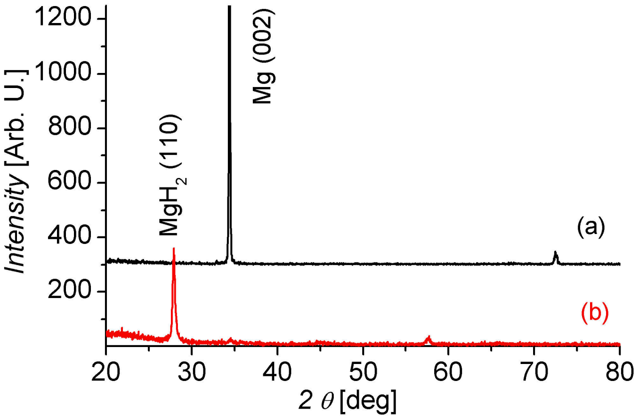

Figure 5.19: $2\theta - \theta$ scans of $c_{Ti} = 0$ sample in the as deposited (a) and hydrogen-loaded at 1 bar, 80°C, 7h (b) state. Patterns are shifted in intensity for clarity.

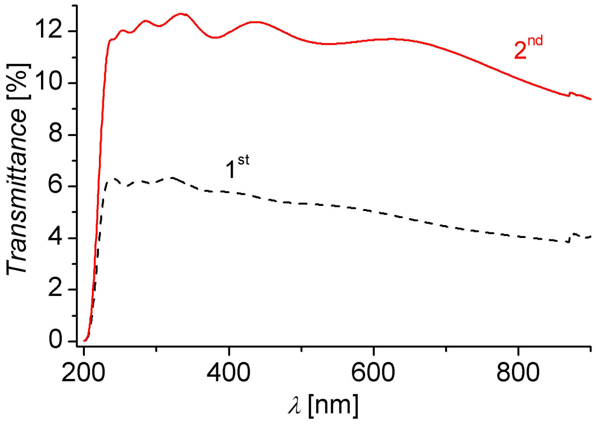

Figure 5.20: Optical transmittance spectra of $c_{Ti} = 0$ sample after one and two hydrogen-loading processes at 1 bar, 80°C, 7h.

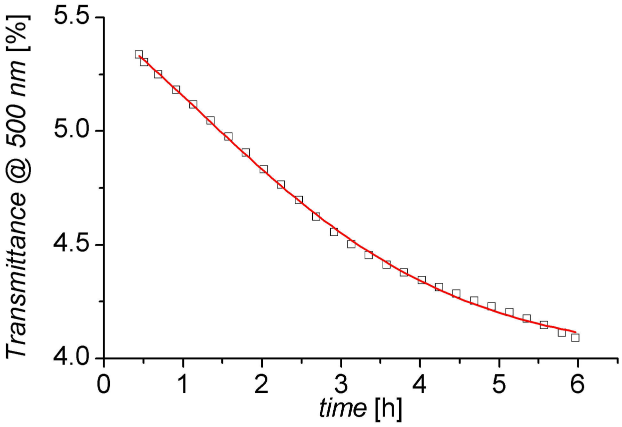

Figure 5.21: Decrease of transmittance with time during exposure to air at RT for the $c_{Ti} = 0$ sample after first hydrogen-loading.

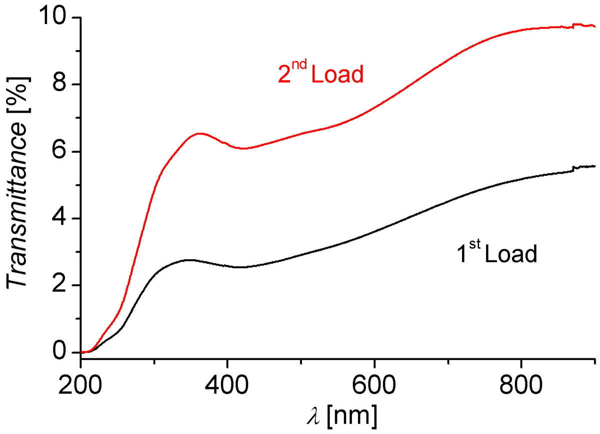

Figure 5.22: Optical transmittance of $c_{Ti} = 6.5\%$ sample after one and two hydrogen loading at 1 bar, 60°C for 4h.

High Ti concentration sample on glass was the loaded at 1 bar, 60°C for 4 h. In figure $2\theta - \theta$ diffraction patterns of the as deposited and loaded sample are reported: Mg (002) is at $2\theta = 35.353(1)$, according to Vegard's law, while α-MgH_2 (110) is not present. Instead a set of broad reflections are visible between 30° and 35°. Interestingly Pd (111), which is present in the as deposited state at $2\theta = 40.090(2)$, is shifted to lower angles (38.93(2)°), suggesting the formation of palladium hydride.

For this sample an attempt of crossed optical and diffraction measurements was done. Transmission spectra at different times are reported in figure 5.24: energy gap is estimated to be (4.09 ± 0.06) eV, which is lower than the MgH_2 one, due to the presence of metallic Titanium. In figure 5.25 we report the series of scans performed in $2\theta - \theta$ mode in the range $30 \div 42$: they show the same transition from the fcc to hcp structure as that seen for the sample on silicon in grazing incidence, except for the fact that now the final position for the hcp reflection is the Mg-Ti (002). It is also visible the progressive transformation of PdH_x in Pd. Comparison between desorption kinetics estimated by optical transmission signal at 500 nm with PdH_x and $Mg_{0.79}Ti_{0.21}H_x$ reflections evolution suggests that the decrease of transmission is correlated with them, especially with PdH_x; in fact most of transmission decrease occurs during hydrogen desorption from palladium hydride (figure 5.26). In addition, Pd peak evolution during desorption supports these findings: it stabilizes around $2\theta = 40.27$ when transmission approaches zero (figure 5.27). On the other hand Mg-Ti (002) has a slow evolution which is not correlated to optical transmittance (figure 5.28).

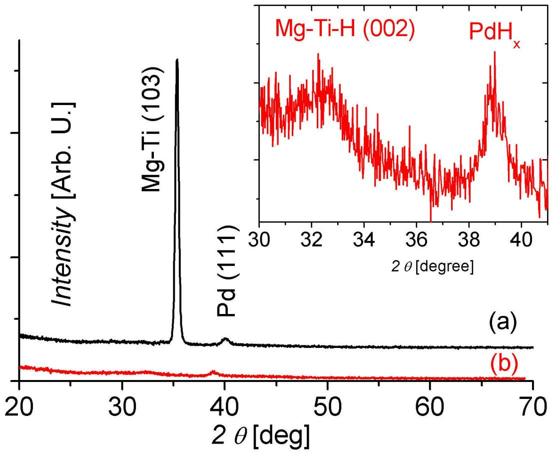

Figure 5.23: $2\theta - \theta$ scans of $c_{Ti} = 21\%$ sample in the as deposited (a) and hydrogen-loaded at 1 bar, 60°C, 4h (b) state. Inset: zoom of (b), showing fcc hydride and palladium hydride reflections. Patterns are shifted in intensity for clarity.

Correlation of diffraction measurements with optical ones seem not to be straightforward for the Mg-Ti system: the transition from a fcc to a hcp structure during desorption poses problems in estimating kinetics of hydrogen desorption by monitoring reflections belonging to the hydride phase or to the metal phase. Anyway, optical measurements are

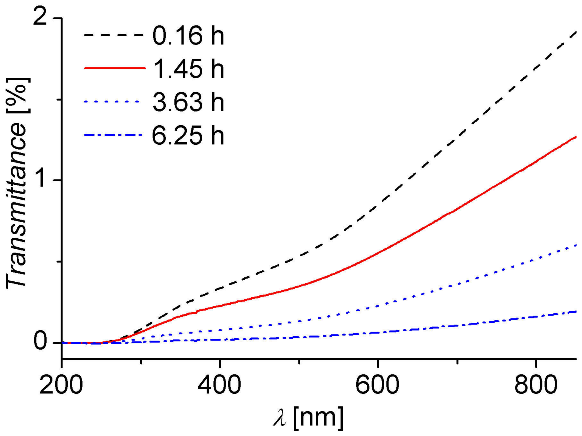

Figure 5.24: Optical transmittance during desorption in air at room temperature. The initial value is quite small due to the presence of metallic Ti.

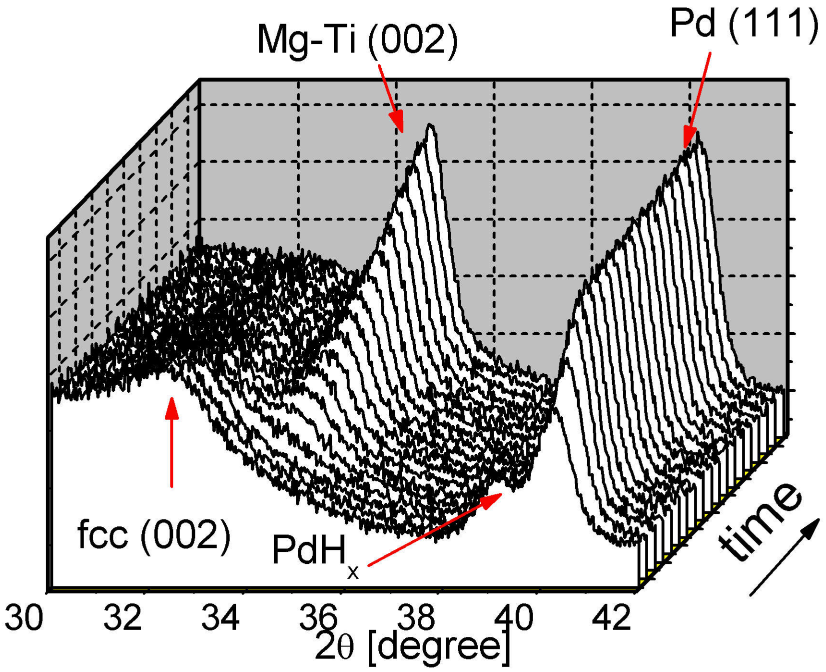

Figure 5.25: $2\theta-\theta$ scans of $c_{Ti} = 21\%$ sample during desorption in air at room temperature.

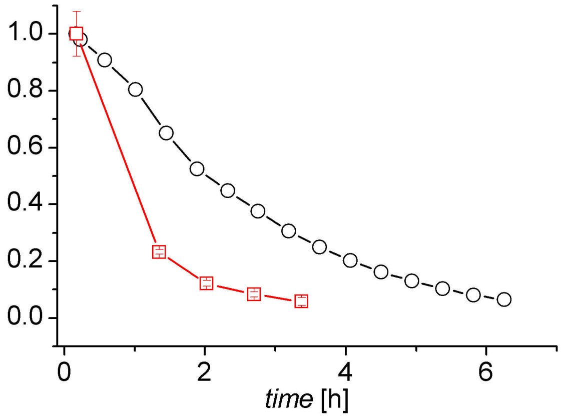

Figure 5.26: Comparison between decrease of optical transmittance signal and PdH_x intensity. Both signals are normalized to their maximum. ○: transmittance; □: PdH_x intensity.

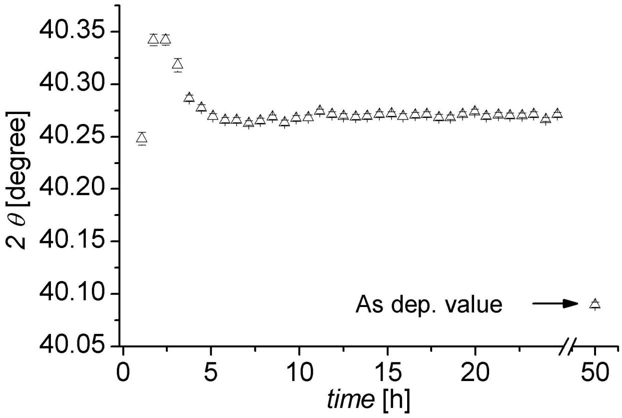

Figure 5.27: Evolution of Pd (111) peak during desorption in air at room temperature.

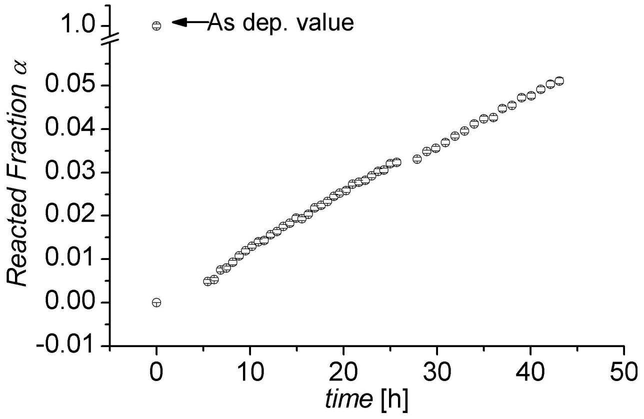

Figure 5.28: Evolution of Mg-Ti (002) intensity during desorption in air at room temperature. It is apparent that time for the process is quite different from that of optical transmittance decrease.

more suitable than diffraction ones to estimate relative desorption kinetics of the samples under study, without the need of knowing the amount of hydrogen in them. Assuming that $\ln T$ grows linearly with hydrogen concentration (5.1) we compare the time decrease of optical transmission of samples with $c_{Ti} = 0, 6.5, 21\%$ in figure 5.29. In all cases the decrease of transmittance is compatible with a homogeneous nucleation and growth of the metal phase within the whole volume of the sample, as observed for Mg-MgH_2 thin films. The faster desorption is that belonging to the high Ti concentration sample, while those of the low concentration ones are quite similar: this behaviour can be explained by the fact that Mg-Ti with low c_{Ti} transforms to a hydride with rutile structure, while with high c_{Ti} it assumes the fcc structure, which is known to have superior hydrogen transport properties.

$$\ln \frac{T}{T_0} \propto C_H \tag{5.1}$$

5.7 Conclusions

The fascinating properties of Ti-doping of magnesium have been studied: the high degree of mixing achieved by non-equilibrium synthesis (sputtering) for these two otherwise immiscible elements involves for $c_{Ti} > 13\%$ a crystalline structure modification of the hydride phase from rutile to fcc one, which enhances hydrogen transport properties and thus absorption/desorption kinetics. The transition from a cubic to hexagonal structure has been monitored by continuous X-ray diffraction measurements during desorption; moreover, grazing incidence mode has evidenced that the original texture present in all samples tends to decrease after hydrogen release, due to a re-orientation of crystallites. Estimations of desorption kinetics have been performed by means of optical transmittance measurements, by exploiting the linear dependence on hydrogen content of the logarithm

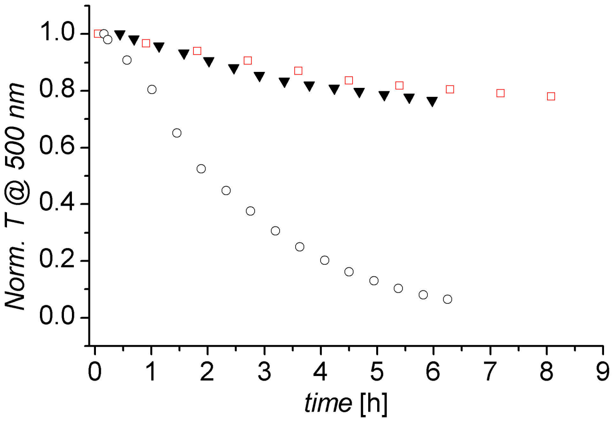

Figure 5.29: Decrease of optical transmittance at 500 nm for the samples with zero (▼), low (☐) and high (○) Ti concentration.

of transmittance. Energy gaps of the hydrogenated films have been found to decrease with Ti content in Mg, according to the metallic character of Ti and its hydride (TiH_2, $TiH_{1.9}$). Moreover, the switching optical properties of the film, combined with the tailoring of Ti concentration, can be exploited in smart coatings. Further developments of optical transmittance measurements can be attained by controlling temperature and atmosphere to which films are exposed, hence the possibility of continuously monitoring hydrogen absorption process follows.

List of Tables

List of Figures

Bibliography

[1] IPCC, Climate change 2007: Synthesis report (2007).

[2] BP, Bp statistical review of world energy (June 2008).

[3] I. E. Agency, World energy outlook 2006 (2006).

[4] R. Smalley, MRS Bulletin 30 (2005) 412–417.

[5] I. E. Agency, Key world energy statistics (2007).

[6] C. Campbell, Scientific American 278 (3) (1998) 77–83.

[7] M. Savinar, http://www.lifeaftertheoilcrash.net, visited in August 2008.

[8] D. Jones, Proceedings of the IEE: Science, Measurement and Technology 138 (1) (1991) 1–10.

[9] IAEA, http://www.iaea.org/newscenter/news/2008/uraniumreport.html, 3 June 2008.

[10] Q. Schiermeier, Nature 454 (2008) 816–823.

[11] R. Nakata, N. Hashimoto, K. Kawano, Japan. J. Appl. Phys. 35 (1996) L90.

[12] DoE, http://www1.eere.energy.gov, 9 September 2008.

[13] A. Zuettel, Naturwissenschaften 91 (2004) 157–172.

[14] S. Thomas, M. Zalbowitz, Fuel cells-green power, los Alamos National Laboratory.

[15] M. Winter, R. Brodd, Chemical Reviews 104 (2004) 4245–4269.

[16] P. Kruger, International Journal of Hydrogen Energy 33 (2008) 5881–5886.

[17] S. Tsang, Catalysis Today 23 (1995) 3–15.

[18] DoE, http://fossil.energy.gov, 28 October 2008.

[19] V. Aroutiounian, V. Arakelyan, G. Shahnazaryan, Solar Energy 78 (2005) 581–592.

[20] DoE, Hydrogen, fuel cells and infrastructure technologies program, http://www1.eere.energy.gov/hydrogenandfuelcells/mypp/pdfs/storage.pdf.

[21] G. Chen, S. Anghaie, http://www.inspi.ufl.edu/data/hproppackage.html, nASA/NIST databases.

[22] A. Zuettel, P. Sudan, P. Mauron, T. Kyiobaiashi, C. Emmenegger, L. Schlapbach, Int. J. Hyd. Energy 27 (2002) 203–212.

[23] H. Langmi, et al., J. All Comp. 356/357 (2003) 710–715.

[24] G. Sandrock, J. All. Compd. 293/295 (1999) 877–888.

[25] G. Pearson, Chem. Rev. 85 (1985) 41–49.

[26] L. Schlapbach, Surface properties and activation. In Hydrogen in intermetallic compounds II, Topics in applied physics 67, Springer, 1992.

[27] Fukai, Z. Phys. Chem. 164 (1989) 165–174.

[28] F. Schueth, B. Bogdanovic, M. Felderhoff, Chem. Comm. (2004) 2249–2258.

[29] B. Bogdanovic, M. Schwickardi, J. All. Comp. 253/254 (1997) 1–9.

[30] A. Zuettel, P. Wenger, S. Rensch, P. Sudan, P. Mauron, C. Emmenegger, J. Power Sources 5194 (2003) 1–7.

[31] P. Sudan, A. Zuettel, P. Wenger, P. Mauron, Nat. Mat. 85 (2004) 41–49.

[32] B. Sakintuna, F. Lamari-Darkrim, M. Hirscher, Int. J. Hydrogen Energy 32 (2007) 1121–1140.

[33] P. Vajeeston, P. Ravindran, B. C. Hauback, H. Fjellvåg, A. Kjekshus, S. Furuseth, M. Hanfland, Phys. Rev. B 73 (224102).

[34] A. Zaluska, L. Zaluski, J. Strom-Olsen, J. All. Compds 288 (1999) 217–225.

[35] J. Norskov, A. Houmueller, P. Johasson, A. S. Pedersen, J. Less Comm. Met. 46 (1981) 257.

[36] A. Krozer, B. Kasemo, J. Phys. Cond. Matter 1 (1989) 1533.

[37] H. Gleiter, Acta Mater. 48 (2000) 1–29.

[38] A. Pundt, Adv. Eng. Mater. 6 (2004) 11–21.

[39] R. Kirchheim, Phys. Scripta T94 (2001) 58–67.

[40] Mater. Trans. JIM 40 (M. Iwamoto and Y. Fukai) 606–611.

[41] P. Nordlander, J. Nørskov, F. Besenbacher, S. Myers, Phys. Rev. B. 40 (1989) 1990–1992.

[42] O. Gutfleisch, N. Schlorke-deBoer, A. Pratt, J. S. A. Walton, I. Harris, A. Zuettel, J. All. Compd. 357 (2003) 598–602.

[43] E. Ivanov, I. Konstanchuk, A. Stepanov, V. Boldyrev, J. Less-Common Met. 131 (1987) 25.

[44] K. Gross, D. Chartouni, E. Leroy, A. Zuettel, L. Schlapbach, J. All. Compd. 269 (1998) 259.

[45] G. Liang, J. Huot, S. Boily, A. V. Neste, R. Schulz, J. All. Compd. 292 (1999) 247–252.

[46] W. Oelerich, T. Klassen, R. Bormann, J. All. Compd. 315 (2001) 237–242.

[47] P. C. H. Mitchell, A. J. Ramirez-Cuesta, S. F. Parker, J. Tomkinson, D. Thompsett, The Journal of Physical Chemistry B 107 (28) (2003) 6838–6845.

[48] J. Harris, Appl. Phys. A 47 (1988) 63–71.

[49] G. Liang, J. Huot, S. Boily, R. Schulz, J. All. Compd. 305 (2000) 239–245.

[50] W. Oerlerich, T. Klassen, R. Bormann, J. All. Compd. 322 (2002) L5–L9.

[51] R. B. G. Barkhordarian, T. Klassen, Scripta Mater. 49 (2003) 213.

[52] R. B. G. Barkhordarian, T. Klassen, J. All. Compd. 364 (2004) 242.

[53] R. B. G. Barkhordarian, T. Klassen, J. Phys. Chem. B 110 (2006) 11020–11024.

[54] V. Berube, G. Radtke, M. Dresselhaus, G. Chen, Int. J. Energy Res. 31 (2007) 637–663.

[55] M. Herrich, N. Ismail, J. Lyubina, A. Handstein, A. Pratt, O. Gutfleisch, Mater. Sci. Eng. B 108 (2004) 28–32.

[56] D. Kyoi, T. Sato, E. Roennebro, N. Kitamura, A. Ueda, M. Ito, S. Katsuyama, S. Hara, D. Noréus, T. Sakai, J. All. Compd. 372 (2004) 213–217.

[57] P. Vermeulen, R. Niessen, P. Notten, Electrochem. Commun. 8 (2006) 27–32.

[58] G. Barkhordarian, T. Klassen, M. Dornheim, R. Bormann, J. Alloy. Compd.

[59] J. Zhang, T. S. Fisher, P. V. Ramachandran, J. P. Gore, I. Mudawar, Journal of Heat Transfer 127 (12) (2005) 1391–1399.

[60] T. Oi, K. Maki, Y. Sakaki, Journal of Power Sources 125 (2004) 52 – 61.

[61] H.-P. Klein, M. Groll, International Journal of Hydrogen Energy 29 (2004) 1503 – 1511.

[62] J. Thornton, Ann. Rev. Mat. Sci. 7 (1977) 239.

[63] A. Krozer, B. Kasemo, J. Vac. Sci. Technol A 5 (1987) 1003.

[64] A. N. Hashemi, J. Clark, Bull. Alloy Phase Diagrams 5 (1985) 164.

[65] K. Higuchi, H. Kajioka, K. Toiyama, H. Fujii, S. Orimo, Y. Kikuchi, J. Phys: Cond. Matter 293-295 (1999) 484–489.

[66] R. Checchetto, N. Bazzanella, A. Miotello, R. S. Brusa, A. Zecca, A. Mengucci, J. Appl. Phys 95 (4) (2004) 1989.

[67] R. Gremaud, C. P. Broedersz, D. M. Borsa, A. Borgschulte, P. Mauron, H. Schreuders, J. H. Rector, B. Dam, R. Griessen, Adv. Mater. 19 (2007) 2813–2817.

[68] J. N. Huiberts, R. Griessen, J. H. Rector, R. J. Wijngaarden, J. P. Dekker, D. G. de Groot, N. J. Koeman, Nature 380 (1996) 231–234.

[69] P. van der Sluis, M. Ouwerkerk, , P. A. Duine, Appl. Phys. Lett. 70 (25) (1997) 3356–3358.

[70] K. Yoshimura, S. Bao, Y. Yamada, M. Okada, Vacuum 80 (2006) 684–687.

[71] M. Slaman, B. Dam, M. Pasturel, D. Borsa, H. Schreuders, J. Rector, R. Griessen, Sens. Act. B 123 (2007) 538–545.

[72] M. Avrami, J. Chem. Phys. 7 (1939) 1103.

[73] M. Avrami, J. Chem. Phys. 8 (1940) 212.

[74] M. Avrami, J. Chem. Phys. 9 (1941) 177.

[75] K. Levenberg, Quart. Appl. Math. 2 (1944) 164–168.

[76] D. Marquardt, SIAM J. Appl. Math. 11 (1963) 431–441.

[77] T. Richardson, J. Slack, R. Armitage, R. Kostecki, B. Farangis, M. Rubin, Appl. Phys. Lett. 78 (2001) 3047–3049.

[78] R. Checchetto, R. Brusa, N. Bazzanella, G. Karwasz, M. Spagolla, A. Miotello, P. Mengucci, A. D. Cristoforo, Thin Solid Films 469-470 (2004) 350–355.

[79] A. Ingason, S. Olafsson, J. Alloys Comp. 404-406 (2005) 469–472.

[80] V. P. Zhdanov, A. Krozer, B. Kasemo, Phys. Rev. B 47 (17) (1993) 11044.

[81] K. Higuchi, H. Kajioka, K. Toiyama, H. Fujii, S. Orimo, Y. Kikuchi, J. Alloys Comp. 293-295 (1999) 484–489.

[82] R. Kelekar, H. Giffard, S. T. Kelly, B. M. Clemens, J. Appl. Phys. 101 (2007) 114311.

[83] A. Léon, E. Knystautas, J. Huot, R. Schulz, Thin Solid Films 496 (2006) 683–687.

[84] L. Doolittle, Nucl. Instr. and Meth. B 9 (1985) 344–351.

[85] F. Boer, R. Boom, W. Mattens, A. Miedema, A. Niessen, Cohesion in Metals-Transition Metal Alloys, North-Holland, Amsterdam, 1988.

[86] K.Yamamoto, K. Higuchi, H. Kajioka, H. Sumida, S. Orimo, H. Fujii, J. Alloys Comp. 330-332 (2002) 352–356.

[87] C. B. B. Dam, R. Gremaud, R. Griessen, Scripta Materialia 56 (2007) 853–858.

[88] A. Andreasen, M. Sorensen, R. Burkarl, B. Moller, A. Molenbroek, A. Pedersen, T. Vegge, T. Jensen, Appl Phys. A 82 (2006) 515–521.

[89] J. Huot, G. Liang, S. Boily, A. V. Neste, R. Schulz, J. Alloys Comp. 293-295 (1999) 495–500.

[90] I. Giebels, J.Isidorsson, R. Griessen, Phys. Rev. B 69 (2004) 20511.

[91] J. Isidorsonn, I. G. H. Arwin, R. Griessen, Phys. Rev. B 68 (2003) 115112.

[92] E. Davis, Philos. Mag. 22 (1970) 903.

[93] L. Grasjo, G. Hultquist, K. Tan, M. Seo, Appl. Surf. Science 89 (1995) 21–34.

[94] M. Pasturel, R. Wijngaarden, W. Lohstroh, H. Schreuders, M. Slaman, B. Dam, R. Griessen, Chem. Mater. 19 (2007) 624–633.

[95] A. Borgschulte, R. Gremaud, R. Griessen, Phys. Rev. B 78 (2008) 094106.

[96] A. Andreasen, T. Vegge, A. Pedersen, J. Phys. Chem. B 109 (2005) 3340–3344.

[97] E. Johansson, C. Chacon, C. Zlotea, Y. Andersson, B. Hjorvarsson, J. Phys. Cond. Matter 16 (2004) 7649–7662.

[98] A. Borgschulte, R. Westerwaal, J. Rector, B. Dam, R. Griessen, J. Schoenes, Phys. Rev. B 70 (2004) 155414.

[99] A. Borgschulte, R. Gremaud, S. de Man, R. Westerwaal, J. Rector, B. Dam, R. Griessen, Appl Surf. Science 253 (2006) 1417–1423.

[100] J. L. Slack, J. Locke, S. Song, J. Ona, T. Richardson, Sol. En. Mater. & Sol. Cells 90 (2006) 485–490.

[101] S. Bao, K. Tajima, Y. Yamada, M. Okada, K. Yoshimura, Sol. En. Mater. & Sol. Cells 92 (2008) 216–223.

[102] M. Slaman, B. Dam, H. Schreuders, R. Griessen, Int. J. Hyd Energy 33 (2008) 1084–1089.

[103] P. Notten, M. Ouwerkerk, H. van Hal, D. Beelen, W. Keur, J. Zhou, H.Feil, J. Power Sources 129 (2004) 45–54.

[104] P. Notten, M. Ouwerkerk, H. van Hal, D. Beelen, W. Keur, J. Zhou, H.Feil, J. All. Comp. 417 (2006) 280–291.

[105] M. S. Conradi, M. P. Mendenhall, T. M. Ivancic, E. A. Carl, C. D. Browning, P. Notten, W. Kalisvaart, P. C. Magusin, R. B. Jr., S.-J. Hwang, N. L. Adolphi, J. All. Comp. 446-447 (2007) 499 – 503.

[106] M. V. Setten, S. Er, G. Brocks, R. A. de Groot, G. A. de Wijs, arXiv:0804.0376.

[107] D. Borsa, A. Baldi, M. Pasturel, H. Schreuders, B. Dam, R. Griessen, P. Vermeulen, P. Notten, , Appl. Phys. Lett. 88 (241910).

[108] A. Baldi, D. M. Borsa, H. Schreuders, J. H. Rector, T. Atmakidis, M. Bakker, H. A. Zondag, W. G. J. van Helden, B. Dam, R. Griessen, , Int J. Hyd. energy 33 (12) (2008) 3188–3192.

[109] T. Massalski, P. Okamoto, L. Kacprzak, Binary Alloy Phase Diagrams, American Society for Metals, Metals Park OH, 1990.

[110] D. M. Borsa, R. Gremaud, A. Baldi, H. Schreuders, J. H. Rector, B. Kooi, P. Vermeulen, P. H. L. Notten, B. Dam, R. Griessen, , Phys. Rev. B 75 (2007) 205408.

[111] L. Vegard, Z. Phys. 5 (1921) 17–26.

[112] P. Vermeulen, H. J. Wondergem, P. C. J. Graat, D. M. Borsa, H. Schreuders, B. Dam, R. Griessen, P. H. L. Notten, , J. Mater. Chem. 18 (31) (2008) 3680–3687.

[113] E. Ma, , Progr. Mat. Science 50 (2005) 413–509.

[114] R. Gremaud, A. Baldi, M. Gonzalez-Silveira, B. Dam, R. Griessen, , Phys. Rev. B 77 (2008) 144204.

[115] B. R. Pauw, W. P. Kalisvaart, S. X. Tao, M. T. M. Koper, A. P. J. Jansen, P. H. L. Notten, , Acta Mater. 56 (13) (2008) 2948–2954.

[116] A. Borgschulte, W. Lohstroh, R. Westerwaal, H. Schreuders, J. Rector, B. Dam, R. Griessen, J. All. Comp. 404-406 (2005) 699–705.

[117] R. Gremaud, M. Slaman, H. Schreuders, B. Dam, R. Griessen, App. Phys. Lett. 91 (23) (2007) 231916.

[118] D. L. Windt, , Computers in Phys. 12 (4) (1998) 360.